UNIONE EUROPEA
Fondo sociale europeo

REGIONE AUTONOMA DELLA SARDEGNA

FSE 2007-2013
POR SARDEGNA
obiettivo competitività regionale e occupazione

Università degli Studi di Cagliari

PHD DEGREE
Physics

Cycle XXX

TITLE OF THE PHD THESIS

Magnetic fields in Galaxy Cluster in the Square Kilometre Array era

Scientific Disciplinary Sector
FIS/05

PhD Student:	Francesca Loi
Coordinator of the PhD Programme:	Alessandro de Falco
Supervisor:	Nicolò D'Amico

Final exam. Academic Year 2016 – 2017
Thesis defence: February-March 2018 Session

THIS THESIS HAS BEEN DONE IN THE CONTEXT OF THE SCIENTIFIC RESEARCH ACTIVITY OF THE "OSSERVATORIO ASTRONOMICO DI CAGLIARI - ISTITUTO NAZIONALE DI ASTROFISICA"

Outline of the thesis

A new era for radio astronomy is coming. The Square Kilometre Array, with its unprecedented capabilities will revolutionize our knowledge of the Universe, opening new challenges to many fields of research: from astronomy to technology, passing by the big data problem. As astrophysicists, to be ready for this revolution, we have to understand how to manage in the best way the data that the SKA will collect.

The purpose of this work is to address what is the origin of magnetic fields in the Universe and it is mainly focussed on the characterization of magnetic fields in galaxy clusters. These are ideal systems to study the properties of large scale magnetic fields as well as the relativistic particles that populate the intracluster medium. Indeed, direct manifestations of the aforementioned non-thermal components in clusters are given by the diffuse synchrotron sources named radio haloes, relics, and mini-haloes. All of these sources present low-surface brightness that makes them very elusive for the current radio telescopes. With the high sensitivity level expected for the SKA, the number of detected diffuse synchrotron sources will grow giving us the chance to characterize intracluster magnetic fields in a bigger sample of clusters. Going to kpc scales, polarized discrete radio sources play a decisive role in determining the strength and the structure of large scale magnetic fields. The Faraday rotation of the polarization plane of these sources, caused by the passage through a magneto-ionic medium, depends on the medium itself and can be used to constrain the properties of the magnetic field responsible for the rotation. So far, this approach has been applied in a limited number of galaxy clusters but the expectations for the SKA are extremely promising.

To investigate how the study of the diffuse and discrete sources can help to shed light on cosmic magnetism, I pursued a two approaches: on one side, I conducted and analysed radio observations of galaxy clusters to infer the properties of their non-thermal component, on the other side, I realized a framework to produce the polarized sky that the SKA will detect. The combination of these two approaches let us understand what are the best strategies to constrain large scale magnetic fields and it is the starting point to get prepared for the SKA.

During this thesis we used cosmological magneto-hydro-dynamical simulations performed with the ENZO software package at the Los Alamos National Laboratories (USA) by the group of Hui Li that we gratefully acknowledge.

This thesis is composed by 5 Chapters. The first consists in a general introduction with an overview on the non-thermal phenomena. Chapter 2 is based on the published work “Observations of the galaxy cluster CIZA J2242+5301 with the Sardinia Radio Telescope” and consists in a multi-frequency study of the discrete and diffuse radio sources hosted by this galaxy cluster. In Chapter 3 we present the numerical simulations tool developed during this PhD project, showing the accuracy of the simulations with respect to data. Moreover, we show our predictions, based on these numerical simulations, of the confusion limits in I, U, and Q Stokes parameters at different beam resolutions. Chapter 4 is dedicated to the application of the Rotation Measure Synthesis technique on simulated data. These data arise from a cosmological magneto-hydro-dynamical simulation of a pair of merging galaxy clusters where we include the diffuse and discrete radio sources with the FARADAY tool. Finally, the conclusions are drawn in Chapter 5.

Throughout the thesis, if it is not differently specified, we adopt a ΛCDM cosmology with $\mathrm{H_0} = 71\,\mathrm{km \cdot s^{-1} Mpc^{-1}}$, $\Omega_\mathrm{m} = 0.27$, and $\Omega_\Lambda = 0.73$.

Contents

1

Introduction

The Universe is highly magnetized on all scales, from stars to planets, from galaxies to clusters of galaxies. Even the cosmic web could host weak magnetic fields with characteristics similar to those of primordial magnetic fields. Understanding the origin and the evolution of these fields is one of the biggest open question of modern astrophysics. In this Chapter, we make a brief summary of the objects that populate the large scale structure of the Universe and we review the main properties of their associated radio emission. In addition, we discuss the theories about the origin of the non thermal component in galaxy clusters with particular attention to radio relics. We conclude the Chapter by shortly summarizing the theory of the Faraday rotation effect and the Rotation Measure Synthesis technique, a useful tool to constrain the properties of large scale magnetic fields.

1.1 The structure of the Universe: from the small to the large scale

The gravitational force dominates the structure of the Universe over a wide range of spatial scales, from planets and stars up to galaxies and clusters of galaxies. According to the standard scenario of the hierarchical formation, these structures form in the gravitational potential created by dark matter concentrations and grow through the union of small units. In what follows, we shortly discuss the main characteristics of the objects that compose the large scale structure of the Universe: the galaxies and the clusters of galaxies (see Fig. 1.1).

1.1.1 Galaxies

Galaxies contain $10^{11} \div 10^{12}$ stars and can be observed isolated or as part of small or big groups. Between the stars the space is filled by gas, dust, magnetic fields and charged particles which form the so-called interstellar medium (ISM). In particular the main components coexisting in the ISM are: clouds of molecular hydrogen (H_2 regions), clouds of neutral hydrogen (HI regions), warm plasma of ionized hydrogen (HII plasma), hot ionized plasma (coronal HII plasma), cosmic rays and dust grains (Biskamp 2003). The stars and the ISM

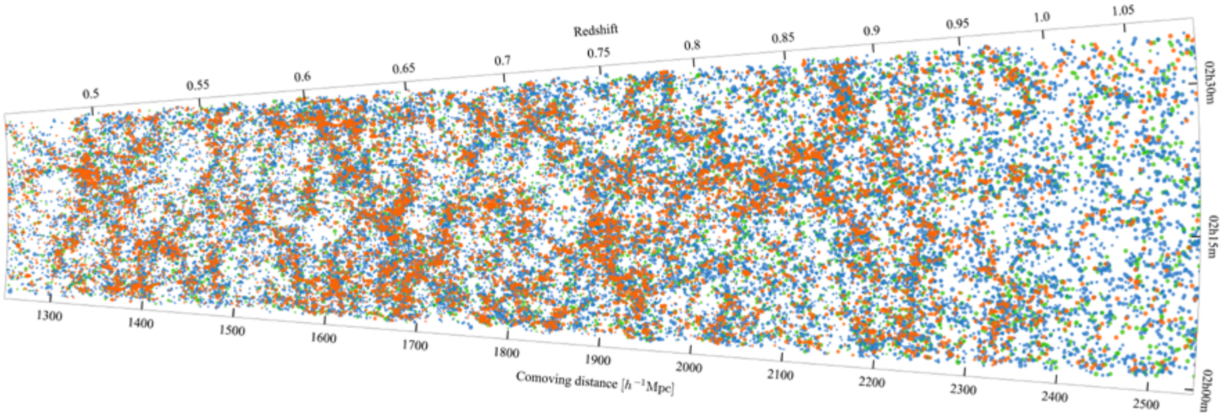

Figure 1.1 The large scale distribution of galaxies as it was between 5 and 8 billion years ago obtained from the "VIMOS Public Extragalactic Redshift Survey" (VIPERS) program (Scodeggio et al. 2016). Dots represent the observed galaxies with the colour of the dominating star population and having a size proportional to their luminosity.

emit at optical and infra-red frequencies revealing different morphologies of the hosting galaxy. Depending on the observed morphology, they are traditionally classified as spiral and elliptical galaxies in the famous “Hubble sequence”. Each class includes a more complex internal classification that takes into account other characteristics, such as the shape of the disk (e.g., arms, bars, rings, or asymmetries), the bulge-to-disk ratio, and other factors like the surface brightness, colour, and the presence of dust (Jarrett 2000). The X-ray emission in galaxies arises from different kind of objects and phenomena: stars and their environment, supernova explosion and remnants, accretion disk or jets of black holes, massive black holes in galactic nuclei or neutron stars. The analysis of the rotation curves of stars reveals the presence of an additional component in galaxies, namely the dark matter (Zwicky 1937). This is an enigmatic component of the Universe which can account for the 70% of the total mass of galaxies and it is thought to be responsible for the structure formation.

The radio continuum emission in galaxies originates from thermal and non-thermal processes. The non-thermal emission is mainly due to the synchrotron process and consists in relativistic particles with energies of $\sim$1 GeV rotating around a magnetic field of $\sim 10^{-5}$ G. The thermal emission mostly arises from the bremsstrahlung emission produced by the ionized plasma in HII regions surrounding young stars. Elliptical galaxies are generally radio quiet although about 10% of them present a strong radio counterpart, named a radio galaxy, with high values of luminosity ($\simeq 10^{41} - 10^{46}$erg s^{-1}) between $\sim$100 MHz and $\sim$10 GHz. Conversely, all spiral galaxies are radio sources mainly thanks to the star formation process that provides both the thermal component (through the ionizing uv flux from the young massive stars) and the non-thermal synchrotron emission through the supernovae remnants. A typical star forming galaxy has radio luminosities of the order of 10^{37}erg s^{-1}. In addition to the radio continuum, spectral line emission at radio wavelengths may be present in galaxies like e.g. the 21-cm line originated by the neutral hydrogen or the maser emission from molecules in the interstellar medium or the CO emission associated to molecular clouds..

1.1.1.1 Morphology of radio galaxies

Radio galaxies can assume a large variety of shapes and sizes, from the most compact (few pc) to the most complex structure covering hundreds of kpc. Traditionally, they are classified as “Faranoff-Riley” (FR) type I and type II depending on the ratio R_{FR} between the separation of the highest surface brightness on opposite sides and the total extent of the radio source. Extended radio galaxies with $\mathrm{R}_{\mathrm{FR}} < 0.5$ are classified as FRI while those having $\mathrm{R}_{\mathrm{FR}} > 0.5$ are FRII radio galaxies. Examples of FRI and FRII sources are shown in the two panels on the left of Fig. 1.2. In the first, a bright core with two opposite jets with decreasing brightness from the centre to the outer edges indicates a FRI source; in the second, a bright core and two opposite lobes hosting hotspots define a FRII source, where jets are hardly detectable. It was noticed that when applying this classification, the majority of FRIs have luminosities $\mathrm{L}_{147\,GHz} \lesssim 2 \times 10^{25}\mathrm{h}_{100}^{-2}\mathrm{W} \cdot \mathrm{Hz}^{-1} \cdot \mathrm{sr}^{-1}$ while FRII sources present higher luminosities. Many radio galaxies present a distorted morphology due to the interaction of the radio plasma with the surrounding medium. Indeed, these objects are typically found in dense environment such as the intracluster medium (ICM) of galaxy clusters. Galaxies move across the ICM at typical velocities of 1000 km/s thus the ram pressure exerted by the ICM may cause a distortion of the radio galaxy morphology due to the bending of the jets. We refer to these sources as tailed radio galaxy and in particular two types have been identified: narrow-angle tail (NAT) galaxies, where the jets of a FRI have been evidently bent (in some cases the jets point in the same direction and the source is called head-tail (HT)) and wide-angle tail (WAT) galaxies, that represent an intermediate case between FRI and FRII because of the presence of both

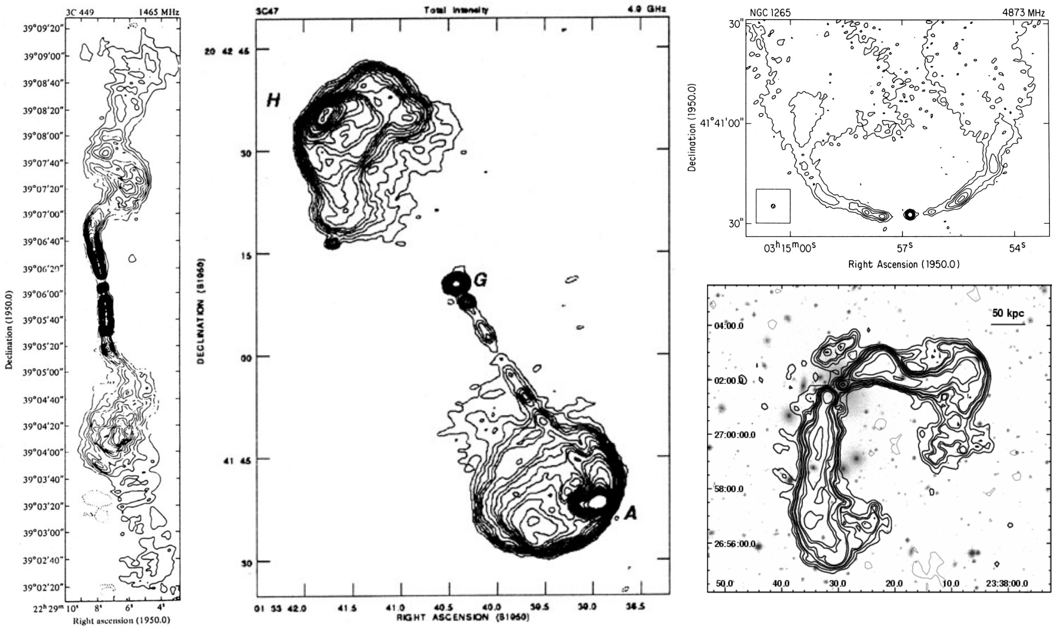

Figure 1.2 *From left to right:* VLA 1465 MHz contours of the FRI galaxy 3C 449 with angular resolution $4.8'' \times 3.4''$ (Perley et al. 1979), VLA 4.9 GHz contours of the FRII quasar 3C 47 Bridle et al. (1994) with $1.45'' \times 1.13''$ resolution, VLA 4873 MHz radio contours (top) of the NAT radio galaxy NGC 1265 where the beam is shown in the bottom right corner (O’Dea & Owen 1986) and GMRT 235 MHz radio contours (bottom) of the WAT radio galaxy 3C 465 with $17.1'' \times 11.4''$ resolution, overlaid on the POSS−2 optical image (Giacintucci et al. 2007).

jets and hotspots and appear less bent than NAT galaxies with a typical "V" shape of the tails. The prototype of NAT and WAT sources are NGC 1265 and 3C 465 respectively, and they are shown in the right panels of Fig. 1.2.
There are also other radio galaxies which cannot be included in the previous classification as their morphology is too complex and irregular or because they are compact sources.

1.1.1.2 Radio luminosity functions

Radio luminosity functions are important tools to characterize the different populations of radio sources. Indeed, the determination of the luminosity functions is necessary to constrain source physics, cosmological evolution, clustering and to evaluate the background contamination of radio observations (i.e. the confusion) (Condon 1996).
Traditionally, two classes of sources are considered: the starburst and the star forming galaxy on one side, and the FRI, FRII and all the source whose radio emission is triggered by active galactic nuclei (AGN) activity, on the other.

Following Condon (1989), we define the comoving space density of sources $\rho(\mathrm{L})\mathrm{dL}$ in Mpc^{-3} as the number of sources in a given volume with luminosities L to L+dL. The radio luminosity function (RLF) of the local Universe, i.e. the source density per unit of $\log_{\mathrm{m}}(\mathrm{L})$ where $\mathrm{m} = \mathrm{dex}(0.4) = 1$ magnitude[1] is the logarithmic interval usually chosen, is $\rho_{\mathrm{m}}(\mathrm{L})$[2]:

$$\rho_m(L) = \ln(m) L \rho(L) \tag{1.1}$$

As we can see, the RLF is in $\mathrm{mag}^{-1}\mathrm{Mpc}^{-3}$. In order to obtain an estimate of ρ_{m} in the local Universe we need radio flux densities or uniform upper limits for an optically complete sample of nearby galaxies with known redshifts z. An example of local RLFs is given in Fig. 1.3 (Mauch & Sadler 2007). Here, two populations are considered: the star-forming galaxies and the galaxies whose radio emission is triggered by an AGN. The first class presents a stable and higher density of sources at low luminosities that decays rapidly from $10^{22}\,\mathrm{W}\cdot\mathrm{Hz}^{-1}$ to higher luminosities. The AGN class has in contrast a flatter behaviour from low to high luminosities with a steepening from $10^{24}\,\mathrm{W}\cdot\mathrm{Hz}^{-1}$.

The contribution of the N radio-detected galaxies (if randomly distributed in space) in the luminosity bin of width m and centred on L is given by:

$$\rho_m(L) = \sum_{i=1}^{N} \left(\frac{1}{V_{max}}\right)_i , \tag{1.2}$$

---

[1] At visible wavelengths is common to measure the brightness of an object in magnitudes. In particular two objects, one of which is used as a reference or baseline, whose intensities (brightnesses) measured from Earth in units of power per unit area ($\mathrm{W}\cdot\mathrm{m}^{-2}$) are I_1 and $\mathrm{I}_{\mathrm{ref}}$, will have magnitudes m_1 and $\mathrm{m}_{\mathrm{ref}}$ related by:

$$m_1 - m_{ref} = -2.5 \cdot \log I_1 / I_{ref}$$

If $\mathrm{m}_1 - \mathrm{m}_{\mathrm{ref}} = 1$ then $\mathrm{I}_1 = 10^{-0.4} \cdot \mathrm{I}_{\mathrm{ref}}$.

[2] In order to derive Eq. 1.1 we can write the source density with luminosities L between L_1 and L_2 in terms of $\rho(\mathrm{L})$ and $\rho_{\mathrm{m}}(\mathrm{L})$:

$$n = \int_{L_1}^{L_2} \rho(L) dL = \int_{L_1}^{L_2} \rho_m(L) d(\log_m(L))$$

By using the logarithmic properties we know that $\log_{\mathrm{m}}(\mathrm{L}) = \ln(\mathrm{L})/\ln(\mathrm{m})$. Since $\mathrm{d}(\log_{\mathrm{m}}(\mathrm{L})) = \mathrm{d}(\ln(\mathrm{L}))/\ln(\mathrm{m})$ and $\mathrm{d}(\ln(\mathrm{L})) = \mathrm{dL}/\mathrm{L}$, we find:

$$n = \int_{L_1}^{L_2} \rho(L) dL = \int_{L_1}^{L_2} \frac{\rho_m(L) \cdot dL}{\ln(m) \cdot L} \Rightarrow \rho(L) = \frac{\rho_m(L)}{L \ln(m)}$$

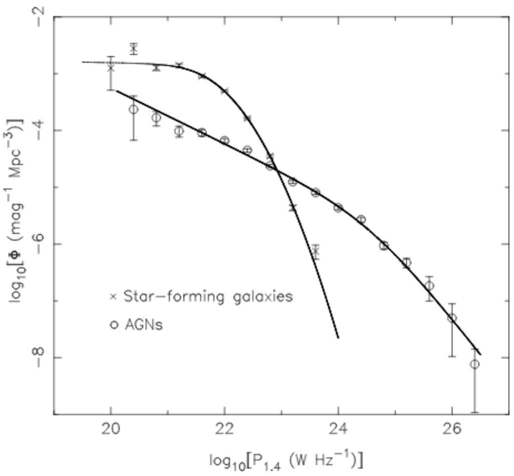

Figure 1.3 The local luminosity function at 1.4 GHz derived separately for the radio-loud AGNs (circles) and star forming galaxies (crosses) in the 6dFGS−NVSS sample (Mauch & Sadler 2007).

where V$_{\rm max}$ is the maximum volume in which the galaxy could be detected in the optical and radio bands.
The density n of the sources with luminosities between L_1 and L_2 is the integral of the space density over this range of luminosity. Using the Eq. 1.1 we can obtain n in terms of the radio luminosity function:

$$n = \int_{L_1}^{L_2} \rho(L)dL = \int_{L_1}^{L_2} \rho_m(L)\frac{1}{L}\frac{1}{\ln(m)}dL = \frac{1}{0.4}\int_{u_1}^{u_2} \rho_m(10^u)du, \tag{1.3}$$

where $u = \log L$.
It is useful to introduce the *visibility function* (von Hoerner 1973):

$$\phi(L) = L^{5/2}\rho(L), \tag{1.4}$$

that can be expressed in units of Jy$^{3/2}$ like the Euclidean-normalized differential source counts $S^{5/2}n(S)$. Being in units of Jy, the visibility function do not depend on the Hubble constant value. The RLF can be expressed in terms of the visibility function:

$$\log[\rho_m(L)_{[mag^{-1}Mpc^{-3}]}] \simeq \log[\phi(L)_{[Jy^{3/2}]}] - \frac{3}{2}\log[L_{[W\,Hz^{-1}]}] + 28.43, \tag{1.5}$$

where the numerical constant is an adjusting factor for the adopted units.

To generalize these definitions to the study of non-local sources, we need to include the cosmological evolution that can characterize these functions. For simplicity, we can consider two different evolutionary scenarios. The first is a pure luminosity evolution (PLE), described as:

$$\rho_m(L,z) = \rho_m(L/f(z),0) \quad ; \quad \phi(L,z) = \frac{1}{\ln(m)}L^{3/2}\rho_m(L/f(z),0)f(z)^{-3/2}, \tag{1.6}$$

where f(z) reproduce the evolution with respect to the redshift. The second is a pure density evolution (PDE):

$$\rho_m(L,z) = g(z)\cdot\rho_m(L,0) \quad ; \quad \phi(L,z) = \frac{1}{\ln(m)}L^{3/2}\rho_m(L,0)g(z) = g(z)\phi(L,0), \tag{1.7}$$

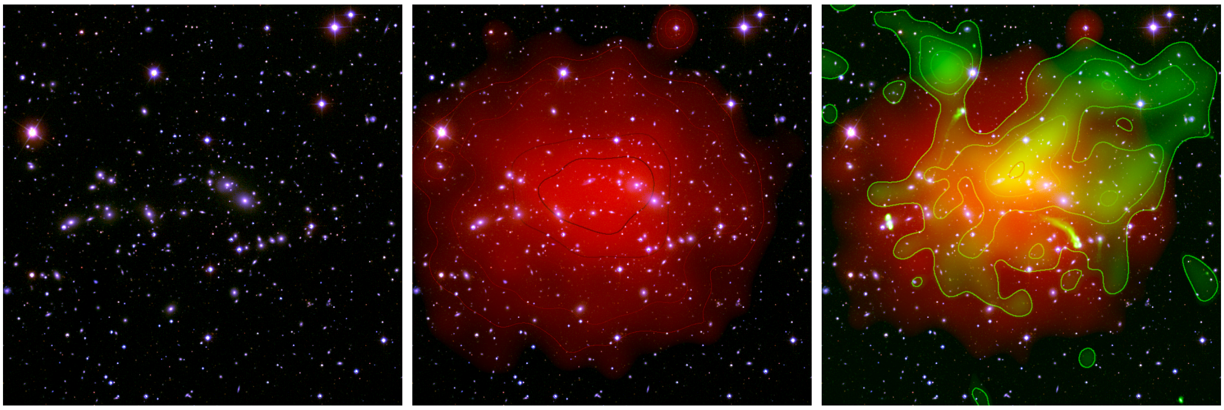

Figure 1.4 *From left to right:* optical, X-ray (red colour and black contours) and radio emission (green colour and contours) of the galaxy cluster A2255, adapted from Govoni et al. (2005, 2006).

where g(z) reproduce the evolution with respect to the redshift. Given the local RLF and assuming an evolutionary model, the comparison between the observed Euclidean-normalized source counts and the visibility function $\phi(\mathrm{L, z})$ can be used to constrain the cosmological evolutionary functions f(z) and g(z) (Condon 1984).

1.1.2 Clusters of galaxies

Galaxy clusters are the largest virialized systems of the Universe. They contain a reservoir of thermal plasma that surrounds thousands galaxies over typical volumes of few Mpc^3. Clusters have masses of the order of 10^{15} solar masses, whose only 3−5% is due to the luminous matter detectable in the visible band. 15−17% of it is constituted of thermal plasma, having temperatures of the order of $\sim 10^8$ K and densities of $\mathrm{n_e(0)} \sim 10^{-3}\,\mathrm{cm^{-3}}$ at the cluster centre. If the system is in hydro-static equilibrium (Cavaliere & Fusco-Femiano 1976), the thermal density decreases as a function of the radius r:

$$n_e(r) = n_e(0)\left(1 + \frac{r^2}{r_c^2}\right)^{-3\beta/2} \tag{1.8}$$

where $\mathrm{r_c}$ is the core radius of the cluster defined as that distance from the centre where the surface brightness has dropped to half of the central value. This component can be studied through its bremsstrahlung emission in the X-ray band. Almost 80% of the clusters mass is due to dark matter whose distribution can be constrained through gravitational lensing of background galaxies.

Galaxy clusters emit at radio frequencies because of the presence of discrete cluster radio sources but in a few cases it is possible to observe diffuse radio sources which will be discussed in the last paragraph of this Section. As an example of the multi-frequency emission of galaxy clusters, we show in Fig. 1.4, from left to right, the optical, the X-ray (red colour and black contours) and the radio emission (green colour and contours) of A2255 (Govoni et al. 2005, 2006).

1.1.2.1 Dynamical state

Clusters of galaxies form and grow due to the gravitational force that dark matter dominated clumps apply on smaller structures. The accretion can either take place as aggregation of small groups of galaxies and isolated galaxies or it can be an extremely energetic process ($\sim 10^{64}\,\mathrm{erg}\cdot\mathrm{s}^{-1}$, Sarazin 2002) as in the case of the merging of two massive clusters. In both cases, the gravitational energy that drives the formation is released in the "new" cluster causing the heating of the thermal gas through shocks, turbulent and bulk motions. The energy dissipates in times of some Gyr, and during this phase the cluster is defined as a **merging cluster**. The physics of these systems is dramatically changed by the merging phenomena as can be inferred from optical, X-ray and radio observations. In particular, shock waves provoke pressure, and temperature jumps in the ICM that can be observed as surface brightness discontinuities in the X-ray image. When one of the two clusters survives the merger we can observe cold fronts as a sharp X-ray surface brightness discontinuity while the pressure is continuous across it and the temperature and the entropy assume lower values inside the edge (Markevitch & Vikhlinin 2007).

After the system reaches a stability, where no trace of the previous merger event is detected, the cluster is defined a **relaxed cluster**. This dynamical state is characterized by the symmetry and the smoothness of the X-ray surface brightness profile that presents a central peak. As the X-ray surface brightness depends on the square of the thermal density, we expect gas cooling through the bremsstrahlung process faster in the centre than in the outer parts of the cluster. In order to preserve hydro-static equilibrium, matter should flow toward the centre. This is assumed in the cooling flow model (Fabian 1994), which predicts the so-called cooling catastrophe: matter accumulates in the centre causing a more and more rapid cooling of the gas. Temperature values as low as those predicted by the standard cooling flow model have never been observed so that other mechanisms able to prevent the cooling are under investigation. A promising explanation (see for example McNamara & Nulsen 2007) is the so-called AGN feedback which assumes that the central AGN provides the energy necessary to stop the cooling of the core.

1.1.2.2 Diffuse radio sources

Some galaxy clusters show a diffuse radio emission not associated with specific optical counterparts or discrete radio sources. The observed properties of these radio sources reveal their synchrotron nature and proof the existence of a non-thermal component in the ICM, made by relativistic particles and large scale magnetic fields. Reviews on these sources can be found in literature (see for example Feretti et al. 2012; Ferrari et al. 2008). Here, we list the major observational characteristics of these sources while the origin of the non-thermal component in clusters is discussed in Sect. 1.3.

Depending on their position and on the dynamical state of the hosting cluster, the diffuse radio sources are classified in radio relics, radio haloes and mini-haloes:

- **Radio haloes** are found at the centre of merging clusters with a size of $\sim 1\,\mathrm{Mpc}$. They are characterized by a low surface brightness ($\mathrm{S}_\nu \sim 0.1 - 1\,\mu\mathrm{Jy/arcsec}^2$ at $1.4\,\mathrm{GHz}$) and a power-law spectrum:

$$S_\nu = S_0 \left(\frac{\nu}{\nu_0}\right)^{-\alpha}, \tag{1.9}$$

  with a steep behaviour ($\alpha \gtrsim 1$). They are generally observed to be unpolarized but there are a few cases where it has been possible to detect filaments of polarized emission (up to ∼20% at 1.4 GHz), namely in the galaxy clusters A2255 (Govoni et al. 2005), MACS J0717.5+3745 (Bonafede et al. 2009) and A523 (Girardi et al. 2016).

- **Relics** are elongated arc-like sources located in the periphery of merging clusters, usually oriented perpendicularly to the merger axis but they can also assume a circular shape. As radio haloes, relics present low surface brightness, steep spectra and Mpc-sizes but differently, they exhibit high degrees of polarization ($\sim 20-30\%$ at 1.4 GHz) indicating that either the magnetic field in these sources is extremely ordered or it has been confined in a thin layer.

- **Radio mini-haloes** are typically detected at the centre of relaxed clusters or minor mergers (see Ferrari et al. 2011) around radio loud brightest cluster galaxies (BCGs). They have typical sizes of 500 kpc, and as the previous sources, low-surface brightness and steep spectrum. Some mini-haloes also present polarization levels of ∼ 10% at 1.4 GHz.

The prototypes of radio haloes and relics are hosted by the Coma cluster (Giovannini et al. 1991) while the one of mini-haloes is in the Perseus cluster (Burns et al. 1992). We show in Fig. 1.5 the Coma cluster on the left (Giovannini et al. 1993) and the Perseus cluster on the right (adapted from Sijbring 1993; Fabian et al. 2000).

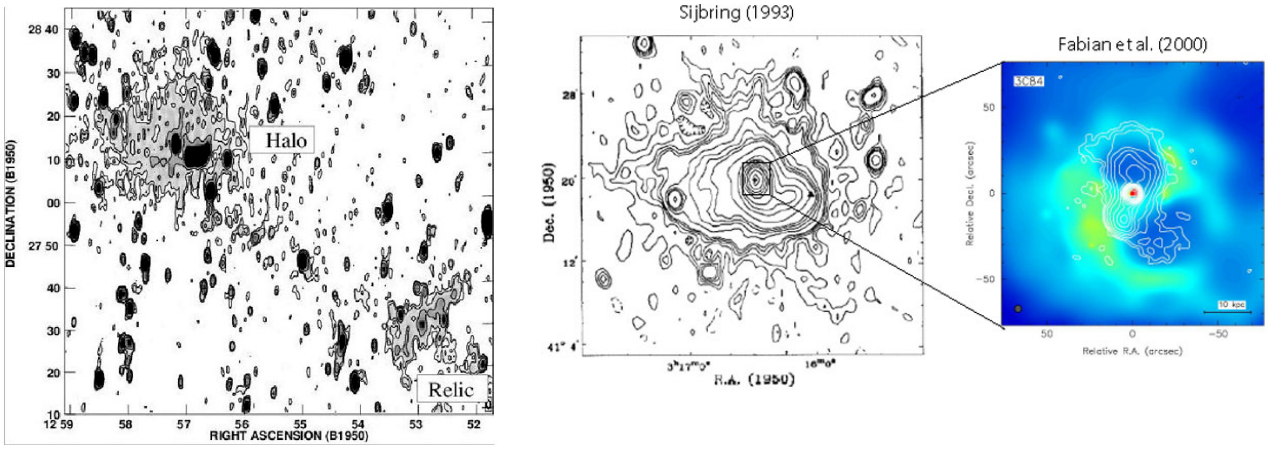

Figure 1.5 *On the left:* 327 MHz WSRT radio image of the Coma cluster with a resolution (FWHM) of $55'' \times 125''$. The radio halo is at the cluster centre, the radio relic 1253+275 is at the cluster periphery. *On the right:* 327 MHz radio image of the mini-halo in the Perseus Cluster with an inset showing radio contours overlaid on the X-ray image of the central region of Perseus.

Up to now, diffuse radio sources have been observed in 95 galaxy clusters (this number is based on the compilation of Feretti et al. (2012) and on the following detection which were not included in the review Cantwell et al. 2016; Knowles et al. 2016; Martinez Aviles et al. 2016; Shakouri et al. 2016; Kale et al. 2015; Pandey-Pommier et al. 2015; Bonafede et al. 2014a,b; Giacintucci et al. 2014; Lindner et al. 2014; van Weeren et al. 2014b,a; Giacintucci et al. 2013; Bagchi et al. 2011; Giovannini & Feretti 2000). Among them, 17 clusters show a mini-halo, 52 clusters a central radio halo, 11 of which present a radio halo and a relic and 5 a radio halo and a double relic system. There is also a case of a pair of two galaxy clusters both hosting a radio halo. Finally, 26 clusters show a relic, 7 of them two relics, which are usually oriented in opposite direction with respect to the cluster centre and extended perpendicular to the merger axis.

Observations of diffuse radio sources are in general performed with radio interferometers. The advantages of interferometer are their sensitivity level which can favour the detection of such low surface brightness objects on one side, and their angular resolution which is extremely precious to distinguish between the emission of diffuse and discrete sources on the other. Indeed, the majority of the diffuse sources hosted by galaxy clusters has been discovered thanks to all-sky surveys performed for example with the Very Large Array (VLA), i.e. the NRAO VLA Sky Survey (NVSS, Condon et al. 1998) at 1.4 GHz (see Giovannini et al. 1999), or with the Westerbork Synthesis Radio Telescope (WSRT), i.e. the Westerbork Northern Sky Survey (WENSS, Rengelink et al. 1997) at 327 GHz (see Kempner & Sarazin 2001; Rudnick & Lemmerman 2009).
However, at a given wavelength λ if the angular size θ of the source exceeds the angular size corresponding to the minimum baseline $\mathrm{B}_{\mathrm{min}}$ (minimum distance between the antennas) of the radio interferometer:

$$\theta \gtrsim \frac{\lambda}{B_{min}}$$

the instrument is not sensitive to the surface brightness of the diffuse source. It is common to refer to this as the *minimum baseline* problem or the *missing zero space* problem. Under this situation, the consequence is that from interferometric observations we cannot estimate the full size of the diffuse source and its flux density or, in the worst case, we cannot detect the source. An example of the missing zero space problem is the case of the Coma cluster whose radio halo is not detected by WSRT and VLA observations at 1.4 GHz.
Single-dish telescopes do not suffer from this limitation and they can actually retain structures as large as the observed field-of-view. They can play a decisive role in the study of diffuse radio sources especially when hosted by nearby galaxy clusters and observed at high frequencies (Emerson 2002). Indeed, there are many examples of single-dish telescope investigations of diffuse radio relics and haloes in the literature (Farnsworth et al. 2013; Carretti et al. 2013; Kierdorf et al. 2017; Loi et al. 2017b).
Nowadays, the two instruments, single-dishes and interferometers, are complementary for the study of diffuse sources allowing us to characterize their spectral behaviour over a wide range of frequency. However, next generation radio telescopes such as the Square Kilometre Array (SKA) will solve the missing zero space problem of radio interferometers and the low angular resolution of single-dish telescopes. Indeed, the SKA has been conceived to have a very compact array core, which will guarantee an unprecedented u-v coverage essential to probe very large angular scales. Moreover, its maximum baseline of ∼150 km (in its first phase, SKA1, Dewdney et al. 2015) will ensure a detailed mapping of the sky, giving us an angular resolution higher than those achievable by most current radio interferometers.

1.2 Theory of the radio emission in galaxies and galaxy clusters

Non-thermal processes are responsible for the radio emission of discrete radio sources and also of diffuse radio sources in galaxy clusters. The associated theory is well established and we refer to Rybicki & Lightman (1979) for a detailed treatment. In what follows, we review the main characteristics of the observed emission and we discuss the interpretation of the associated spectra.

1.2.1 Synchrotron emission

A relativistic charged particle moving in a magnetic field is forced to undergo a helical motion, a combination of a circular motion in the plane perpendicular to the magnetic field lines and a linearly uniform motion in the direction of the magnetic field, as one can infer from the equations of motion. The acceleration of such particle causes radiative losses and in the relativistic case ($\epsilon \gg \mathrm{m_0c^2}$, being ϵ the particle energy, c the light velocity and $\mathrm{m_0}$ the particle mass at rest) the radiation is beamed in a cone of half-angle $\simeq \gamma^{-1}$, where γ is the Lorentz factor, defined as $\gamma = \sqrt{1 - v^2/c^2}$, where v is the particle velocity. The radiative loss is described by the Larmor formula:

$$-\frac{d\epsilon}{dt} = \frac{2}{3} \cdot \frac{q^4}{c^7 m_0^4} \cdot \epsilon^2 \cdot (B \sin\theta)^2 \tag{1.10}$$

where q is the charge of the particle, θ is the angle between the magnetic field direction whose strength is B and the direction of the particle velocity. For an observer the radiation is a pulse and results in a continuum spectrum in the frequency domain described by:

$$P_\nu(\epsilon, \theta, B) = -\frac{d\epsilon}{dt d\nu} = C_1 \cdot B \cdot \sin\theta \cdot F(\nu/\nu_c) \tag{1.11}$$

where $\mathrm{C_1}$ is a constant and $\mathrm{F(x) = x \int_x^\infty K_{5/3}(z)\, dz}$ where $\mathrm{K_{5/3}(z)}$ is the Bessel function of order 5/3. The spectrum extends toward the critical frequency ν_c:

$$\nu_c = C_2 \cdot B \cdot \sin\theta \cdot \epsilon^2 \tag{1.12}$$

where $\mathrm{C_2}$ is a constant and as $\mathrm{C_1}$ only depends on fundamental constants of physics. The spectrum of a population of relativistic electrons moving in a magnetic field can be derived convolving Eq. 1.11 with the energy distribution of the particles. Assuming a power-law:

$$N(\epsilon, \theta) = \frac{N_0}{2} \epsilon^{-\delta} \sin\theta$$

for the energy distribution of electrons with Lorentz factors between $\gamma_\mathrm{min} \simeq 100$ and $\gamma_\mathrm{max} \simeq 10^4$, and the index δ variable in the range 2−4, we obtain the total intensity emissivity:

$$j_\nu(\theta) = C(\alpha_{inj}, \theta, \nu/\nu_{min}) \cdot N_0 \cdot B^{1+\alpha_{inj}} \cdot \nu^{-\alpha_{inj}} \tag{1.13}$$

where $\alpha_\mathrm{inj} = (\delta - 1)/2$ and:

$$C(\alpha_{inj}, \theta, \nu/\nu_{min}) = C_1 \cdot C_2^{\alpha_{inj}} \frac{(\sin\theta)^{2+\alpha_{inj}}}{4} \int_{\nu/\nu_{max}\sin\theta}^{\nu/\nu_{min}\sin\theta} \left(\frac{\nu}{\nu_{min}}\right)^{\alpha_{inj}-1} F\left(\frac{\nu}{\nu_{min}}\right) \cdot d\left(\frac{\nu}{\nu_{min}}\right).$$

In the previous equation $\nu_\mathrm{min} = \mathrm{C_2 \cdot B} \cdot \epsilon^2_\mathrm{min}$ and $\nu_\mathrm{max} = \mathrm{C_2 \cdot B} \cdot \epsilon^2_\mathrm{max}$. We stress that the synchrotron emissivity follows a power-law like behaviour with respect to frequency between ν_min and ν_max. Due to the shape of the synchrotron kernel emission, above ν_max the emission spectrum cuts-off exponentially while below ν_min assumes a power-law behaviour scaling as $\nu^{-0.3}$.

The synchrotron radiation is partially linearly polarized and the degree of polarization of a single particle is:

$$FPOL(\nu/\nu_{min}) = \frac{G(\nu/\nu_{min})}{F(\nu/\nu_{min})}, \tag{1.14}$$

where $G(x) = x \cdot K_{2/3}$ and $K_{2/3}$ is the Bessel function of order 2/3. The associated polarized emissivity of a particle distribution $N(\epsilon', \theta')$ is:

$$\Pi_\nu = \int_0^\infty \int_0^\pi C_1 \cdot B \cdot \sin\theta' \cdot G(\nu/\nu_{min}) \cdot N(\epsilon', \theta') d\epsilon' d\theta'. \tag{1.15}$$

1.2.2 Inverse Compton losses and radiative ages

The Cosmic Microwave Background radiation permeates the whole Universe. It is characterized by a continuum spectrum, having a maximum at 160.23 GHz as shown in Fig. 1.6. The

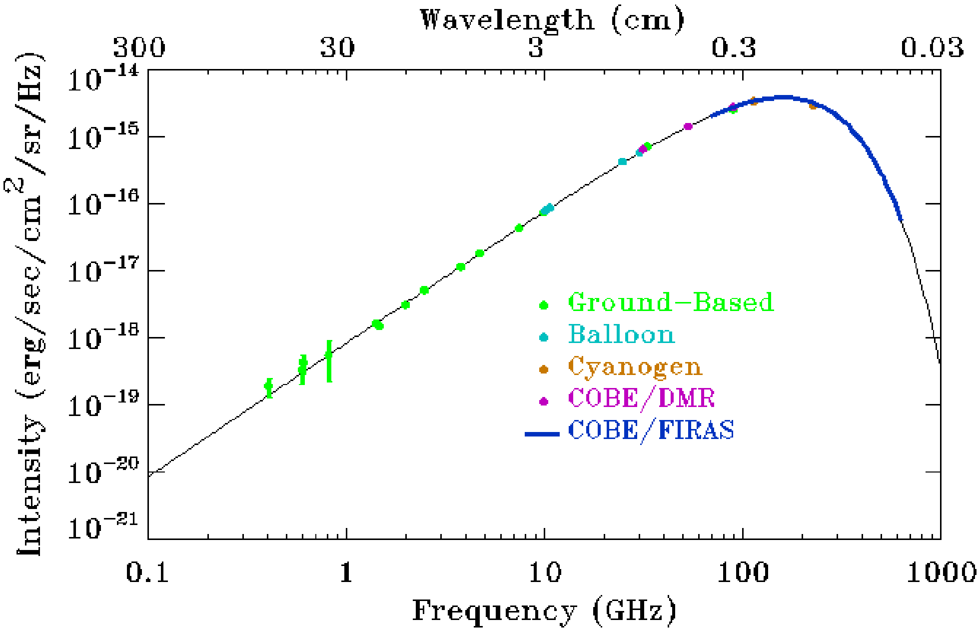

Figure 1.6 The intensity of the cosmic microwave background with respect to frequency.

CMB photon density u_γ is not constant but depends on the expansion of the Universe and on the Doppler effect:

$$u_\gamma = \frac{1}{(1+z)^4}$$

The interaction between CMB photons and relativistic electrons is an inverse Compton process, where the relativistic electron gives part of its energy to the photon. The power emitted is:

$$-\left.\frac{d\epsilon}{dt}\right|_{IC} = C_1 \cdot u_\gamma \cdot \epsilon^2 \tag{1.16}$$

which share the same energy dependence as the synchrotron losses (see Eq. 1.10). To include this kind of radiative loss in the treatment of a synchrotron source, we sum the previous equation and the Larmor formula:

$$-\left.\frac{d\epsilon}{dt}\right|_{tot} = C_1 \cdot \left(B^2 \sin\theta^2 + \frac{2}{3} B_{IC}^2\right) \cdot \epsilon^2 \tag{1.17}$$

where we expressed the CMB photon density u_γ which causes the inverse Compton in terms of an equivalent magnetic field that depends on redshift $B_{IC} = 3.25(1+z)^2\,\mu G$. Thus, the spectrum of a relativistic particle population injected at a time t is a power-law that goes to zero at a critical frequency, as described before.

It should be noted that the ratio between the synchrotron and the inverse Compton emission of a radio source is related to the magnetic field strength:

$$\frac{-\frac{d\epsilon}{dt}\Big|_{syn}}{-\frac{d\epsilon}{dt}\Big|_{IC}} = \frac{B^2\sin^2\theta}{u_\gamma^2} = \frac{L_{radio}(\nu)}{L_{X-ray}(\epsilon)}$$

Provided that we measure radio and X-ray luminosities originating from the same relativistic electrons, one can use the previous relation to estimate B.

If we assume the **continuous injection (CI)** model (Pacholczyk 1970) relativistic particles are injected at any time t and we can integrate Eq. 1.17 to find how the energy varies with time:

$$-\int_{\epsilon_0}^{\epsilon}\frac{d\epsilon}{\epsilon^2} = C_1\int_{t_0}^{t}(B^2\sin^2\theta + \frac{2}{3}B_{IC}^2)dt$$

To perform the integral over the time interval $(t - t_0)$, we can either assume that the magnetic field strength B and the angle θ to be constant with time or a constant B and θ variable over temporal scales «$(t - t_0)$ which will give us a factor of 2/3. Under the latter condition, we find:

$$\frac{1}{\epsilon} - \frac{1}{\epsilon_0} = C_1\cdot\frac{2}{3}\cdot(B^2 + B_{IC}^2)\cdot(t - t_0)$$

We can define the break energy ϵ_b as the inverse of the right part of the previous equation and write the energy $\epsilon(t)$ in the form:

$$\epsilon(t) = \frac{\epsilon_0}{1+\frac{\epsilon_0}{\epsilon_b(t)}} \quad \text{with} \quad \epsilon_b(t) = \frac{1}{C_1\cdot\frac{2}{3}\cdot(B^2 + B_{IC}^2)\cdot(t - t_0)}$$

All the relativistic electrons with injected energies ϵ_0 will lose their energy and at a fixed time t their spectrum will evidence a break in frequency at:

$$\nu_b = C_2\cdot B\sin\theta\cdot\epsilon_b^2, \tag{1.18}$$

that is moving toward lower frequencies as time evolves. Below the break frequency (where radiative losses are negligible) particles accumulate, the source luminosity grows linearly with time and the spectrum is still a power-law with index α_{inj}. Above the break frequency a steady state is reached and the high-frequency spectrum stays unchanged with a spectral index of:

$$\alpha_h = \alpha_{inj} + 0.5, \tag{1.19}$$

since radiative losses are compensated by the freshly injected particles (Kardashev 1962; Pacholczyk 1970).

By substituting the definition of ϵ_b in Eq. 1.18, we can derive the radiative age of a source, i.e. the time elapsed since the first injection (happened at $t = t_0$):

$$t_s = 1590\frac{B^{0.5}}{(B^2 + B_{IC}^2)[(1+z)\nu_b]^{0.5}}, \tag{1.20}$$

supposing that we know B here expressed in μG and ignoring adiabatic expansions. The time is in Myrs, the observed break frequency is in GHz, and we multiply it by a factor of (1+z) to consider the redshift of the emitted break frequency.

It should be noted that the break frequency of the CI model corresponds to the spectral break of the oldest electron population injected only if the particles are confined within the volume of the radio source, and the radio spectrum is extracted from a region that encloses the entire emitting region. If particles are not confined it is necessary to interpret the spectrum differently.
Let us suppose that particles escape from the emitting region, where a magnetic field feeds the synchrotron mechanism, before the radiative losses start to modify the spectrum. The result would be a power-law of the injected particles, while the aged electrons moving outside in a region with a weaker or without magnetic field cannot emit any more and thus do not contribute to the steepening of the spectrum. Alternatively, particles can escape after their aging start to influence the spectrum, causing the break at high frequencies. Incidentally, the observed spectrum is not due to all the injected particles but only to those still present in the emitting region. This means that the break do not indicate any more the age of the source but it rather refers to the confinement time.
As part of this PhD project we observed the galaxy cluster CIZA J2242+5301 (Loi et al. 2017b) with the Sardinia Radio Telescope (Bolli et al. 2015; Prandoni et al. 2017). Combining the collected data with interferometric data we determined the spectral behaviour of the northern relic of this cluster. The results are presented in Chapter 2 where a discussion similar to the previous can be found in Sect. 2.3.4.

1.3 On the origin of the large scale synchrotron emission

Several theories have been proposed to explain the origin of magnetic fields as well as the acceleration of particles up to relativistic energies in the large scale structure of the Universe. Up to now, there is not a uniquely established explanation for the non-thermal processes in galaxy clusters. In this Section we want to summarize the most reliable scenarios about the origin of magnetic fields and relativistic particles in clusters. Finally, we briefly analyse the case of radio relics to understand how observations can be used to constrain their origin.

1.3.1 Models

The models invoked to explain the intracluster magnetic field origin are numerous and still debated (Dolag et al. 2008).

Magnetic fields could have been produced at relatively low redshift, z$\sim$2$-$3, by galactic winds (Völk & Atoyan 2000) or AGN ejecta (Ensslin et al. 1997; Furlanetto & Loeb 2001) inside the proto-cluster region. This scenario is supported by the high metallicity observed in the ICM which requires an enrichment mechanism which indeed can be identified in past galactic wind and AGN ejecta. After the injection, the adiabatic compression of the proto-cluster region as well as merging phenomena such as turbulence and shock waves should amplify the magnetic field up to the observed μG-level.

Another scenario places the origin of magnetic fields in clusters at higher redshift, z$\gtrsim$4, where an early population of dwarf starburst galaxies or AGN (Kronberg et al. 1999) could have produced magnetic fields before the galaxy cluster formation. This model admits lower values of magnetic field seeds with respect to the previous one because of the larger amplification time.

Because of their presence almost everywhere in the Universe, magnetic fields could have been created in the early Universe (see the review by Grasso & Rubinstein 2001) during a phase transition, at neutrino or photon decoupling, or during the inflation. The first hypothesis is challenged by the predicted coherence length, which would be small enough to permit the dissipation of the corresponding magnetic field, while in the second case the coherence length could be large enough to guarantee a magnetic field at present time.

The Biermann battery effect (Kulsrud et al. 1997) assumes that magnetic fields of the order of 10^{-21} G are induced by thermionic electric currents that could have been generated by merger/accretion shocks. Obviously, subsequent shocks and turbulence are needed to amplify the magnetic fields to the observed μG-level.

Attempts to put constraints on primordial magnetic fields can be found in the Planck Collaboration et al. (2016), where four different imprints of a stochastic background of primordial magnetic fields on Planck data are predicted and analysed. The four methods gave consistent constraints and suggest primordial magnetic fields amplitudes at nG level. This can help to shed light on the origin of magnetic fields, while observations of galaxy clusters can give us information about magnetic field structure and strength by comparing models with data (Govoni et al. 2017; Vacca et al. 2012).

Since the direct manifestation of large scale magnetic fields is linked to the presence of relativistic particles through the synchrotron emission, it is also important to investigate the origin of such particles in the ICM. Regarding this aspect several models have been proposed that can be identified in the framework of two main scenarios (Brunetti & Jones 2014):

- *primary electron models* (Jaffe 1977; Roland 1981): relativistic electrons are injected by AGN and/or star forming activity in galaxies through supernovae explosions or galactic winds. After the ejection they start to loose energy as described in Sect. 1.2. The associated radiative lifetime is 10^{7-8}yrs which implies that these electrons can cover distances of ∼10-100 kpc. Indeed, considering that they are travelling in a magnetized plasma, the electron velocity is limited by the associated Alfvén speed $\mathrm{v_A} = \mathrm{B}/\sqrt{\mu_0 \rho}$ ∼100 km/s, where B is the magnetic field strength, μ_0 the permeability of the vacuum, and ρ the total mass density of the charged plasma particles. These models cannot explain the large sizes of radio haloes therefore a mechanism of re-acceleration *in situ* has to be included. This can be identified in the gas turbulences and shocks associated with merger events.

- *secondary electron models* (Dennison 1980; Blasi & Colafrancesco 1999; Dolag & Enßlin 2000): relativistic electron are the secondary product of hadronic collisions between relativistic protons and thermal protons of the ICM. The hadronic interactions between protons are indeed responsible for charged and neutral pion production which decay producing relativistic electrons and other particles. These models avoid the re-acceleration problem, since relativistic protons, having radiative lifetime of the order of the Hubble time, can produce relativistic electrons throughout the whole cluster volume.

From the observational point of view the two scenarios predict radio haloes with different characteristics: some are found to be in agreement with the first models and others with the second ones. First of all, assuming the first models, we should observe radio haloes only in X-ray luminous clusters, where the energy is large enough to re-accelerate particles, while according to the second ones, every cluster should host a radio halo. Primary electron models predict a complex morphology for the radio haloes and a discontinuous spectral index map, as the production and the re-acceleration of the particles is not uniform as in the case of secondary models. Indeed, in secondary models, particles are continuously and uniformly produced over the entire volume of the cluster because protons have a radiative lifetime long enough to travel throughout the cluster. In addition, primary models predict a steepening of the radio spectrum because the process is not enough efficient to compensate synchrotron and inverse Compton losses. On the other side, the hadronic interaction assumed in the secondary models predicts a large $\gamma-$ray flux from neutral pion decay and neutrino emission from the charged pion decay.

The presence of radio haloes in X-ray luminous clusters and the steepening of their spectra cannot be considered as conclusive criteria of choice between the two scenarios because the faintness of these sources limits their detection and we would need radio telescopes with a better sensitivity to investigate this point. Nevertheless, the steepening of radio spectra, when observed, cannot find an explanation in the context of secondary models. Moreover, for what concerns radio haloes, turbulence is a quite inefficient mechanism and it can be effective only during the most recent ongoing mergers leading to an irregular morphology of the radio source. It should also be noted that only upper limits on the $\gamma-$ray flux in galaxy clusters have been derived (e.g. Reimer et al. 2003; Aharonian et al. 2009a,b; Aleksić et al. 2010) and that these values are below the prediction of secondary models.

From these considerations we can conclude that the observations seems to be in better agreement with the primary electron models, although the re-acceleration mechanism is not yet clearly identified.

1.3.2 The case of radio relics

Observations of relics are consistent with the idea that they trace shock waves occurring in merger events (Röttiger et al. 1999) and in particular Enßlin et al. (1998) proposed a diffusive shock acceleration mechanism (DSA, Drury 1983) to explain the re-acceleration of relativistic particles in relics. This mechanism does not put constraints on the nature of the injected relativistic particles which is still an open question in literature. In this respect, recent observations are consistent with a scenario in which old electrons from nearby radio galaxies are re-accelerated through the DSA mechanism (e.g., Bonafede et al. 2014a; van Weeren et al. 2017). However, a single acceleration of thermal electrons by shocks or a combination of acceleration and re-acceleration have been shown to produce quite similar results in a number of specific cases (e.g., Kang & Ryu 2016). Radio observations of relics are also important to understand the evolution of large scale magnetic fields. Shock waves amplify the fields to μG-levels and align the magnetic field with the shock plane, as predicted by the aforementioned models and observed in terms of strong linearly-polarized synchrotron emission associated with relics.

1.3.2.1 Association with shocks

Shock waves are usually observed in merger events as they constitute a way for the system to dissipate the gravitational energy that drove the merger. In what follows, we consider the case of an adiabatic shock and we will assume the shocked region to be filled by a perfect gas.

The theory of the shocks can be derived from the conservation laws, i.e. matter, momentum and energy conservation. Indicating with $\mathrm{u_i}, \rho_\mathrm{i}, \mathrm{p_i}$ the velocity, the matter density and the pressure in the medium i, the conservation laws between the regions perturbed (1) and unperturbed (2) by the shock wave are:

$$\begin{cases} \rho_1 \cdot u_1 = \rho_2 \cdot u_2 \\ p_1 + \rho_1 \cdot u_1^2 = p_2 + \rho_2 \cdot u_2^2 \\ \rho_1 \cdot u_1 \left(\frac{u_1^2}{2} + \epsilon_1 + \frac{p_1}{\rho_1} \right) = \rho_2 \cdot u_2 \left(\frac{u_2^2}{2} + \epsilon_2 + \frac{p_2}{\rho_2} \right) \end{cases} \tag{1.21}$$

where ϵ is the internal energy per mass unit. From the equation of the momentum conservation, defining the density flux of matter through the discontinuity as $\mathrm{J} = \rho_1 \cdot \mathrm{u_1} = \rho_2 \cdot \mathrm{u_2}$ and the specific volumes of the upstream (perturbed) and downstream (unperturbed) regions, Υ_1 and Υ_2, as the inverse of the matter densities, we found:

$$J^2 = \frac{p_1 - p_2}{\Upsilon_2 - \Upsilon_1}.$$

which implies that the pressure and the density in the upstream region become larger than in the downstream region as a consequence of the shock passage. The last equation also holds in the opposite situation but we will see that the unperturbed medium moves toward the discontinuity with a velocity larger than the recession velocity of the perturbed medium: $\mathrm{u_2} > \mathrm{u_1}$ so that $\Upsilon_2 > \Upsilon_1$.
By combining Eqs. 1.21, we can obtain the equation of Hugoniot-Rankine:

$$\epsilon_2 - \epsilon_1 = \frac{1}{2}(p_1 + p_2) \cdot (\Upsilon_1 - \Upsilon_2). \tag{1.22}$$

that estimates the variation of the internal energy as a consequence of the shock passage. The effect of the shock wave is a non reversible process so that we will assist to an increase of the entropy in the perturbed region. From the Hugoniot-Rankine equation, it can be shown that if $\mathrm{S_1} > \mathrm{S_2}$ then $\mathrm{p_1} > \mathrm{p_2}$.
The sound speed in a given medium depends on its characteristics and in particular, for a perfect gas with adiabatic constant γ:

$$c_s^2 \equiv \left(\frac{\partial p}{\partial \rho} \right) \propto \rho^{\gamma - 1}$$

which implies a higher sound speed in the perturbed medium, $\mathrm{c_{s1}} > \frac{\Delta \mathrm{p}}{\Delta \rho} > \mathrm{c_{s2}}$. By combining the first two of Eqs. 1.21, we find that:

$$u_1^2 = \left(\frac{p_2 - p_1}{\rho_2 - \rho_1} \right) \cdot \frac{\rho_2}{\rho_1} \quad \Rightarrow \quad u_1^2 > \frac{\Delta p}{\Delta \rho} > c_{s1}$$

The shock wave moves toward the downstream medium with a velocity larger than the sound speed. This implies that the shock waves are characterized by a Mach number M defined as:

$$M \equiv \frac{u}{c_s} \tag{1.23}$$

larger than 1.

It is possible to infer the Mach number of a shock wave from X-ray observations. Indeed, these can be used to evaluate the jump in density, temperature and pressure between the upstream and downstream region. Assuming we are dealing with a perfect gas, i.e. $\epsilon = \mathrm{p}/(\rho(\gamma-1))$ and $\mathrm{M}^2 = \mathrm{u}^2\rho/(\gamma\mathrm{p})$, the jump conditions can be found from Eq. 1.22 and they are related to the Mach number by:

$$\begin{cases} \frac{\rho_1}{\rho_2} = \frac{(\gamma-1)M_1^2+2}{(\gamma+1)M_1^2} \\ \frac{T_1}{T_2} = \frac{(\gamma+1)^2 M_1^2}{[(\gamma-1)M_1^2+2][2\gamma M_1^2-(\gamma-1)]} \\ \frac{p_1}{p_2} = \frac{\gamma+1}{2\gamma M_1^2-(\gamma-1)} \end{cases} \tag{1.24}$$

1.3.2.2 The Diffusive Shock Acceleration mechanism

The DSA mechanism is a Fermi-I process based on the idea that as particles cross backwards and forwards a shock discontinuity they are accelerated. The crossing of the discontinuity can happen several times, since the medium in clusters is magnetized and it presents irregularities that diffuse the particles.

We can think of this process as a head-on collision between a particle and a more massive cloud. After the collision the particle will gain a velocity v':

$$v' = \frac{(m-M)v + 2Mu}{m+M} \approx -v + 2u$$

where M is the mass of the cloud, u its initial velocity, m is the mass of the particle and v its initial velocity. The corresponding energy gain will be:

$$\epsilon_1 = \frac{m}{2}(-v - 2|u|)^2$$

In a given interval of time many collisions can take place so that the gain of energy for the particle will vary with the time as:

$$\left\langle \frac{d\epsilon}{dt} \right\rangle_{Fermi-I} = \frac{\epsilon}{T_F}$$

where $\mathrm{T_F} = \mathrm{l}/\mathrm{u}$ being l the free mean path of the particle between two consecutive collisions. The energy of the particle at a given time can be found by integrating the previous equation:

$$\epsilon(t) = \epsilon_0 e^{t/T_F}$$

When considering a particle population, we can use the continuity equation:

$$\frac{\partial N(\epsilon,t)}{\partial t} + \frac{\partial}{\partial \epsilon}\left(\frac{d\epsilon}{dt}N(\epsilon,t)\right) + \frac{N(\epsilon,t)}{\tau_c} = Q(\epsilon,t)$$

where τ_c is the confinement time of the particles, $\mathrm{Q}(\epsilon,\mathrm{t})$ is the injection rate of particles. A stationary solution, in absence of injection ($\mathrm{Q}(\epsilon,\mathrm{t}) = 0$) is:

$$\frac{\partial N(\epsilon,t)}{\partial t} = 0$$

which implies $\mathrm{N}(\epsilon) = \mathrm{K}\cdot\epsilon^{-(1+\mathrm{T_F}/\tau_\mathrm{c})} \propto \epsilon^{-\delta}$, i.e. a power-law of the energy distribution of the particles. It should be noted that this energy distribution is necessary to obtain the synchrotron power spectrum $j_\nu \propto \nu^{-\alpha_{\rm inj}}$, with $\alpha_{\rm inj} = (\delta - 1)/2$, discussed in the previous section. Moreover, Bell (1978) showed that:

$$\delta = \frac{2u_2 + u_1}{u_1 - u_2} \tag{1.25}$$

where u_1 and u_2 are the upstream and downstream velocities. The ratio between these velocities defines the compression ratio $r = \frac{u_1}{u_2}$ so that:

$$\delta = \frac{2 + r}{r - 1} \tag{1.26}$$

Under the assumption of the previous paragraph, i.e. a perfect gas undergoing an adiabatic shock, the compression ratio r is related to the Mach number as (see Blandford & Eichler 1987):

$$r = \frac{(\gamma + 1)M^2}{(\gamma - 1)M^2 + 2} = \frac{4M^2}{M^2 + 3},$$

where in the last part we also assume that the gas is mono-atomic ($\gamma = 5/3$). By substituting the compression ratio expression in Eq. 1.26 we obtain:

$$\delta = 2 \cdot \frac{M^2 + 1}{M^2 - 1},$$

and thus, using the relation between δ and $\alpha_{\rm inj}$:

$$M^2 = \frac{2\alpha_{inj} + 3}{2\alpha_{inj} - 1}.$$

If we assume that the particles experience radiative losses inside the emitting region, we can use Eq. 1.19 to derive the relation between the Mach number and the spectral index $\alpha_{\rm h}$ at high frequency:

$$M = \sqrt{\frac{\alpha_h + 1}{\alpha_h - 1}} \tag{1.27}$$

1.4 Constraining the intracluster magnetic field

As explained in Sect. 1.2, the spectral behaviour of diffuse radio sources and their polarization properties can give us information about the characteristics of the magnetic field which gives rise to these sources. In what follows, we want to introduce the Faraday rotation effect which affects polarized signals crossing a magnetic field immersed in a thermal plasma such as the magneto-ionic plasma of a galaxy cluster. As it will be shown, from the Faraday rotation effect it is possible to constrain the intracluster magnetic field (see Carilli & Taylor 2002; Govoni & Feretti 2004, for a review on cluster magnetic fields).

1.4.1 The Faraday rotation

The Faraday effect consists in the rotation of the polarization plane of a linearly polarized signal as it crosses a magnetized plasma (see Fig. 1.7). A linearly polarized wave is a superposition of a right-hand and a left-hand circularly polarized wave. In a plasma these two components propagate with different velocity generating a phase shift which is responsible

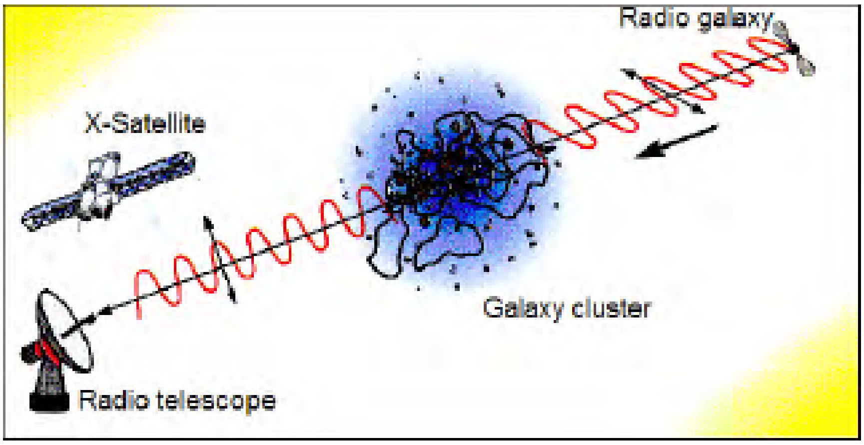

Figure 1.7 A cartoon of the Faraday rotation effect of a background radio galaxy caused by the magneto-ionic medium of a galaxy cluster.

for the rotation of the polarization plane. The rotation depends on the wavelength λ of the signal as:

$$\Psi - \Psi_0 = \lambda^2 \times RM, \tag{1.28}$$

where Ψ and Ψ_0 are the observed and the intrinsic polarization angles respectively and RM is the Rotation Measure. This quantity is linked to the line-of-sight parallel component of the magnetic field $B_{||}$ (in μG) and on the thermal plasma density n_e (in cm^{-3}) as:

$$RM = 812 \int_0^l B_{||} n_e dl. \tag{1.29}$$

The RM is in rad/m^2 and the integral is performed over the length l of the magneto-ionic plasma crossed by the signal. If we observe at different wavelengths a polarized radio galaxy located behind a galaxy cluster, we can evaluate the RM of the ICM for each line-of-sight that intercepts the radio galaxy area. An example of this procedure is shown in Fig. 1.8 for the galaxy cluster A2255 (Govoni et al. 2006). Moreover, if we have accurate X-ray observations which can give us an estimate of the thermal plasma density we can use Eq. 1.29 to infer $B_{||}$ although dedicated numerical codes are needed to extract the intracluster magnetic field properties (Enßlin & Vogt 2003; Murgia et al. 2004; Laing & Bridle 2008; Kuchar & Enßlin 2011; Bonafede et al. 2013). Indeed, only the comparison between data and mock RM images generated from the measured thermal plasma density and different simulated magnetic fields, can reveal the magnetic field characteristics. This can be done by investigating different values of the strength, the minimum and maximum scale of fluctuations in Fourier space (i.e. the power spectrum) of a magnetic field model and it needs advanced numerical approaches. Some examples of the determination of the intracluster magnetic field power spectrum from very accurate RM images can be found in literature (Vogt & Enßlin 2003; Murgia et al. 2004; Vogt & Enßlin 2005; Govoni et al. 2006; Guidetti et al. 2008; Laing et al. 2008; Guidetti et al. 2010; Bonafede et al. 2010; Vacca et al. 2012).

In the ideal case of a number of polarized background discrete radio sources such that the entire area of the cluster is covered by these galaxies we can have a complete picture of the magnetic field of the cluster and evaluate its strength and structure. Actually, from observations of individual clusters about 1-5 measurements per cluster can be made and statistical studies can only yield crude estimates of the magnetic field characteristics. Indeed, the most

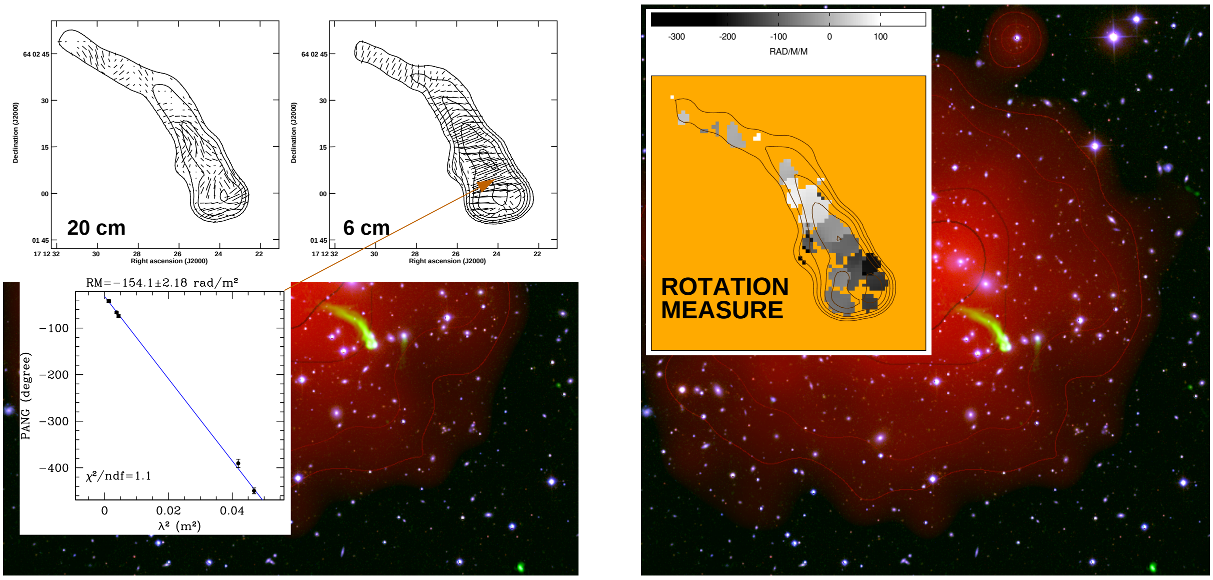

Figure 1.8 Faraday rotation measure of a cluster-embedded radio galaxy. The background image is the galaxy cluster A2255 Govoni et al. (2006) in optical (blue), X-ray (red), and radio band (green) at high resolution. *On the left*: the two top images represent the polarized signal orientation at 20 and 6 cm while the bottom panel is the fit of Eq. 1.28. *On the right*: the top panel is the RM map inferred from the fit performed for each line-of-sight.

accurate all-sky RM map available now has an average density of ∼1 RM per square degree (Taylor et al. 2009). Nevertheless, important results have been achieved both on individual clusters (Perley & Taylor 1991; Taylor & Perley 1993; Feretti et al. 1995, 1999; Taylor et al. 2001; Eilek & Owen 2002; Pratley et al. 2013) and on statistical samples (Clarke et al. 2001; Johnston-Hollitt & Ekers 2004; Govoni et al. 2010). The Square Kilometre Array will dramatically improve this situation: Johnston-Hollitt et al. (2014) predict a grid of 230−450 RM per square degree at the sensitivity of 4 μJy/beam with a resolution of $2''$. In the future, the RM grid will give us a more complete picture of large scale magnetic fields even if it is not trivial to obtain magnetic field properties from RM images.

Polarized signals undergo Faraday rotation from each magnetized plasma they cross. For instance, this means that we have to take into account the contribution of the Galaxy, which has its own magnetic field, and this can be done using an accurate map of the Galactic $\mathrm{RM}_{\mathrm{Gal}}$ (Oppermann et al. 2015). Moreover some radio sources, such as star forming galaxies, suffer from an internal rotation: the polarized signal emitted by the source rotates because of the presence of thermal plasma inside the galaxy volume. Apart from the Galactic RM, the observed rotation in this case will be the sum of two contributions: one is the internal rotation measure $\mathrm{RM}_{\mathrm{int}}$ of the radio source and one is due to the cluster $\mathrm{RM}_{\mathrm{cl}}$. Several methods have been set up to disentangle the two components based on sophisticated statistical approaches such as Bayesian inference (Vacca et al. 2016).

Radio galaxies fed by an AGN do not suffer in general from internal rotation: the jets launched by the AGN remove the surrounding plasma preventing Faraday rotation. In any case, if we observe the linearity of Eq. 1.28 between the rotation and the wavelength squared we can neglect the internal Faraday rotation and assume that the rotation is only due to the ICM.

Concerning observational limits, it is important to mention beam depolarization. Let us suppose to have a radio telescope with a beam area A and that the projection of the beam on the cluster encloses two structures of magnetic field with a different orientation and strength. We observe a background radio galaxy with a strong polarized signal in the corresponding beam area: as it crosses the cluster it will rotate differently depending on $B_{||}$ which assumes different values for the two structures. Inside the beam area the two polarized structures sum up decreasing the degree of polarization of the signal. This happens every time that the beam area is bigger than the minimum scale on which the intracluster magnetic field is homogeneous and we can use high resolution radio telescopes which have a small beam area to reduce this effect.

1.4.2 Rotation measure synthesis technique

As well as background and cluster-embedded discrete radio sources, radio haloes can be useful to constrain the characteristics of the intracluster magnetic field (Xu et al. 2012; Govoni et al. 2013). Radio haloes cover almost the whole size of the cluster and thus they could give us a complete picture of the cluster RM and therefore of the intracluster magnetic field. However, these sources, except for a few cases, are observed to be unpolarized due to internal depolarization: if we assume that along a given line-of-sight there can be different polarized structures, each one will have its own rotation measure $\phi(\mathrm{l})$ (see Eq. 1.29) which depends on the portion l of magnetized plasma crossed by each signal. It is common to refer to the $\phi(\mathrm{l})$ as the Faraday depth. When we observe the radio halo, the polarized emissions of all the structures along a line-of-sight sum up incoherently inside every single channel causing internal depolarization.

To overcome this problem we can apply the so-called RM synthesis technique (Burn 1966; Brentjens et al. 2005). The idea is to reconstruct, for each line-of-sight, the polarization as a function of the Faraday depth $\phi(\mathrm{l})$: starting from the spectra of U and Q Stokes parameters (Stokes parameters are defined in Appendix A) we assume a value for the Faraday depth and we de-rotate consequently the Stokes parameters and we compute the corresponding polarization P. We repeat the procedure by assuming different values of the Faraday depth inside a given interval and we finally obtain the variation of the polarization as a function of the Faraday depth. This approach has been applied to a simulated radio halo in a work presented by Loi et al. (2017a) and the results are shown in Fig. 1.9. The image refers to the X-ray (red), the total (green), and polarized radio emission (blue) of a simulated cluster composed by a thermal plasma and a radio halo. For a given line-of-sight the associated gas density, and intracluster magnetic field, are shown in the first two central panels as a function of the cluster length, while the bottom panel shows the polarized structure inside the halo at associated Faraday depth. The right panels report, from top to bottom, the variation of the polarized intensity (solid line) and the polarization angle (dashed) with respect to λ^2 (top), the transfer function (middle) and the recovered polarized signals along the line-of-sight (bottom). The transfer function is the response of the RM Synthesis, namely the application of the technique on a unitary polarized signal with RM=0, for each frequency channel of the bandwidth, assuming different values of Faraday depth.

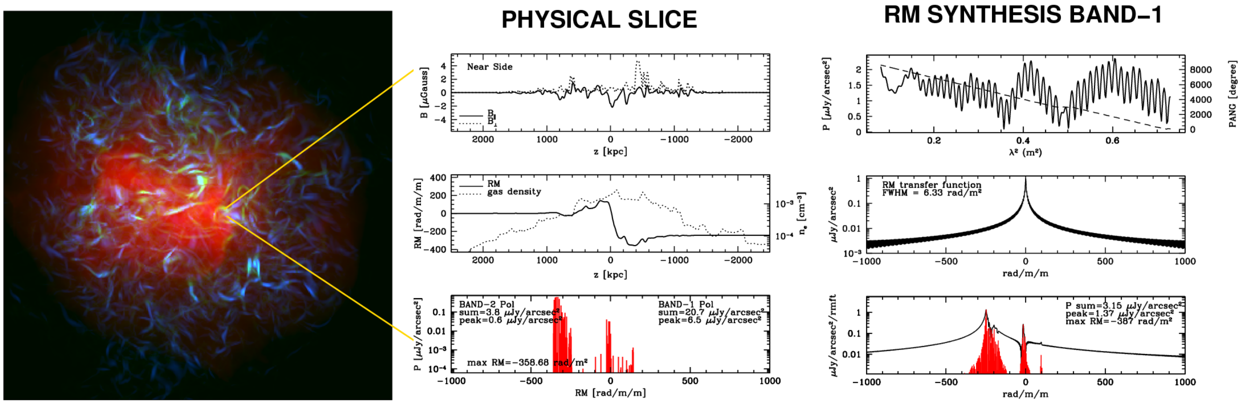

Figure 1.9 The image (left) shows the X-ray signal (red), as well as the total (green) and polarized (blue) radio emission of the simulated cluster. The central plots show the values of the parallel and perpendicular components of the magnetic field along the cluster length for a selected line of sight (top); the thermal plasma density and the RM values (middle); the polarized signal along the line-of-sight, corresponding to each RM value (bottom). The right plots show the results of the RM Synthesis technique: the variation of the polarized intensity (solid line) and of the polarization angle (dashed) with respect to λ^2 (top); the transfer function (middle) and the recovered polarized signal along the line-of-sight (bottom).

2

The large scale magnetic field of the galaxy cluster CIZA J2242+5301

Radio observations of galaxy clusters hosting diffuse radio sources give us hints on the characteristic of the non-thermal component in clusters.
In this Chapter, we present a study of the galaxy cluster CIZA J2242+5301 focuses on the determination of its spectral properties at high frequency. We conducted observations in three frequency bands centred at 1.4 GHz, 6.6 GHz and 19 GHz, with the Sardinia Radio Telescope resulting in beam resolutions of $14'$, $2.9'$ and $1'$ respectively. These single-dish data were also combined with archival Westerbork Synthesis Radio Telescope interferometric observations at 1.4 and 1.7 GHz. From the combined images, we measured a flux density of $\mathrm{S}_{1.4\mathrm{GHz}} = (158.3 \pm 9.6)$ mJy for the central radio halo and $\mathrm{S}_{1.4\mathrm{GHz}} = (126 \pm 8)$ mJy and $\mathrm{S}_{1.4\mathrm{GHz}} = (11.7 \pm 0.7)$ mJy for the northern and the southern relic respectively. After spectral modelling of the discrete sources, we measured at 6.6 GHz $\mathrm{S}_{6.6\mathrm{GHz}} = (17.1 \pm 1.2)$ mJy and $\mathrm{S}_{6.6\mathrm{GHz}} = (0.6 \pm 0.3)$ mJy for the northern and southern relic respectively. Assuming simple diffusive shock acceleration, we interpret measurements of the northern relic with a continuous injection model represented by a broken power-law. This yields an injection spectral index $\alpha_{\mathrm{inj}} = 0.7 \pm 0.1$ and a Mach number $\mathrm{M} = 3.3 \pm 0.9$, consistent with recent X-ray estimates. Unlike other studies of the same object, no significant steepening of the relic radio emission is seen in data up to 8.35 GHz. By fitting the southern relic spectrum with a simple power-law ($\mathrm{S}_\nu \propto \nu^{-\alpha}$) we obtained a spectral index $\alpha \approx 1.9$ corresponding to a Mach number ($\mathrm{M} \approx 1.8$) in agreement with X-ray estimates. Finally, we evaluated the rotation measure of the northern relic at 6.6 GHz. These results provide new insights on the magnetic structure of the relic, but further observations are needed to clarify the nature of the observed Faraday rotation.

2.1 The galaxy cluster CIZA J2242.8+5301

The galaxy cluster CIZA J2242.8+5301 was discovered from X-rays observations by Kocevski et al. (2007) during a survey aiming at finding new cluster candidates at low Galactic latitudes (l=104.19 degrees, b=−5.11 degrees). They measured its redshift (z=0.1921) and its luminosity ($L_X = 4.0 \times 10^{44}\,\mathrm{erg \cdot s^{-1}}$) in the energy band 0.1−2.4 keV. Its disturbed elongated X-ray morphology suggested that this could be an example of cluster that underwent a merger event. van Weeren et al. (2010) confirmed this scenario using observations taken with the Westerbork Synthesis Radio Telescope (WSRT), the Giant Metrewave Radio Telescope (GMRT) and the Very Large Array (VLA). In their work they presented the discovery of a faint central halo and a double relic system with a northern relic having a length of ∼2 Mpc, a width of ∼55 kpc and located 1.5 Mpc from the centre of the cluster. The radio morphology, together with the spectral index gradient of the northern relic toward the cluster centre, have been interpreted as signatures of acceleration and spectral aging of relativistic electrons due to the passage of a shock. Assuming the DSA model they found a Mach number $M \sim 4.6$ for the northern relic.

A reasonable scenario for this galaxy cluster is a collision in the plane of the sky (within 10°) between two sub-clusters with a mass ratio of 2:1 (confirmed by Okabe et al. 2015 using gravitational lensing) and an impact parameter $\lesssim$400 kpc. The core passage of the sub-clusters likely happened about 1 Gyr ago (van Weeren et al. 2011).

Association of the relics with shock fronts has been confirmed from Suzaku observations: Akamatsu & Kawahara (2013) measured a drop in temperature at the position of the northern relic, while the jump in the X-rays surface brightness was not detected, probably because of resolution limits. However, even with the highest spatial resolution X-ray data available (i.e. the Chandra data, Ogrean et al. 2014), the surface brightness discontinuity is still not detected. This aspect is very peculiar since at these high Mach numbers (M∼2-4) the discontinuity should be remarkable, as in the case of the cluster El Gordo (Botteon et al. 2016) and A665 (Dasadia et al. 2016). Projection effects can be invoked but the optical analysis by Dawson et al. (2015) points to the systems being in a nearly plane-of-the-sky merger configuration. Evidence for shock compression east of the southern relic has been observed with XMM-Newton by Ogrean et al. (2013). Recent estimates (Akamatsu et al. 2015) of temperature drops from Suzaku observations suggest a Mach number M∼2.7 and M∼1.7 for the northern and the southern relics respectively.

The tension between Mach numbers for the northern relic inferred from radio and X-ray data was the first hint for physics beyond the DSA model. As a result there were several attempts to find a consistent model for all observations of CIZA J2242.8+5301 using numerical simulations (Donnert et al. 2017). However, new measurements of the radio flux injection index resulted in a Mach number M∼2.9 (Stroe et al. 2014), in better agreement with the X-ray value inferred from the temperature jump detected by Suzaku. In recent years CIZA J2242.8+5301 has been observed over several radio frequency bands. In particular, Stroe et al. (2016) presented a study of the northern relic from 150 MHz to 30 GHz. They highlighted the steepening of the integrated spectrum beyond 2.5 GHz (from α=0.90 to α=1.77), claiming that the simple standard relic scenario could not hold for this galaxy cluster. Several models have been proposed to explain the steepening such as a time variable magnetic field in the relic area (Donnert et al. 2016), or an additional population of fossil electrons that has broken out from the shock (Kang & Ryu 2016). However, interpretations based on the currently available high frequency data (at 16 and 30 GHz) have to be taken with care because of their large uncertainties. These measurements are made from interferometric observations that could have lost a significant fraction of the total flux and can also be noticeably affected by the Sunyaev−Zel'dovich effect (see Basu et al. 2016). These aspects have been taken into account in a recent work where the relic has been studied with single-dish observations conducted with the Effelsberg telescope (Kierdorf et al. 2017). They inferred a relic spectral

L-Band

Date	Freq.$_{[\mathrm{GHz}]}$	FWHM$_{[']}$	FOV	OTF scan axis	Calibrators	TOS$_{[\mathrm{h}]}$
08 Jul 2016	1.3-1.8	14	$3^\circ \times 3^\circ$	2×RA+1×DEC	3C147	2.2
12 Jul 2016	1.3-1.8	14	$3^\circ \times 3^\circ$	1×RA+2×DEC	3C147	2.2

C-Band

Date	Freq.$_{[\mathrm{GHz}]}$	FWHM$_{[']}$	FOV	OTF scan axis	Calibrators	TOS$_{[\mathrm{h}]}$
06 Feb 2016	6.0-7.2	2.9	$1^\circ \times 1^\circ$	2×RA+2×DEC	3C286, 3C84	2.3
01 Jun 2016	6.0-7.2	2.9	$1^\circ \times 1^\circ$	2×RA+1×DEC	3C48, 3C84	2.5
24 Jun 2016	6.0-7.2	2.9	$30' \times 30'$	9×RA+9×DEC	3C138, 3C48, 3C84	4.2
26 Jun 2016	6.0-7.2	2.9	$30' \times 30'$	9×RA+9×DEC	3C138, 3C48, 3C84	5

Table 2.1 Details of the observations of the galaxy cluster CIZA J2242.8+5301 at the SRT in L and C-bands, acquired during the SMOG program. Columns report from left to right: the date, the frequency range in GHz, the beam full-width-half-maximum (FWHM), the field-of-view (FOV), the number of on-the-fly (OTF) maps carried out, the calibrators used for the data reduction, the time spent on source (TOS).

index $\alpha = (0.90 \pm 0.04)$ between 150 MHz and 8.35 GHz and suggest that models describing the origin of relics have to include effects beyond the DSA mechanism that requires $\alpha > 1$, in order to physically model the relic. Similar findings have been reported for the cluster A2256 by Trasatti et al. (2015).

From this picture, it is clear how new, accurate high frequency observations and estimates of the flux density of the northern relic are important to constrain the physical scenario of CIZA J2242.8+5301.

2.2 Observations and data reduction

We observed the galaxy cluster CIZA J2242.8+5301 at the SRT in three frequency ranges: L-band (1.3-1.8 GHz), C-band (6-7.2 GHz) and K-band (18-20 GHz). L-band and C-band observations were centred at the J2000 coordinates RA $22^h\ 42^m\ 53.0^s$ and DEC $+53^\circ\ 01'\ 05''$, while K-band observations were centred on individual galaxies of the system. The details of the observations are reported in Table 2.1 (L, C-band observations) and Table 2.2 (K-band observations).

We acquired spectral-polarimetric data in full-Stokes parameters with the SArdinia Roach2-based Digital Architecture for Radio Astronomy back-end (SARDARA, Melis et al. in prep.) for the L and C-band observations, while for the K-band observations only total intensity continuum observations were performed with the central feed. For the data reduction and the imaging we used the proprietary software package Single-dish Spectral-polarimetry Software (SCUBE, Murgia et al. 2016). In the following we describe, for each band, the observational set up and the procedure adopted for the data reduction and imaging.

L-Band

We observed an area of $3^\circ \times 3^\circ$ with the entire $1.3{-}1.8$ GHz band of the L-band receiver. We used the SARDARA back-end configuration with 1500 MHz bandwidth (the only option

K-Band					
Source	RA [$^{h\ m\ s}$]	DEC [$^{\circ\ \prime\ \prime\prime}$]	FOV	Cross Scans	Calibrators
A	22 43 38.027	+53 09 19.47	$6'$x$6'$	20	3C147
B	22 42 44.666	+53 08 04.98	$6'$x$6'$	21	3C147
C	22 43 17.995	+53 07 19.84	$6'$x$6'$	22	3C147
D	22 42 48.004	+53 05 34.99	$6'$x$6'$	23	3C147
E	22 42 53.000	+53 04 50.00	$6'$x$6'$	11	3C147
G	22 42 51.338	+53 00 35.00	$6'$x$6'$	23	3C147
H	22 42 04.820	+52 59 34.39	$6'$x$6'$	11	3C147

Table 2.2 Details of the observations of some discrete sources, in the field-of-view of the galaxy cluster CIZA J2242.8+5301, at 19 GHz with a FWHM of 1 $'$. Columns report from left to right: the source name, the source J2000 coordinates, the field-of-view (FOV) of the scans, the number of the cross scans, the calibrators used for the data reduction.

available to cover the entire 500 MHz band of the receiver) and 16384 channels of 92 kHz each. The beam FWHM is about $14'$ at a frequency of 1.55 GHz. We performed several On-The-Fly (OTF) maps in equatorial coordinates along the two orthogonal directions of RA and DEC. The telescope scanning speed was set to $6'$/s and the scans were separated by $3.5'$ to properly sample the SRT beam. We recorded the data stream by sampling at 10 spectra per second thereby producing individual samples separated by $36''$ along the scanning direction.

For our purposes, we calibrated only the total intensity. Band-pass and flux density calibration were performed by observing 3C 147 assuming the flux density scale of Perley & Butler (2013). Those frequency windows affected by persistent radio-frequency interference (RFI) were flagged by hand. We also applied an automatic flagging procedure to excise the large amount of RFI randomly spread in frequency and time. The flagged data were then used to repeat the baseline subtraction, bandpass, and flux density calibration. At these frequencies, the gain-elevation curve can be assumed to be flat and therefore we did not apply any correction.

We subtracted the baseline of the OTF maps of CIZA J2242.8+5301, scan by scan, by fitting 10% of the data at the beginning and at the end of each scan. We projected the data in a regular 3-dimensional grid with a spatial resolution of $180''$/pixel. We then applied the automatic flag procedure on the target and we repeated the baseline subtraction and the projection. In total, we discarded about 30% of the data. The total intensity image of CIZA J2242.8+5301 is obtained by stacking all the calibrated OTF maps. In the combination the individual image cubes were averaged and de-striped by mixing their stationary wavelet transform (SWT) coefficients. Coefficients on a spatial scale below 2 pixels were omitted in order to improve the signal-to-noise ratio without degrading the resolution. For further details see Murgia et al. (2016).

C-Band

We decided to make a shallow and a deep map, over a field-of-view of 1° × 1° and $30' \times 30'$, respectively. We used a 1.2 GHz bandwidth centred at 6.6 GHz. We acquired full-Stokes parameters in a bandwidth of 1500 MHz with the SARDARA back-end, with 1024 channels of 1.46 MHz each. The beam FWHM at 6.6 GHz is $2.9'$. We performed several OTF maps setting a spacing between the scans of $0.7'$ using a scan rate of $6'$/s for the shallow map and

3′/s for the deep map. We acquired 33 spectra per second, therefore, on the sky, the spatial separation between individual samples along the scanning direction was 10.9″ and 5.45″, for the shallow and the deep maps respectively.
We calibrated the band-pass and the flux density by observing 3C 286, 3C 48 or 3C 138, depending on availability for each observation, assuming the flux density scale of Perley & Butler (2013). We removed RFI observed in a cold part of the sky and we repeated the calibration and RFI-flagging procedure until all the obvious RFI was removed. Then, we applied the gain-elevation curve correction to take into account the gain variations with elevation due to the telescope structure's gravitational stress change. For the polarization we first corrected the delay between right and left polarization of the receiver by using 3C 286, 3C 138 or 3C48. Next we used 3C 84 to correct the instrumental polarization, and finally we corrected the absolute position of the polarization angle using 3C 286, 3C 138 or 3C48.
We subtracted the baseline of each scan of the OTF map of CIZA J2242.8+5301. To take into account the presence of bright sources at the edge of the images we decided to refine the baseline removal from each image cube using a mask. The mask has been obtained from the observation of CIZA J2242.8+5301 at 1.4 GHz with the NRAO VLA Sky Survey (NVSS, Condon et al. 1998): after a convolution of the map with the SRT beam we blanked all the pixels where the signal was larger than 1σ (σ=0.5 mJy/beam), in order to keep just the noise regions. We proceeded by fitting the baseline of our images with a second order polynomial, excluding the blanked regions in the mask. In this way, we could evaluate and subtract the noise more efficiently. We flagged the remaining RFI and then we repeated the baseline removal. The fraction of flagged data is $\sim$ 30%. We projected the data in a regular 3-dimensional grid with a spatial resolution of 42″/pixel. Afterwards, we stacked together all the RA-DEC scans to obtain full-Stokes I, U, and Q cubes. In the combination the individual image cubes were averaged and de-stripped by mixing their SWT coefficients. Coefficients on a spatial scale below 2 pixels were omitted to improve the signal-to-noise ratio without degrading the resolution. The polarized intensity P and the observed polarization angle Ψ were obtained from the U and Q maps by applying the relation $\mathrm{P} = \sqrt{Q^2 + U^2}$ and $\Psi = 0.5 \cdot \arctan(\mathrm{U/Q})$. The polarization maps were corrected for the positive bias introduced when combining U and Q images (see Appendix B in Killeen et al. 1986).

K-Band

At 19 GHz, the diffuse emission of CIZA J2242.8+5301 is very faint because of its steep spectrum. For instance, to detect the northern relic at 19 GHz with a S/N=3, we would need to reach a sensitivity level of σ=0.1 mJy/beam in the SRT images. Even with the SRT K-band multi-feed, this would require more than 100 hours of exposure time, too much to fit within the time allocated to the SMOG program.
Indeed, the K-band observations were aimed at characterizing the spectral behaviour of a few discrete sources embedded in the diffuse emission of the galaxy cluster CIZA J2242.8+5301. In this way we can have an accurate estimate of their flux densities at 6.6 GHz and disentangle the discrete and the diffuse emission of CIZA J2242.8+5301 (see 2.3.3).
We performed total intensity continuum observations, using a total bandwidth of 2 GHz centred on 19 GHz, at which the FWHM is $\sim 1'$. The coordinates of the cross-scans observations and other details are reported in Table 2.2.
After the baseline subtraction from each cross scan we calibrated the flux density with 3C 147 corrected for the atmosphere opacity and the gain variation with elevation. We used sky-dip

observations to infer the opacity τ. The opacity during our observations was $\tau \simeq$0.02. Finally, we projected the data in a regular 2-dimensional grid with a cell-size of 15″/pixel and we stacked all the cross scans together to improve the signal-to-noise ratio. We fitted the cross scans with a 2-dimensional Gaussian to derive the high frequency flux density.

2.3 Total intensity results

2.3.1 L-Band

Image

The results obtained from the L-band observations of CIZA J2242.8+5301 are shown in Figure 2.1 (top panel): contours start at 3σ with σ=20 mJy/beam and colours refer to the NVSS image of the cluster. The central emission belongs to the galaxy cluster CIZA J2242.8+5301. In the SRT image we note two additional features. About one degree north of CIZA J2242.8+5301 we see a diffuse arc-shaped structure which is likely due to a blending of discrete radio sources. North-east of CIZA J2242.8+5301, at ∼10 Mpc from the cluster centre, we detect an extended “L-shaped” structure which appears in the NVSS as a clustering of several point-like sources. In the bottom panel of Figure 2.1 we show a zoomed figure including this extended structure and CIZA J2242.8+5301. Colours refer to the X-ray image taken from the ROSAT All-Sky Survey (RASS, Trümper 1993) in the 0.1-2.4 keV band, corrected for the background, divided by the exposure map, and smoothed with a Gaussian of σ =90″. We overlaid the SRT contours in blue and those from NVSS in black. The SRT L-shaped structure seems to connect a few spots of X-ray emission: (1) on the west side, the closest to CIZA J2242.8+5301, hosts at its centre an NVSS source; (2) another source, which is seen at the southern tip of the extended L-shaped structure, is somewhat fainter and overlaps in projection with several NVSS sources.
We wondered if the spatial coincidence between the radio and X-ray emission may possibly indicate the presence of one or more galaxy clusters, nearby to CIZA J2242.8+5301. The association with high hardness ratios of sources in the ROSAT Bright Source Catalogue (BSC, Voges et al. 1999) and in the Faint Source Catalogue (FSC), coupled with the presence of an optical over-density or Sunyaev-Zel’dovich (SZ) signal, is a good indication of the presence of a cluster (e.g. Ebeling et al. 2002; Planck Collaboration et al. 2013). A bright source with a high hardness ratio, associated with optical over-density, is the selection criterion of the CIZA catalogue itself (Kocevski et al. 2007, and references therein). This criteria can be extended to faint sources (Ebeling et al. 2013). The source closest to CIZA J2242.8+5301 (labelled S1 in Sect. 2.3.2) is associated with the FSC source 1RXS J224504.3+532800, which has a hardness ratio of 0.93±0.09. This is also confirmed by the second RASS source catalogue (2RXS, Boller et al. 2016) and the association with the source 2RXS J224454.9+532719 having a hardness ratio of 1.0±0.1. See also Section 2.3.2.

Combination of single-dish and interferometer data

We combined our single-dish map together with interferometric maps from Stroe et al. (2013), available online[1], taken with the WSRT at 1.4 and 1.7 GHz. Data were collected in the frequency ranges between 1.303−1.460 GHz and 1.642−1.780 GHz. The beam sizes of the WSRT images are 20.95″ × 15.80″ and 15.98″ × 13.10″ at 1.4 GHz and 1.7 GHz respectively. Their

---

[1] http://vizier.cfa.harvard.edu/viz-bin/VizieR?-source=J/A+A/555/A110

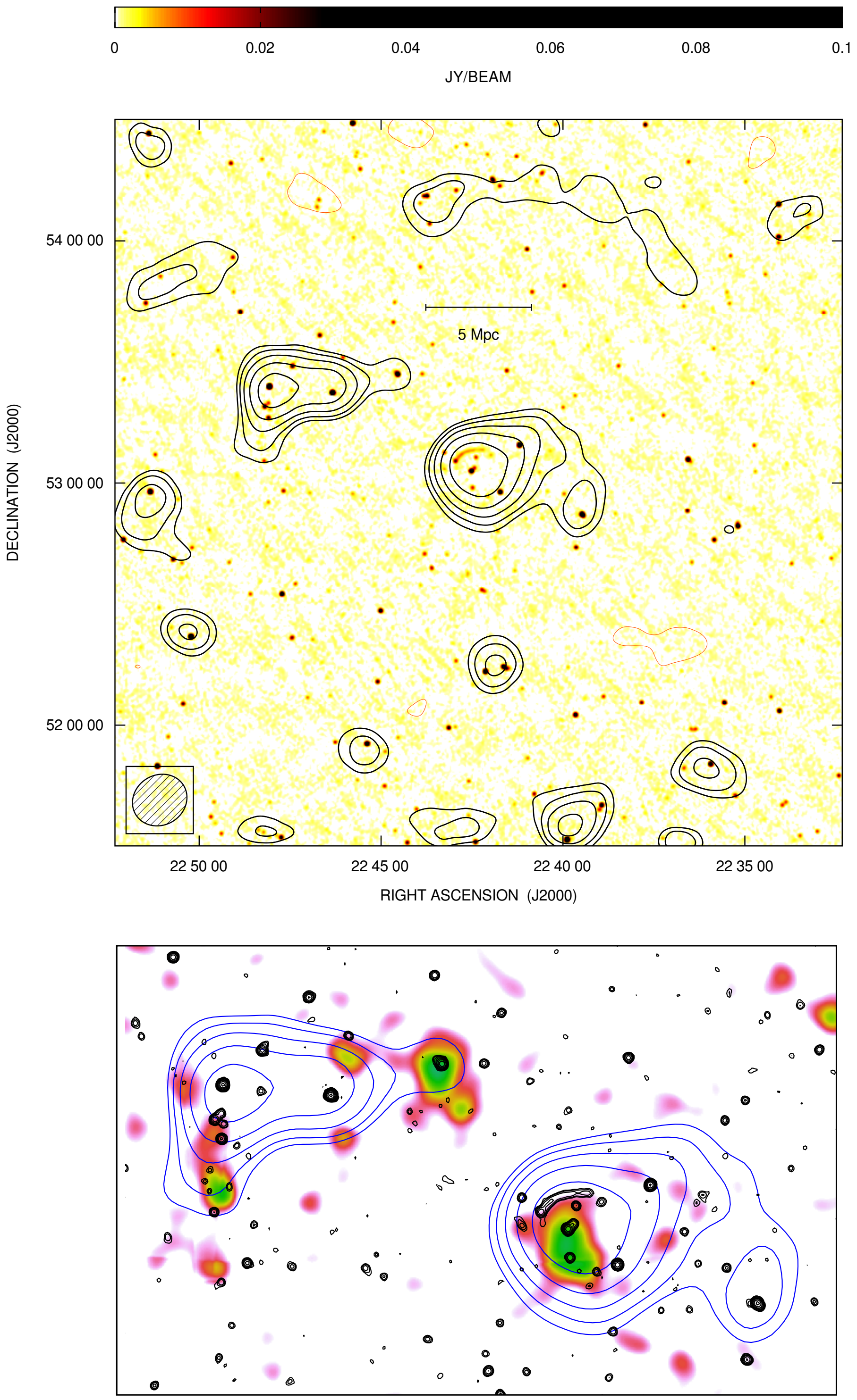

Figure 2.1 *Top:* NVSS image overlaid with the SRT total intensity contours of the galaxy cluster CIZA J2242.8+5301 obtained with the L-band receiver in the frequency range 1.3-1.8 GHz. The field-of-view of the image is 3°x3°. The FWHM beam is 14′ and is shown in bottom-left corner. The noise level is 20 mJy/beam. Contours start at 3σ-level and increase by a factor of $\sqrt{2}$ with negative contours (-3σ) drawn in orange. *Bottom:* A zoomed version including the L-shaped structure (see text) and CIZA J2242.8+5301 is shown. The SRT contours in blue and the NVSS contours in black are overlaid on the X-ray image taken from the RASS in the 0.1-2.4 keV band.

sensitivity is σ=40 μJy/beam at 1.4 GHz and σ=30 μJy/beam at 1.7 GHz.
As already mentioned in the introduction, the angular extent of the diffuse emission in CIZA J2242.8+5301 (radio halo and relics) exceeds $15'$. The maximum structure that can be recovered by the WSRT at L-band, given the minimum baseline of $\mathrm{b}_{\mathrm{min}}$=36 m between the antennas of the array, is about $16'$ for a source at the zenith. As a result, a fraction of the flux density from the radio halo and the relics could have been missed by the WSRT, due to the lack of information in the inner portion of the (u, v)-plane. The single-dish SRT L-band image does not suffer from this limitation, since structures as large as the angular scale of the SRT image are retained (3 degrees).
Therefore we combined the SRT with the WSRT images to reconstruct the correct large scale structure while preserving the angular resolution of the interferometric observations (see e.g. Stanimirovic et al. 1999).

We did this in the image plane using the SCUBE software package, in a similar way as the Astronomical Image Processing System (AIPS) task IMERG or the Miriad (Sault et al. 1995) task IMMERGE. In particular, we used the WSRT images which are already corrected for the primary beam attenuation. These images consist of a single pointing and are blanked outside a circular region of $55.3'$ and $45'$, at 1.4 and 1.7 GHz, respectively. We extracted two smaller sub-bands from the full SRT bandwidth (1.3−1.8 GHz), centred at the exact central frequencies and with the same bandwidths as the WSRT data. We cropped the two SRT images produced from these sub-bands in the same way as the WSRT images to contain the same region of the sky. After that, we transformed the single-dish and the interferometric images to combine them in Fourier space. The diameter of the SRT, 64-m, is larger than the minimum baseline of the WSRT, therefore in the Fourier plane there is a region of overlap in which both images share the same power spectral density. This annulus in the Fourier space is used to cross-check the calibration of the two images and to calculate a scaling factor that we then applied to the single-dish data. In order to account for the different resolution of the two instruments, we deconvolved the images, by dividing both of them by the Fourier transforms of the corresponding Gaussian beams, before calculating the scaling factor.
Due to the superior signal-to-noise ratio the scaling factor was calculated at 1.7 GHz. The required adjustment resulted in a scaling-up factor for the SRT image of 1.23 that we also applied to the SRT 1.4 GHz image. After this scaling the two power spectra were merged using a weighted sum of the Fourier transforms. For the single-dish observations, data weights are set to 0 for all wave-numbers larger than the outer ring of the annulus, while they are set to 1 in the inner portion of the Fourier plane. In the annulus the weights linearly vary from 0 to 1. The interferometric data are weighted in a similar way but with swapped values for the weights.
The combined Fourier spectrum was then tapered by multiplying by the transform of the interferometer beam. The combined image, obtained by the anti-transform, has the same angular resolution of the original WSRT image and includes the large scale structures detected by the SRT.

Results are shown in Figure 2.2: at left we present the WSRT maps at 1.4 GHz (top) and 1.7 GHz (bottom) and on the right we show the WSRT and SRT combined maps. Contours start at 3σ-level. Thanks to the combination we can recover the flux density associated with the diffuse sources of the galaxy cluster CIZA J2242.8+5301, revealing a greater extension of the central radio halo, especially at 1.4 GHz. At 1.7 GHz we do not see a significant enhancement of the radio halo emission. This could be consistent with the fact that typically these sources have a steep spectrum (α=1.3) such that at higher frequencies the associ-

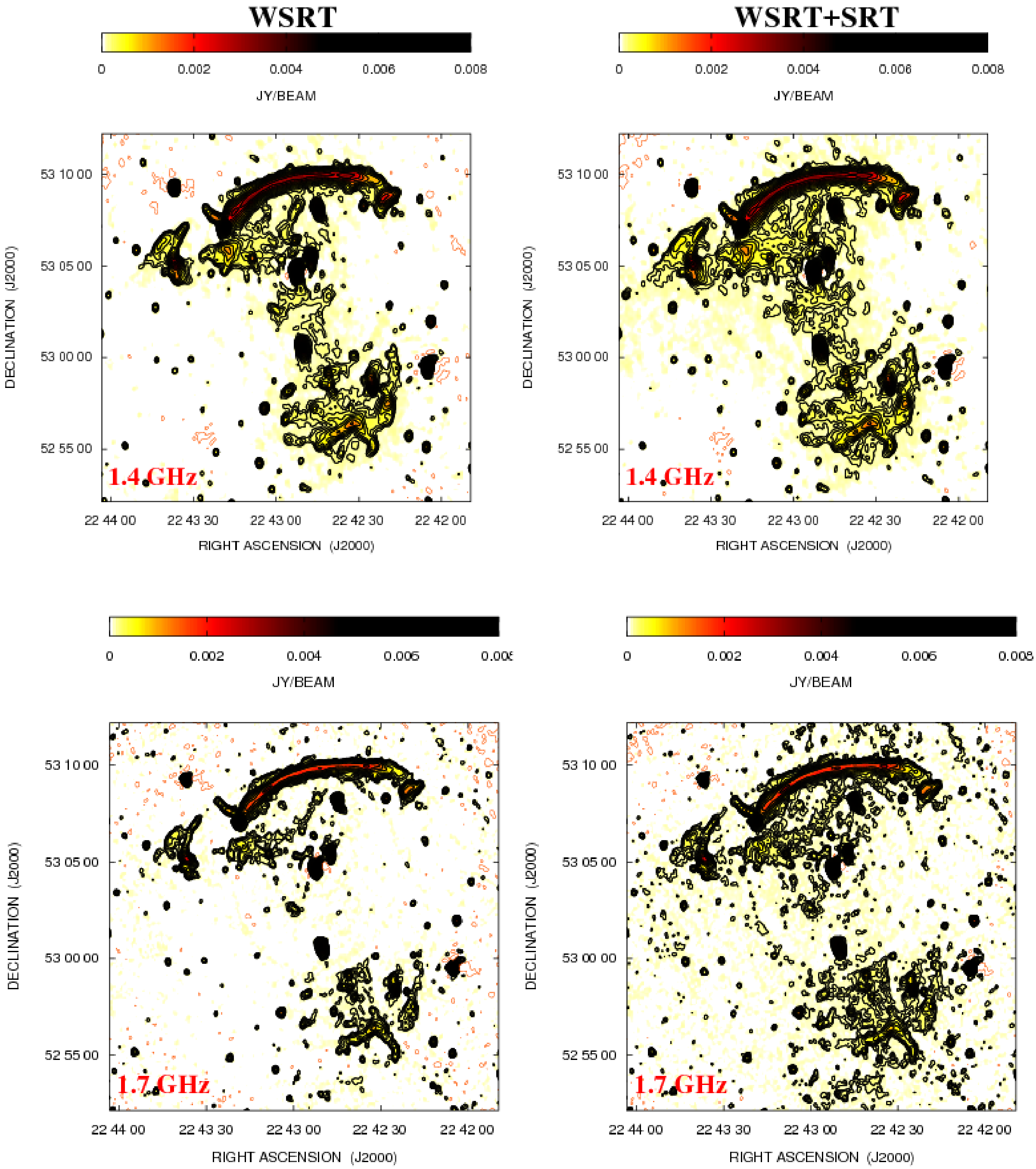

Figure 2.2 Results of the single-dish interferometer combination: on the left we show the WSRT maps at 1.4 GHz (top) and 1.7 GHz (bottom) taken from Stroe et al. (2013) and on the right the WSRT and SRT combination maps. Contours start at 3σ-level, where σ=40 μJy/beam at 1.4 GHz and σ=30 μJy/beam at 1.7 GHz, and increase by a factor of $\sqrt{2}$. Negative contours (-3σ) are drawn in orange. The beam sizes of the images are $20.95'' \times 15.80''$ at 1.4 GHz and $15.98'' \times 13.10''$ at 1.7 GHz.

ated flux could be lower than the rms of the map. Assuming the same size at the two frequencies the mean surface brightness at 1.7 GHz should be $\langle I_{1.7\mathrm{GHz}} \rangle = \langle I_{1.4\mathrm{GHz}} \rangle \times 0.485$, a factor that takes into account the different beam areas of the two instruments. At 1.4 GHz, $\langle I_{1.4\mathrm{GHz}} \rangle \sim 3.8 \times \sigma_{1.4\mathrm{GHz}}$ that implies $\langle I_{1.7\mathrm{GHz}} \rangle \sim 0.074$ mJy/beam. Thus, in order to detect the radio halo at 1.7 GHz, we would need a noise level of σ=25 μJy/beam, lower than the rms of the image.

Flux density measurements of diffuse sources

We measured the flux density of the diffuse emission of the galaxy cluster CIZA J2242.8+5301 at 1.4 GHz using the combination of SRT and WSRT data.

As we do not observe radio halo emission in the WSRT 1.7 GHz image of Figure 2.2 at the 3σ-level we used this image to blank the strong sources in the field of CIZA J2242.8+5301 from the 1.4 GHz images. We ended up with an image where the discrete sources and the relics are blanked as shown by blue contours in Figure 2.3.

In this image black represents the emission above the 3σ-level of the combined map at 1.4 GHz. We assumed that this is the extent of the radio halo and that the relics are located inside the red contours. We defined the northern relic region by taking all those pixels inside the same area considered by Stroe et al. (2016) in Figure A1 with a flux density greater than 5σ, excluding obvious discrete sources. The southern relic emission is fainter than that of the northern relic. Thus, to isolate the southern relic from the radio halo, we used a stronger limit in flux by drawing a 8σ-level contour around the relic. We used the black area outside

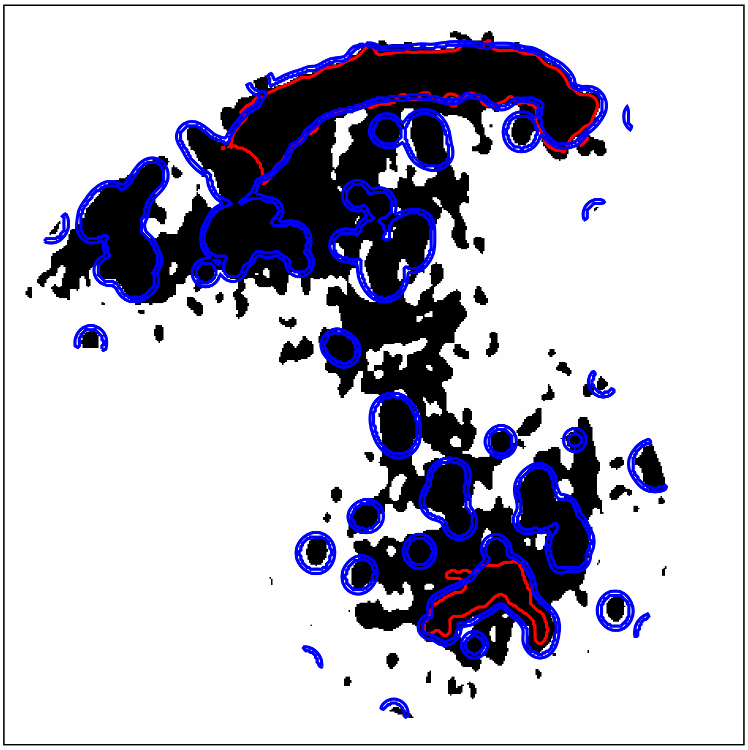

Figure 2.3 This image shows the area we considered to measure the flux of the diffuse sources hosted by CIZA J2242.8+5301: red contours are drawn around the relic areas, while black colour corresponds to the radio halo emission. Blue contour indicates strong sources that we did not consider in the estimate of the halo mean surface brightness.

the blue contours (equivalent to ∼451 times the beam area) to evaluate a mean surface brightness of the radio halo. Then, we multiplied this value by the total area (equivalent to ∼869 times the beam area), as we assume that the halo extends even in the relic regions and that of the discrete sources.
We found that the radio halo hosted by CIZA J2242.8+5301 has a total flux density of $S_{1.4GHz}^{SRT+WSRT} = (158.3 \pm 9.6)$ mJy. We noticed that if we measure with the same procedure the radio halo flux from the WSRT 1.4 GHz image we find $S_{1.4GHz}^{WSRT} = (115 \pm 7)$ mJy. In our estimates we included statistical and systematic (6% of the flux to include calibration uncertainties) errors. The northern relic has a total flux density of $S_{1.4GHz}^{WSRT} = (121 \pm 7)$ mJy and $S_{1.4GHz}^{WSRT+SRT} = (126 \pm 8)$ mJy as calculated from the interferometric and combined maps respectively. Here we have subtracted the contribution of the extended radio halo in order to take into account only the flux density of the northern relic. Finally, we found that the southern relic has a flux density $S_{1.4GHz}^{WSRT+SRT} = (11.7 \pm 0.7)$ mJy, a value consistent, within errors, with that calculated from the interferometric map, $S_{1.4GHz}^{WSRT} = (11.0 \pm 0.7)$ mJy.
For the radio halo we find an enhancement of the flux density of about $\sim 38\%$ when we combine single-dish and interferometric images, whereas for the relics we obtain no significant differences. This demonstrates how the interferometer has poor sensitivity to extended and diffuse emission while it performs better with narrow structures such as the northern relic.

The statistical properties of radio haloes in galaxy cluster are important in order to understand the nature of these sources. Thanks to our measurements, we can now compare the properties of CIZA J2242.8+5301 with other clusters that host radio haloes. In Figure 2.4, we plot the 1.4 GHz power of the radio halo versus the X-ray luminosity between 0.1−2.4 keV (top) and the 1.4 GHz power of the radio halo versus its largest linear size (bottom) measured at the same frequency. Filled dots are observed clusters taken from the literature. We added to the compilation by Feretti et al. (2012) new radio haloes in merging galaxy clusters revealed through pointed interferometric observations at ≃1.4 GHz (Govoni et al. 2012; van Weeren et al. 2012; Giovannini et al. 2013; Martinez Aviles et al. 2016; Shakouri et al. 2016; Parekh et al. 2017). A red triangle marks the cluster CIZA J2242.8+5301 whose properties have been obtained from single-dish and interferometric combined maps. The radio halo of CIZA J2242.8+5301 appears as one of the largest and one of the brightest radio haloes observed so far but this result can be significantly affected by the comparison with interferometric measurement which could have lost a significant portion of source flux density and estimated a smaller LLS. However, it should be noted that there is not a standard procedure to measure the flux density and the size of radio haloes therefore every comparison have to be taken with care.

2.3.2 Shallow C-band

Image

In Figure 2.5 (bottom) we show the resulting total intensity contour map in the frequency range between 6 and 7.2 GHz over a region of 1°x1°. We reached a noise level of σ=1 mJy/beam with a beam size of $2.9' \times 2.9'$. The radio contours at 6.6 GHz are overlaid on the same X-ray image as Figure 2.1, taken from the RASS in the 0.1-2.4 keV band. The central cluster is bright both in the X-ray and radio band and we detected the diffuse radio emission associated with CIZA J2242.8+5301.
Among the external sources, marked with a letter in the image, the most interesting is S1.

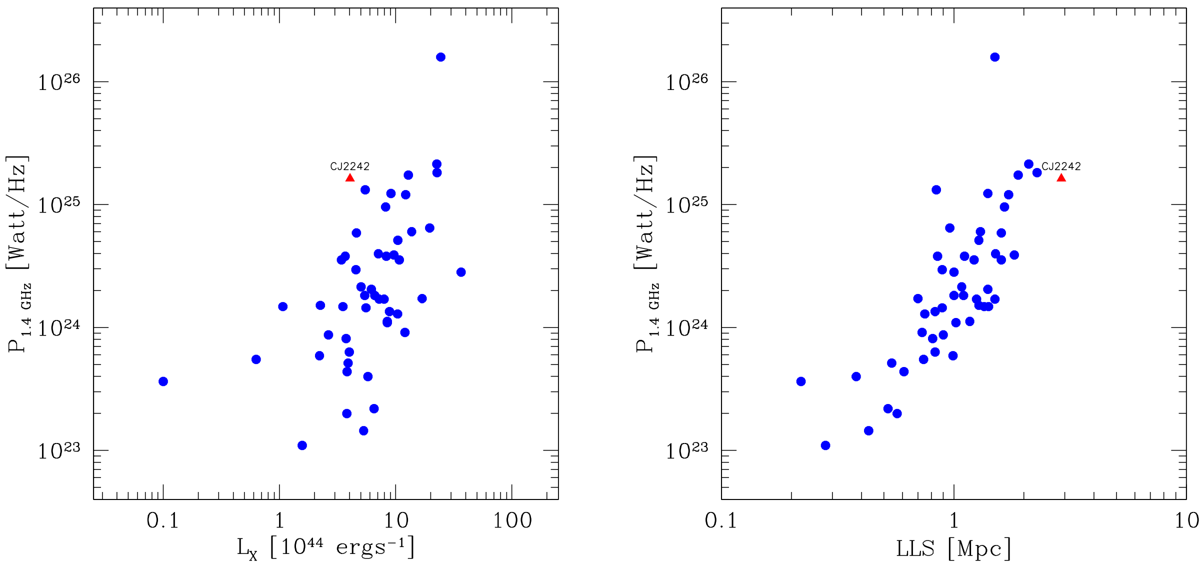

Figure 2.4 Radio halo power at 1.4 GHz versus the cluster X-ray luminosity in the 0.1-2.4 keV band (top) and versus the largest linear size of the radio halo measured at 1.4 GHz (bottom). Full dots are observed clusters taken from the literature. We added to the compilation by Feretti et al. (2012) new radio haloes in merging galaxy clusters revealed through pointed interferometric observations at ≃1.4 GHz (Govoni et al. 2012; van Weeren et al. 2012; Giovannini et al. 2013; Martinez Aviles et al. 2016; Shakouri et al. 2016; Parekh et al. 2017). A red triangle marks the cluster CIZA J2242.8+5301.

As already pointed out in Section 2.3.1, the X-ray emission has the right hardness ratio to be classified as a galaxy cluster candidate. We show in Figure 2.5 (top), contours of the 323 MHz GMRT image of Stroe et al. (2013). These contours are drawn starting from 2 mJy/beam and increase by a factor of 2. Thanks to the higher resolution of the GMRT we can appreciate the head-tail morphology of the source which is further indication of the presence of a dense external medium similar to what is typically found in galaxy clusters. The radio contours are overlaid on an optical Canada-France-Hawaii Telescope (CFHT) image[2], where two blue crosses indicate the position of two optical galaxies: 2MASX J22445464+5328318, at less than 0.2′ from S1, and 2MASX J22445565+5327578, at less than 0.7′. The galaxies have a K-band magnitude of M=(13.5±0.1) mag and M=(12.67±0.06) mag, respectively, already corrected for extinction (see Appendix in Schlafly & Finkbeiner 2011). By using the K-band magnitude-redshift relations of Inskip et al. (2002) we found that these galaxies have a redshift z∼0.1-0.2, similar to CIZA J2242.8+5301. We obtained a similar result ($z \sim 0.15 - 0.2$) when considering the K-band magnitude-redshift relation for brightest cluster galaxies (see Fig.5 in Stott et al. 2008).

Even if at the moment there are only two optical galaxies identified in the vicinity of S1, this fact, together with its X-ray properties and the fact that S1 is an head-tail radio source, corroborates the hypothesis of S1 as a cluster candidate.

---

[2] http://www.cadc-ccda.hia-iha.nrc-cnrc.gc.ca/en/search/

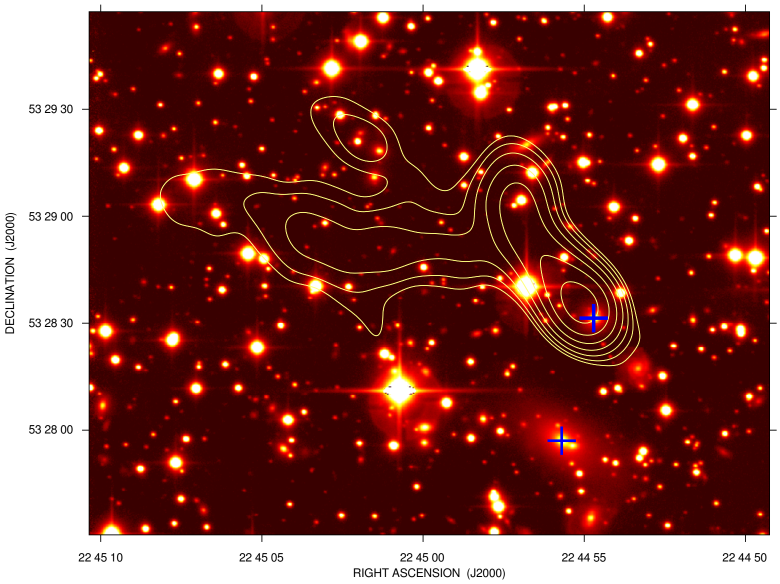

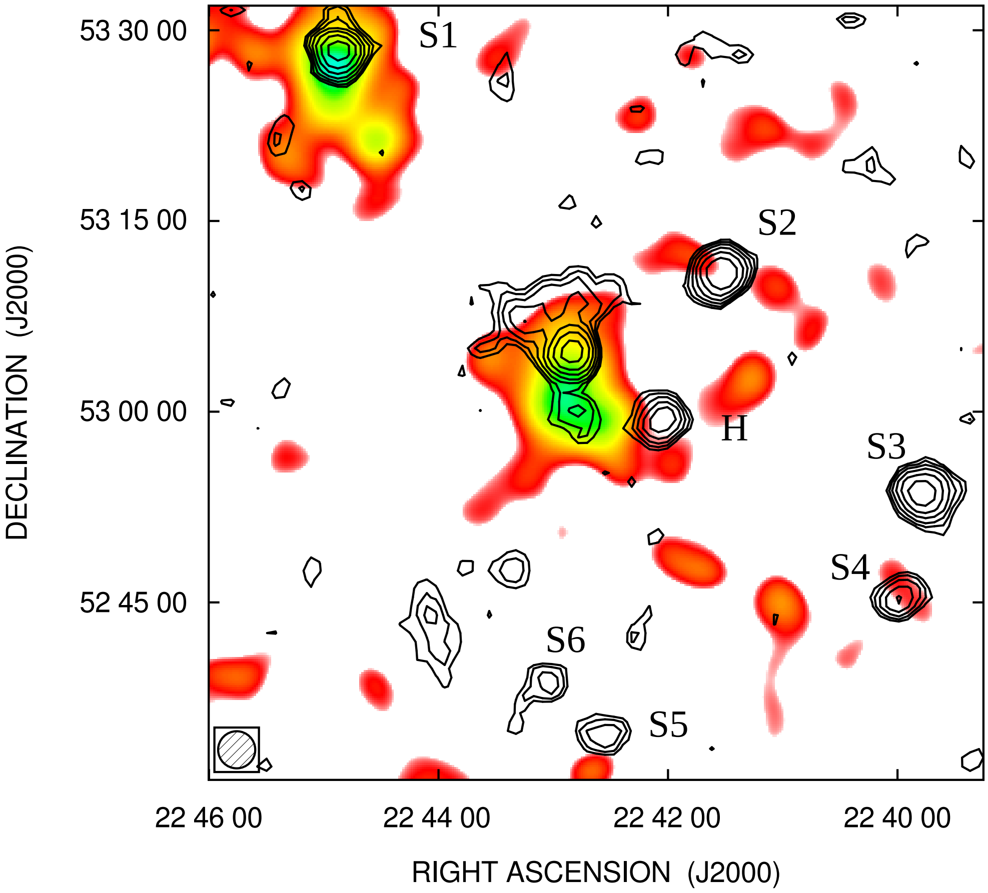

Figure 2.5 *Top:* CFHT optical image of S1 with the two optical galaxies indicated by the crosses and contours from the 323 MHz GMRT image that start at 2 mJy/beam and increase by a factor 2. *Bottom:* Shallow SRT total intensity contour image of the galaxy cluster CIZA J2242.8+5301 at 6.6 GHz overlaid on the X-ray image taken from the RASS in the 0.1-2.4 keV band. The SRT image has been obtained from the spectral average of the data in the frequency range 6−7.2 GHz. The field-of-view is 1° × 1°. The FWHM beam is 2.9′ and is shown in bottom-left corner. Contours start at 3σ-level, with σ=1 mJy/beam, and increase by a factor of $\sqrt{2}$.

Label	Name	$S^{\mathrm{mJy}}_{1.4\mathrm{GHz}}$	$S^{\mathrm{mJy}}_{6.6\mathrm{GHz}}$	α
S1	NVSS J224455+532840	133±8	28±2	1.00±0.09
S2	87GB 223927.9+525526	138±8	26±2	1.08±0.09
S3	4C +52.50	182±11	26±2	1.3±0.1
S4	NVSS J224001+524538	35±2	9±1	0.9±0.1
S5	NVSS J224234+523506	32±2	6±1	1.1±0.2
S6	NVSS J224258+523912	11±1	5±1	0.5±0.2
H	NVSS J224205+525931	99.6±0.6	14±2	1.3±0.2

Table 2.3 Flux measurements of the sources marked in Figure 2.5 obtained from the NVSS 1.4 GHz (Condon et al. 1998) and the SRT 6.6 GHz images (this work).

Flux density measurements of discrete sources

In Table 2.3 we give the flux density of the sources identified in the field and marked with a letter in Figure 2.5, measured from the NVSS 1.4 GHz and the SRT 6.6 GHz images (at their original resolution). We also calculated the spectral index α of the sources assuming for the flux density S_ν a power law behaviour with the frequency ν (see Eq. 1.9). For source S1 we found $\alpha = 1.00 \pm 0.09$ which is typical for head-tail sources as pointed out in the previous Section.

2.3.3 Deep C-Band

Image

In Figure 2.6 we show the total intensity map resulting from all the observations at 6.6 GHz in a field-of-view of $30' \times 30'$ centred on the cluster centre. In this image we reached a noise level of $\sigma = 0.5\,\mathrm{mJy/beam}$. Here the two relics are clearly detected.

Discrete sources modelling

We characterize the spectral behaviour of the discrete sources, at less than $15'$ from the cluster centre, by using the following multi-frequency high resolution images of the galaxies:

1. from the NRAO archive we retrieved observations from the program AV312 presented by van Weeren et al. (2010), which used the VLA in C configuration at 4835 MHz and 4885 MHz. We calibrated data following standard procedures using the AIPS software package;

2. we used GMRT 323 MHz, 608 MHz and WSRT 1714 MHz, 2272 MHz images from Stroe et al. (2013) available online[3];

3. we included in our sample the Westerbork Northern Sky Survey (WENSS) at 325 MHz (Rengelink et al. 1997) and the NVSS at 1400 MHz (Condon et al. 1998) maps;

4. we also added the SRT 19 GHz observations reported in Table 2.2.

We considered the nine sources marked in Figure 2.7 whose flux is mixed with the diffuse sources at the SRT resolution. In this image colours represent the SRT total intensity image

---

[3] http://vizier.cfa.harvard.edu/viz-bin/VizieR?-source=J/A+A/555/A110

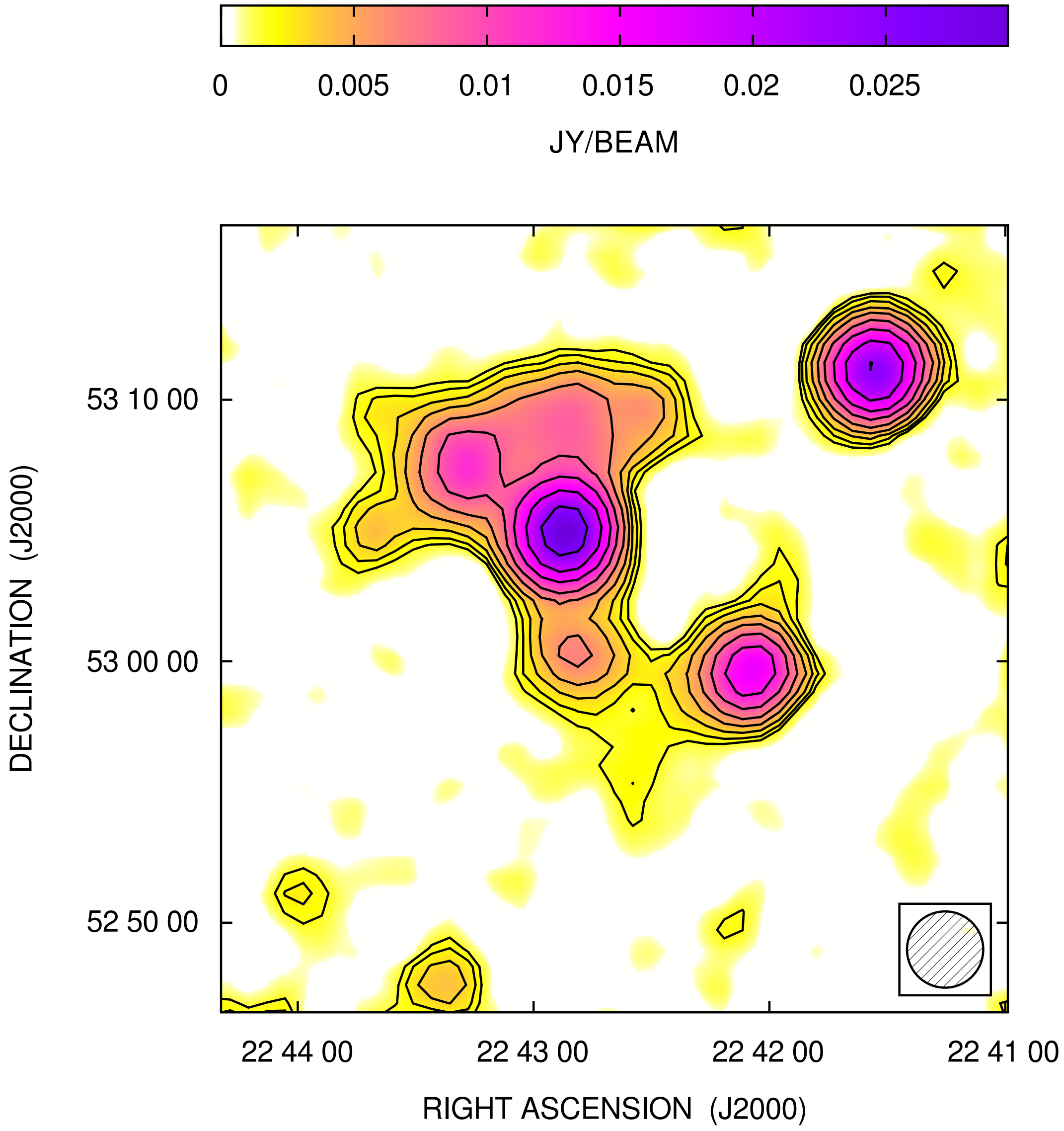

Figure 2.6 Deep SRT total intensity image of the galaxy cluster CIZA J2242.8+5301 obtained from the spectral average over the frequency range 6−7.2 GHz. The field-of-view of the image is $30' \times 30'$. The FWHM beam is $2.9'$ and is shown in bottom-right corner. The noise level is 0.5 mJy/beam. Contours start at 3σ-level and increase by a factor of $\sqrt{2}$.

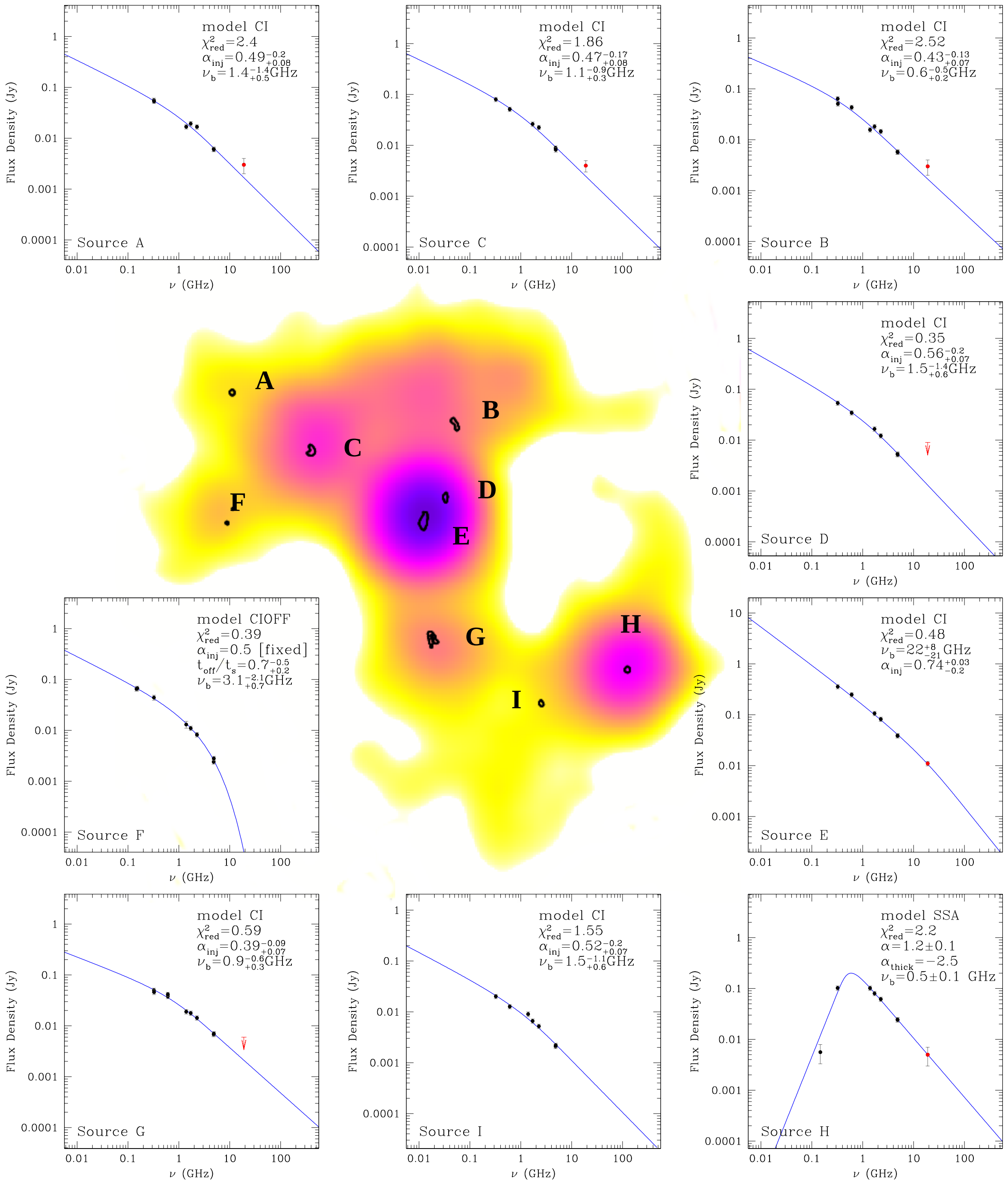

Figure 2.7 The image is the deep 6.6 GHz SRT total intensity map of the galaxy cluster CIZA J2242.8+5301 with VLA contours at 5 σ-level (σ=0.03 mJy/beam). Each plot around the image refers to the spectrum of the discrete source specified in the bottom left corner. Black points are the flux density measurements from GMRT, WSRT, WENSS, NVSS and VLA images, while red points indicate the 19 GHz SRT measurements (see text for details). The continuous blue line is the result of the fit whose parameters are reported in the top right corner of each panel.

at 6.6 GHz, and contours are from the VLA 4.8 GHz contours at 5 σ-level. We measured the flux density of each point-like source using a two-dimensional Gaussian fit, while for the extended sources we integrated the radio brightness down to the first isophote above the noise level.

In Table 2.4 we present the values obtained including a systematic error of 10% of the source flux, to take into account the different calibration scales of the images. Figure 2.7 shows the resulting spectra: in each panel the corresponding source is indicated in the bottom left corner with red dots indicating SRT 19 GHz measurements listed in Table 2.4 together with other measurements shown by black dots. Spectra are modelled by using the software SYNAGE (Murgia et al. 1999). The continuous blue line is the result of the fit using parameters as reported in the top right corner of each panel.

The spectra of A, B, C, D, E, G, and I are well described by a continuous injection (CI) model (Pacholczyk 1970), where the sources are continuously and constantly replenished with new relativistic electrons by the AGN and the power-law spectrum breaks due to energy losses caused by the synchrotron radiation itself and inverse Compton scattering with the Cosmic Microwave Background (CMB) photons. The CI model includes three free parameters: the injection spectral index, $\alpha_{\rm inj}$, that characterizes the spectrum below the break frequency, $\nu_{\rm b}$, and the normalization. Above $\nu_{\rm b}$, the high-frequency spectral index is $\alpha_{\rm h}$ which is related to the injected spectral index as shown in Eq. 1.19.

From these parameters we can evaluate the synchrotron age of the source $t_{\rm s}$, i.e. the time elapsed since the start of the injection, by using Eq. 1.20 and adopting the equipartition value $B_{\rm min}$ for the magnetic field strength (see Appendix B). Since this value depends on the source volume we derived $B_{\rm min}$ and hence the age only for the extended sources B, C, D, E and G. The results of the spectral modelling and the source ages are listed in Table 2.5.

Source A: It is point-like, the spectrum is fitted by a CI-model with $\alpha_{\rm inj} = 0.5$, and $\nu_{\rm b} = 1.4$ GHz. The observed spectrum includes SRT measurements at 19 GHz.

Source B: The spectrum for this source is described by a CI-model, with $\alpha_{\rm inj} = 0.43$ and $\nu_{\rm b} = 0.6$ GHz. It is a small double of 164 kpc in size. Assuming a cylindrical volume we calculated an equipartition magnetic field of $B_{\rm min} \approx 8.1\,\mu$G, and we deduce an age of $t_{\rm s}$=76 Myr.

Source C: This is a narrow-angle-tail source, seen in projection over the northern relic. The tail, which has a linear size of 146 kpc, extends toward the north-east. We calculate for this source an age of $t_{\rm s}$=70 Myr.

Source D: This source is seen in projection close to the cluster centre, and is slightly extended at the resolution of the VLA 4.8 GHz image. The spectrum is well fit by a CI-model. We estimate an age of 46 Myr.

Source E: This source is located in projection close to the cluster centre. Its morphology shows two bright lobes and two faint tails extending in the N-S direction. The spectrum is fitted by a CI-model with $\nu_{\rm b}$ =22 GHz and has an estimated age of $t_{\rm s}$=45 Myr.

Source	$S^{\rm mJy}_{\rm 323MHz}$	$S^{\rm mJy}_{\rm 325MHz}$	$S^{\rm mJy}_{\rm 608MHz}$	$S^{\rm mJy}_{\rm 1.4GHz}$	$S^{\rm mJy}_{\rm 1.7GHz}$	$S^{\rm mJy}_{\rm 2.2GHz}$	$S^{\rm mJy}_{\rm 4.835GHz}$	$S^{\rm mJy}_{\rm 4.885GHz}$	$S^{\rm mJy}_{\rm 19GHz}$	$[S^{\rm mJy}_{\rm 6.6GHz}]^{\rm exp}$
A	56±6	53±5	-	17±2	19±2	17±2	6.1±0.6	6.0±0.6	3±1	4.8
B	64±6	51±5	43±4	16±2	18±2	15±2	5.8±0.6	5.7±0.6	3±1	4.6
C	80±8	-	51±5	-	26±3	22±2	8.9±0.9	8.2±0.8	4±1	6.9
D	54±5	-	35±3	-	17±2	12±1	5.4±0.5	5.2±0.5	6±3	4.0
E	357±36	-	248±25	-	106±11	82±8	39±4	39±4	11±1	31.0
F	-	44±5	-	13±2	11±1	8.2±0.8	2.4±0.2	2.8±0.3	-	1.4
G	50±5	46±5	38±4	42±4	19±2	18±2	14±1	6.8±0.7	3±2	5.4
H	102±10	-	-	102±10	80±8	62±6	24±2	24±2	5±2	17.4
I	20±2	-	13±1	9±1	6.6±0.7	5.2±0.5	2.1±0.2	2.2±0.2	-	1.4

Table 2.4 Flux density measurements obtained from the following maps: GMRT 323 MHz (Stroe et al. 2013), WENSS 325 MHz (Rengelink et al. 1997), GMRT 608 MHz (Stroe et al. 2013), NVSS 1400 MHz (Condon et al. 1998), WSRT 1714 MHz (Stroe et al. 2013), WSRT 2272 MHz (Stroe et al. 2013), VLA 4835 MHz and 4885 MHz (van Weeren et al. 2010), SRT 19 GHz (this work). We report the expected flux density of each source at 6.6 GHz in the last column.

Source	Model	$\alpha_{\rm inj}$	$\nu_{\rm b}$ [GHz]	$\rm B_{min}$ [μG]	$\rm t_s$ [Myr]
A	CI	0.5±0.1	1.4±1.0	-	-
B	CI	0.4±0.1	0.6±0.4	8.1	76±36
C	CI	0.5±0.1	1.1±0.6	6.9	70±24
D	CI	0.6±0.1	1.5±1.0	8.4	46±22
E	CI	0.7±0.1	22±14	10.2	45±16
F	$\rm CI_{OFF}$	0.5	3±1	1.4	149±60
G	CI	0.4±0.1	0.9±0.5	3.6	166±58
H	SSA+PL	0.7±0.1	<0.54	-	-
I	CI	0.5±0.1	1.5±0.6	-	-

Table 2.5 Results of the spectral modelling and source ages.

Source F: This source is located at the Eastern tip of the northern relic. For this source we added the flux density measurements we derived from the 150 MHz TIFR GMRT Sky Survey (TGSS[4]) (Intema et al. 2017) and the WSRT 153 MHz (Stroe et al. 2013) images: $\rm S_{150MHz} = (65 \pm 6)\,mJy$ and $\rm S_{153MHz} = (67 \pm 2)\,mJy$. The radio spectrum shows a sharp high frequency exponential cut-off that cannot be explained by the smooth steepening of the CI-model. This source seems to be an example of a dying source where the central black hole of the galaxy has stopped its activity (Murgia et al. 2011). Following these authors, we fitted the radio spectrum using the $\rm CI_{OFF}$ model. This model assumes that the CI phase is followed by a remnant (or dying) phase during which the radio jets are switched off. In the absence of the injection of new electrons the sources spectrum develops an exponential high frequency cut-off. By fitting the $\rm CI_{OFF}$ model we derived the break frequency which gives the total source age, and $\rm t_{OFF}/t_s$, which gives the relative duration of the dying phase. We found a total source age of 149 Myr. The source has been in the active phase for 45 Myr and in the dying phase for 104 Myr. The morphology is relaxed, as expected for dying sources, but a weak point-like core is present. This weak core seems however to be disconnected from the fading lobes as no jets are visible.
Source F could be a potential source of seed electrons for the northern relic (e.g., Bonafede et al. 2014a; van Weeren et al. 2017). By looking at the top-right panel of Figure 2.2 we see that the source is close to an arc-like feature which appears to be a secondary shock or a possible extension of the northern relic, although a discontinuity between these two structures is present.

Source G: This is a narrow-angle tail with a linear size of 174 kpc. The spectrum is well described by a CI model, with $\nu_{\rm b} \approx 0.9\,\rm GHz$. The source age is 166 Myr from which we deduced an advancing speed for the galaxy of $\rm v = d/t_s = 1000 \pm 400 \cdot \frac{1}{\sin(i)}\,km/s$, where i is the inclination of the source with respect to the line-of-sight.

Source H: For this source we added the flux density measurement derived from the 150 MHz TGSS image: $\rm S_{150MHz} = (5.6 \pm 2.3)\,mJy$. This source exhibits a spectral turn-over at low frequencies, that could be due to synchrotron self-absorption (SSA). In the optically thick part of the spectrum we fixed the spectral index to $\alpha_{\rm thick}$=-2.5, while we modelled the optically thin regime using a power-law. The source is unresolved and could be intrinsically a compact steep spectrum source where the break frequency is below the SSA peak: $\nu_{\rm b} \ll \nu_{\rm SSA}$.

---

[4] http://tgssadr.strw.leidenuniv.nl/doku.php

For this reason the observed spectral index in the optically thin part of the spectrum is interpreted as $\alpha = \alpha_{\rm inj} + 0.5$.

Source I: The spectrum of this source is well fit by a CI model with the break at 1.5 GHz and $\alpha_{\rm inj} \approx 0.5$. The source is point-like.

From the fitted spectra we derived the flux density of the sources at $\nu = 6.6$ GHz and report these in the last column of Table 2.4.

Flux density measurements of diffuse sources

As mentioned in the introduction, single-dish telescopes can be used to accurately infer the size and flux density of diffuse sources. They are not affected by the missing zero spacing problem that plagues radio interferometers, especially at high frequency where the primary beam is usually smaller than the cluster size in the local Universe. Unfortunately, the typical beam of single-dish telescopes is far larger than the beam synthesised by the interferometer, so it is difficult to distinguish between diffuse and discrete sources.
Thanks to the spectral modelling of the discrete sources from the previous section we have a firm prediction of their flux densities at 6.6 GHz (see last column of Table 2.4).
We modelled these sources with Dirac delta functions normalized to the expected fluxes. We then convolved these functions with the SRT beam and finally we subtracted the resulting image from our SRT 6.6 GHz image.
Figure 2.8 shows in grey-scale and magenta contours the total intensity deep image on the right and, on the left, the image with the sources subtracted, where we expect to observe the contribution of diffuse emission only. The noise is $\sigma = 0.5$ mJy/beam. Both images show yellow contours of the combined image at 1.4 GHz presented in Figure 2.2. At the 3σ-level the northern emission seems to extend beyond the strong galaxy C covering a total extension of ~2.9 Mpc and a width of ~800 kpc. However, the extra-component in the north-east direction could be either due to a real extension of the northern relic or to the residual flux from source F (see notes on Sect. 2.3.3). For these reasons, and to be consistent with the other measurements (see Fig. A1 of Stroe et al. 2016), we evaluated the northern relic flux density inside the ellipse drawn with a dashed line in Figure 2.8. At the 5σ-level (a cut consistent with that of Kierdorf et al. 2017), we found $S_{6.6\rm GHz} = (17.1 \pm 1.2)$ mJy.
From Figure 2.8 we can also give an estimate of the flux of the southern relic at 6.6 GHz. We measured a flux density of $S_{6.6\,\rm GHz} = (0.6 \pm 0.3)$ mJy at the 3σ-level.

2.3.4 Northern and southern relics

Our results regarding the flux of the northern relic are reported in Table 2.6 together with flux density measurements at different frequencies taken from literature up to 8.4 GHz. We included the value we inferred from the WENSS 327 MHz image after the subtraction of sources A, B and C, using the flux densities predicted by our models at 327 MHz.

In Figure 2.9 we plot the values of Table 2.6. The red points represent our measurement obtained with the SRT observations. We fit the spectrum of the northern relic with a continuous injection model (blue line). This model takes into account the presence of relativistic particles injected at early stages of the shock passage that have lost their energy resulting in a break in the spectrum. From the fit we obtain a value of the injection spectral index $\alpha_{\rm inj}$. This value is related to the spectral index $\alpha_{\rm h}$ as already shown in Eq. 1.19.

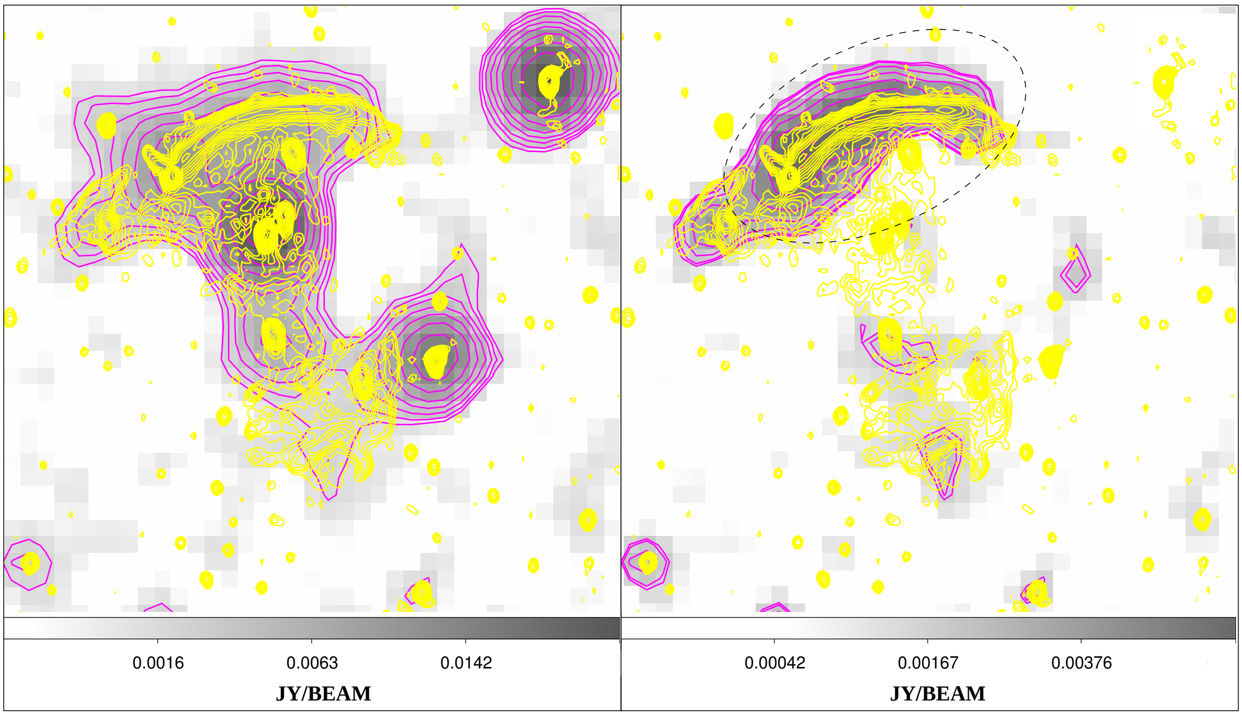

Figure 2.8 *Left:* The original SRT image at 6−7.2 GHz (colour-scale + magenta contours) overlaid with the higher resolution WSRT+SRT 1.4 GHz contours (yellow). *Right:* The residual 6−7.2 GHz image of the diffuse emission after the subtraction of modelled discrete sources (see text for details). Again the WSRT+SRT 1.4 GHz contours are overlaid in yellow.

ν [GHz]	S_ν [mJy]	Reference
0.15	780.4±80	Stroe et al. (2016)
0.325	315.7±32.4	Stroe et al. (2016)
0.327	446±21	This work, WENSS image
0.61	222.3±22.4	Stroe et al. (2016)
1.2	125.7±12.6	Stroe et al. (2016)
1.4	126±8	This work, SRT image
1.7	91.2±9.2	Stroe et al. (2016)
2.25	61±3.6	Stroe et al. (2016)
2.3	54.3±5.6	Stroe et al. (2016)
4.85	32±8	Kierdorf et al. (2017)
6.6	17.1±1.2	This work, SRT image
8.35	17±5	Kierdorf et al. (2017)

Table 2.6 Flux density measurements of the northern relic of CIZA J2242.8+5301.

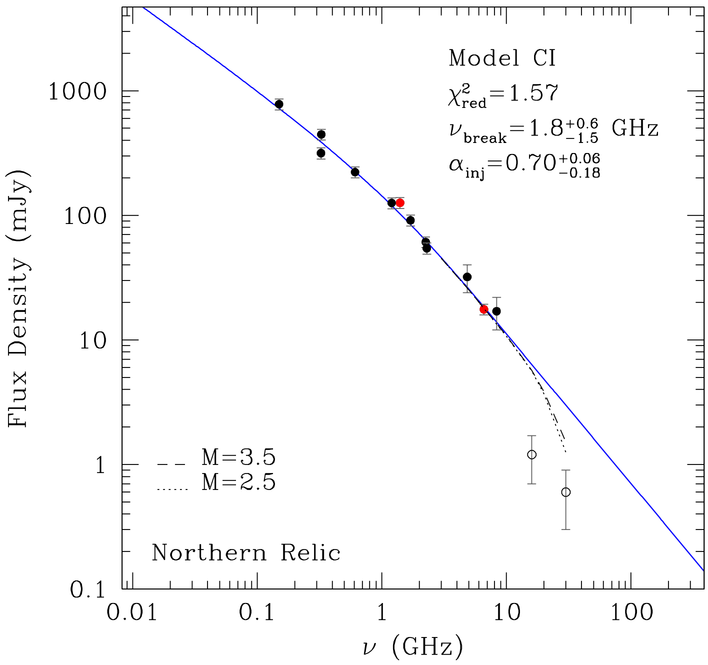

Figure 2.9 Total flux measurements of the northern relic at different frequencies from Table 2.6. Red points are the new measurements from this paper obtained with the SRT observations. The blue line represents the continuous injection model fit whose parameters are shown in the top-right corner of the image. Dot and a dashed lines have been drawn to show the flux density decrement due to the SZ effect as predicted for the northern relic of CIZA J2242.8+5301 by Basu et al. (2016) assuming M=2.5 and M=3.5 respectively.

From the fit we know that the spectrum breaks at $\nu_{\rm b} = 1.8^{+0.6}_{-1.5}$ GHz and that $\alpha_{\rm inj} = (0.7{\pm}0.1)$, in agreement with van Weeren et al. (2010). In the high-frequency region of the spectrum ($\nu >> \nu$b), where radiative losses are balanced by the injection of new particles, the resulting spectral index is $\alpha_{\rm h} = (1.2 \pm 0.1)$. By applying the simple DSA model formula of Eq. 1.27 we inferred a Mach number $M = (3.3 \pm 0.9)$ in agreement within the errors of the value $M = 2.7^{+0.7}_{-0.4}$ presented in Akamatsu et al. (2015). However, we noticed that there is not yet a clearly detected jump in the X-ray surface brightness as expected at these Mach numbers (Donnert et al. 2017) (see discussion in Sect.2.1).

In the frequency range probed by our observations no significant evidence of steepening in the radio spectrum is found beyond that predicted by the CI model. From our analysis based on a wide frequency range (from 150 MHz to 8.35 GHz) we can exclude the steepening found by Stroe et al. (2016) beyond 2.5 GHz. Moreover, we find that the continuous injection model is consistent with the data. Thus, the physics of the northern relic of CIZA J2242.8+5301 does not seem to require models beyond the standard DSA mechanism, although only new accurate measurements at frequencies higher than 10 GHz can definitively exclude alternative scenarios.

It should be noted that Stroe et al. (2016) presented interferometric measurements at 16 GHz and 30 GHz taken with the Arcminute Microkelvin Imager (AMI) and with the Combined Array for Research in Millimeter-wave Astronomy (CARMA). These measurements are represented as open dots in Figure 2.9. We do not include them in our fit procedure since these measurements are made with interferometers that could have lost a significant fraction of the flux density from the extended structure. Nonetheless, we compare them with the best fit of the CI model taking into account the SZ decrement. Extrapolating the CI model at frequencies higher than 10 GHz we show as a dot and dashed lines in Figure 2.9 the SZ decrement as expected by Basu et al. (2016) for this relic assuming a Mach number of M=2.5 and 3.5 respectively.

As we can see, the decrement is negligible, or at least within the flux calibration uncertainties until ∼16 GHz. Above this frequency the SZ decrement is increasingly significant, but not enough to explain the measurements at 16 and 30 GHz.
The observed gap could be due to a missing flux problem, as previously mentioned, or it could be real. In the latter case a modification from the basic CI model is required. Donnert et al. (2016) showed that a non uniform magnetic field in the region of the relic could explain the flux densities measured at 16 and 30 GHz. Future single-dish observations at frequencies higher than 10 GHz, which could be obtained with the SRT 7-feed K-band receiver, could help to shed light on the claimed high frequency steepening.

It should be noted that the break frequency of the CI model corresponds to the spectral break of the oldest electron population injected only if the particles are confined within the volume of the radio source, and the radio spectrum is extracted from a region that encloses the entire emitting region. In this case, we can think at the CI model as the sum of all electron populations from the youngest to the oldest ones. Below the break frequency (where radiative losses are negligible) particles accumulate and the source luminosity grows linearly with time. Above the break frequency a steady state is reached and the high-frequency spectrum stays unchanged since radiative losses are compensated by the freshly injected particles (Kardashev 1962; Pacholczyk 1970). If the magnetic field has been constant in time and uniform in space inside the radio source we can use Eq. 1.20 to estimate the time since the start of the injection, provided that we know the magnetic field strength. This assumption was used to estimate the ages of the discrete sources embedded in the diffuse emission in Section 2.3.3. However, this basic scenario needs to be modified if the confinement time $\tau_{\rm c}$ of the particles inside the source is finite which is likely the case for relics. We can make the oversimplified assumption that the shocked region consists of a slab of enhanced magnetic field strength of width $\rm l_{relic}$. Particles are accelerated in the outer rim of the slab at the edge of the upstream region by the shock wave and then they flow and age backwards in the downstream region. As the particles exit the slab their radio emission rapidly disappears even at low-frequencies due to the drop in the magnetic field strength. Indeed, the confinement time is related to the relic width by $\tau_{\rm c} = \rm l_{relic}/v_d$, where $\rm v_d$ is the downstream velocity. Note that a similar argument has been advocated in Carilli et al. (1991) to explain the spectra of the hot spots in Cygnus-A, where particles are injected (or re-accelerated) at the termination shock inside the hot spots and then they back-flow into the radio lobes. By definition, the age of the oldest electrons still present in the relic region and that produce the spectral break seen in the CI spectrum should be exactly τ_c. The magnetic field strength inside the relic is not known, however, from Eq. 1.20 it can be shown that the maximum age allowed for the electrons is $\rm t_{max} = 62\,Myr$, which is obtained for $\rm B = B_{IC}/\sqrt{3} \simeq 2.7\,\mu G$. We highlight that this value is in agreement with the minimum energy field strength of $\rm B_{min} = 2.4\,\mu G$ estimated by Kierdorf et al. (2017). Therefore, by assuming a relic width $\rm l_{relic} \simeq 200\,kpc$ (Stroe et al. 2016), we can derive a lower limit for the downstream velocity of $\rm v_d > 3145\,km/s$ or

$\mathrm{M} > 3$. We note that this lower limit is high but still compatible, within the measurement errors, with the Mach number derived both from the X-rays and from the DSA model (see Eq. 1.27). It is reasonable to assume (see Sect. 2.4.2) that the ambient magnetic field in the proximity of the relic is of the order of $1\,\mu$G. Indeed, the average magnetic field strength inside the relic region would be amplified by a factor $\gtrsim 2$. This represents the average magnetic field strength in the compression region, while outside we suppose that the magnetic field drops to the background level. The particles that flow in the de-compressed region disappear rapidly, even at low frequencies, because of the drop in the spectrum normalization due to the weaker magnetic field. We stress that, according to this simple scenario, the break frequency of the CI model is not related to the time necessary to the shock to propagate from the cluster centre to the observed position ($\sim$0.5 Gyr), but rather it refers to the much shorter confinement time of the electrons inside the shocked region. Therefore, we cannot infer the total age of the relic (that however, we can assume to be larger than τ_{c}) since the very first injected particles are not contributing anymore to the current observable radio spectrum. We underline that in this calculation we assumed that the magnetic field strength profile is described by a simple step function. A more detailed treatment of this issue is beyond the scope of this work; we refer to Donnert et al. (2016) for a more sophisticated modelling. These authors consider much smoother profiles for the magnetic fields after the shock (resulting from their assumption of a small-scale dynamo in the downstream region), which results in a curvature for the high-frequency spectrum more pronounced with respect to that of the CI model.

In any case, it is important to point out that a steep-spectrum power-law behaviour is expected only if the confinement time is so long that the break frequency of the oldest population present in the relic region shifts below the lower end of the observed window. Attempts to fit the spectrum with a single power-law have been presented in Kierdorf et al. (2017). They found for CIZA J2242.8+5301 $\alpha = 0.90 \pm 0.04$ which is intermediate between α_{inj} and α_{h} in our fit. However, this value of spectral index leads to problematic results since the Mach number expected by the DSA model diverges. We therefore opt for the CI fit, under the assumption that the spectral curvature is real, since the missing flux problem is negligible below 1 GHz. This is confirmed by the finding that the flux density of the relic before and after the single-dish-interferometric combination is roughly the same at L-band.

Concerning the southern relic: we fitted our estimates of the flux density at 1.4 GHz and 6.6 GHz with a simple power-law as shown in Figure 2.10. Because only two experimental points were available the fit of the CI model is not applicable. The southern relic has a spectral index $\alpha \simeq 1.9$ corresponding to a Mach number of $M \simeq 1.8$. Even in this case the value is in agreement with that found by Akamatsu et al. (2015) ($M = 1.7^{+0.4}_{-0.3}$).

It is worth noticing that in a recent work Hoang et al. (2017) presented Low-Frequency Array (LOFAR) observations between 115.5 and 179 MHz of the diffuse sources of CIZA J2242.8+5301. Assuming the DSA model and by evaluating the injection spectral index in the upstream region, they find Mach numbers for the southern and the northern relics in agreement with the ones obtained from X-rays by Akamatsu et al. (2015) and consistent with our results.

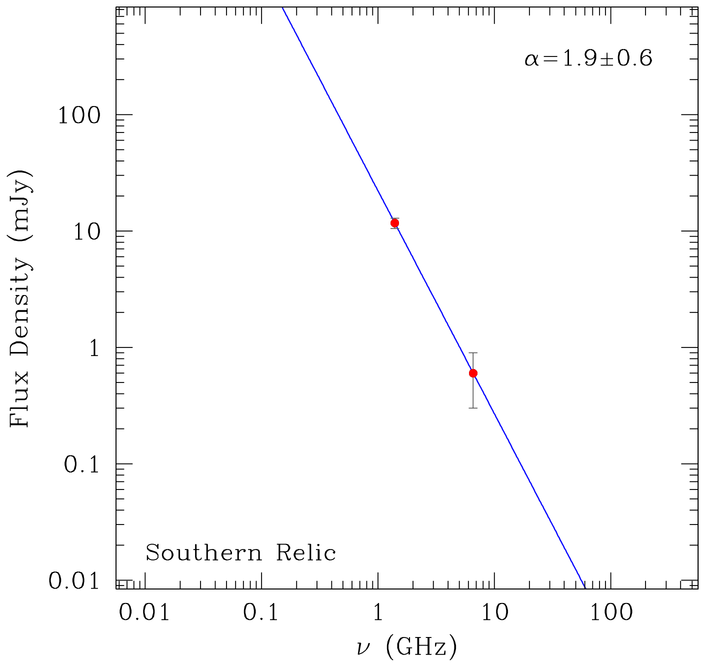

Figure 2.10 Total flux measurements of the southern relic obtained with the SRT observations.

2.4 Polarized intensity results

2.4.1 C-band

Figure 2.11 shows, on the left, the SRT 6.6 GHz linearly-polarized intensity image of CIZA J2242.8+5301 in colours as detected from the deep observations (FoV=$30' \times 30'$). Contours refer to the total intensity image (Figure 2.6) and vectors indicate the electric-field polarization. In this image the noise-level is σ=0.35 mJy/beam.
We detect the polarized emission of the northern relic: its average fractional polarization is of ∼40%, reaching levels as high as ∼70%. This could be a consequence of the shock passage - the turbulent magnetic field is compressed and its component in the direction of the shock is suppressed.

2.4.2 Rotation Measure Synthesis

We applied the Rotation Measure (RM) Synthesis technique (Burn 1966; Brentjens et al. 2005) on the linearly-polarized data presented in Figure 2.11 in order to recover the Faraday depth of the relic.
In addition to the SRT data, for which the frequency band goes from 6.0 GHz up to 7.2 GHz with a channel width ∼1.46 MHz, we also included two more channels taken from the archival VLA data at 4.835 and 4.885 GHz presented in Sect. 2.3.3. This helped us to improve the reliability of the RM Synthesis technique by extending the λ^2 coverage. We smoothed the VLA U and Q images to the SRT resolution. However, the resulting RM transfer function has still a quite large FWHM (∼4000 rad/m^2) since we are observing at relatively high frequencies. We should also consider that the angular resolution of our polarized images

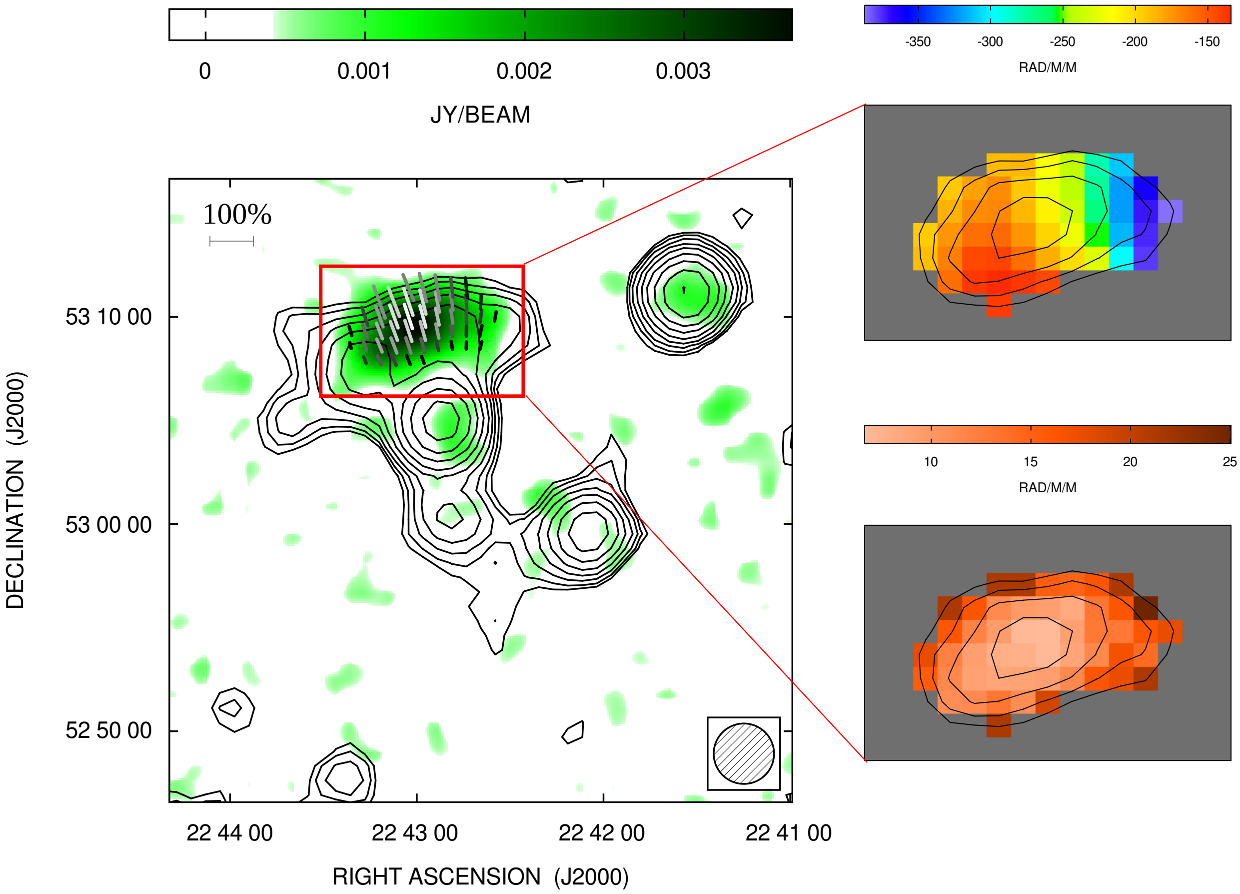

Figure 2.11 *Left:* SRT linearly-polarized intensity image of the galaxy cluster CIZA J2242.8+5301 obtained from the spectral average in the frequency range 6-7.2 GHz. The field-of-view of the image is $30' \times 30'$. The FWHM beam is $2.9'$ and is shown in bottom-right corner. The noise level is 0.35 mJy/beam. Contours refer to the total intensity image starting at the 3σ-level and increasing by factors of $\sqrt{2}$. The vectors indicate the electric field polarization with the orientation corresponding to the polarization angle and the length proportional to the polarization percentage where 100% is shown in the top-left corner. The vectors are traced only for pixels with a total and linearly-polarized intensity signal higher than 3σ and an error of the polarization angle below $10°$. *Right:* Result of the application of the RM Synthesis technique. The top panel represents the Faraday depth we obtained for the maximum polarized signal. In the bottom panel we report the associated uncertainties evaluated from simulations.

corresponds to a linear scale of ∼550 kpc, which could be larger than the autocorrelation length of the RM fluctuations. Indeed, it is hard to distinguish multiple components in the Faraday depth space and as a consequence we cannot verify if the RM originates internally to the radio relic or in an external Faraday screen. For these reasons, in what follows we assumed that the RM originates entirely in the ICM between us and the relic and that the internal Faraday rotation is negligible. In practice we considered just one polarized component in Faraday space and we computed its RM from the RM Synthesis by measuring the Faraday depth of the polarization peak.

Figure 2.11 shows, on the right, the results of the RM Synthesis applied on pixels with a polarized S/N ratio larger than 3. The top-right panel shows the resulting Faraday depth while the bottom-right panel shows the associated uncertainty.
These errors have been evaluated with a Monte Carlo simulation. We injected 30 different components in Faraday depth, randomly distributed between -10000 and $10000\,\mathrm{rad/m^2}$, with intensities ranging from 1 mJy/beam up to 4 mJy/beam to reproduce the S/N range of the observed polarization intensity. From these values we produced simulated U and Q data in the selected frequency band (SRT C-band plus the two VLA frequencies). We fixed the relic spectral index to what found in Sect. 2.3.4 and we assumed a weight w_{ch} for each frequency channel (defined as $w_{\mathrm{ch}} = 1/(\sigma^2_{\mathrm{ch}})$ where σ_{ch} is the rms of the single channel), in order to accurately reproduce the effect of the noise on data. We used $w_{\mathrm{ch}} = 0$ for those channels that have been blanked due to RFI. We applied the RM Synthesis to the simulated U and Q data and we compared the injected values with respect to the polarized signal and the Faraday depth inferred from the RM Synthesis. We assumed for the RM uncertainty the rms of the distribution of the difference between input and "measured" Faraday depth. As expected, the higher the S/N ratio the lower the rms. For a S/N=3 the RM uncertainty is about 25 $\mathrm{rad/m^2}$, but it decreases down to 7 $\mathrm{rad/m^2}$ at the position with the brightest polarized emission (S/N=10).

The Faraday depth image shows negative values with a gradient along the relic length from about -150 at the east end to about -400 $\mathrm{rad/m^2}$ at the west end. At the polarization peak we found $\mathrm{RM} = (-176 \pm 8)\,\mathrm{rad/m^2}$. Our Faraday depth image is in good agreement with the values obtained by Kierdorf et al. (2017), but we observe a RM gradient of $\sim 250\,\mathrm{rad/m^2}$ over an angular scale of $10'$, a factor of 2 larger than the gradient inferred from that work.

We estimated the Galactic RM contribution in the position of CIZA J2242.8+5301 using the reconstruction of Oppermann et al. (2015) that provides a $\mathrm{RM_{gal}} = (-73 \pm 70)\,\mathrm{rad/m^2}$. Therefore, despite the large uncertainties the Faraday depth shown in Figure 2.11 seems to exceed the Galactic contribution by at least a factor of two. Furthermore one could ask if the observed RM gradient is due to a gradient in the foreground Galactic RM since CIZA J2242.8+5301 is very close to the Galactic plane (latitude b=−5.11 deg). Using the map of Oppermann et al. (2015) we deduced that in general RM gradients as large as $1000\,\mathrm{rad/m^2/deg}$ are possible along the Galactic plane. In order to explain the RM gradient observed along the northern relic in CIZA J2242.8+5301 we would need a very high gradient of about $1500\,\mathrm{rad/m^2/deg}$.

We therefore deduce that the RM gradient is not due to the Galactic foreground. Thus, we can subtract the constant value of $\mathrm{RM_{gal}} = -73\,\mathrm{rad/m^2}$, and evaluate if the residual RM could be caused by the magneto-ionic medium in the galaxy cluster itself. Following Govoni et al. (2010) (see also Appendix C), and assuming a cluster magnetic field with an autocorrelation length $\Lambda_{\mathrm{B}} << \mathrm{L}$, where L is the integration path along the gas density distribution, the observed RM along a line-of-sight is a random walk process that involves a large number of cells with size Λ_B. The distribution of the RM will be a Gaussian with zero mean and a variance:

$$\sigma^2_{RM} =< RM^2 >= (812)^2 \Lambda_B \int_0^L (n_e B_\parallel)^2 dl \tag{2.1}$$

Assuming that the cluster magnetic field follows a η-profile with respect to the density distribution $B(r) = B_0(n_e(r)/n_0)^\eta$ and that the density distribution follows a β-profile $n(r) = n_0(1 + r^2/r_\perp^2)^{-3\beta/2}$, we obtain that the RM dispersion at a given projected distance $r_\perp$ is:

$$\sigma_{RM}(r_\perp, L) = \frac{K(L) B_0 \Lambda_B^{1/2} n_0 r_c^{1/2}}{(1 + \frac{r_\perp^2}{r_c^2})^{\frac{6\beta(1+\eta)-1}{4}}} \sqrt{\frac{\Gamma[3\beta(1+\eta) - \frac{1}{2}]}{\Gamma[3\beta(1+\eta)]}} \tag{2.2}$$

where K(L) depends on the integration path along the gas density distribution. We assume that the northern relic is located halfway the cluster so that K=441. B_0 and n_0 are respectively the central values of the magnetic field and thermal plasma density profiles, r_c is the core radius of the cluster and Γ is the gamma function. The observed RM image is compatible with a magnetic field tangled on a scale equal or larger than the RM structure of Figure 2.11, so that we can assume $\Lambda_B \sim 1300\,\mathrm{kpc}$. If we subtract from the RM of the peak the Galactic contribution the residual RM due to the ICM is $\mathrm{RM} = -103\,\mathrm{rad/m^2}$. Assuming reasonable values for the parameters of the hot ICM ($n_0 = 10^{-3}\,\mathrm{cm^{-3}}$, $\beta = 0.6$, and $r_c = 500\,\mathrm{kpc}$), we would need a magnetic field of $B_0 = 4.5\,\mu\mathrm{G}$ at the cluster centre with $\eta = 0.5$ to generate an RM distribution with a $\sigma_{\mathrm{RM}} \sim 107\,\mathrm{rad/m^2}$ at the relic, where we expect $\mathrm{B} = 1.6\,\mu\mathrm{G}$. We note however that even if the central magnetic field strength is in line with what typically found at the centre of galaxy clusters (Feretti et al. 2012), the magnetic field autocorrelation length is much larger than what expected for the turbulent ICM. We also note that the condition $\Lambda_B << \mathrm{L}$ could not be verified in our case, since the scale of the magnetic field would be comparable with the size of the cluster.

Another possibility is to consider that the Faraday rotation is occurring in a cosmic web filament which includes CIZA J2242.8+5301. As suggested by Planck Collaboration et al. (2016) the primordial magnetic fields have a strength not larger than a few nG. Even assuming a thermal density of $n_e = 10^{-4}\,\mathrm{cm^{-3}}$ and a magnetic field tangled on a scale of 1300 kpc, the resulting RM would be only $\sim$0.1 rad/m^2, making the filament contribution irrelevant. Moreover we notice that magnetic fields of the order of $\sim 0.1\,\mu\mathrm{G}$ in filaments should be reached only in the presence of small-scale dynamo amplification in excess of what can be presently resolved by simulation (Vazza et al. 2015). This may be verified in the presence of small-scale vorticity and/or plasma instabilities of various kinds (e.g. Mogavero & Schekochihin 2014), which would however make the magnetic field tangled on much smaller scales than what is inferred by our observations.

For this analysis it is clear that high resolution polarized observations are needed to clarify the nature of the observed Faraday rotation in CIZA J2242.8+5301. For instance the forthcoming Westerbork Observations of the Deep APERTIF Northern-Sky (WODAN, Röttgering et al. 2011) project will give us a polarized image of the northern sky. The high resolution and sensitivity of this survey will make it possible to better investigate the RM observed in the region covered by the galaxy cluster CIZA J2242.8+5301 and will help to constrain the properties of the intracluster magnetic field.

3

Full-Stokes simulations of the radio sky

The advent of the Square Kilometre Array will have an unprecedented impact on the study of the cosmic magnetism. An all-sky survey at 1.4 GHz will be proposed for the SKA with the aim to produce an accurate map of the RM based on a enormous number of radio sources spread over cosmological distances. The spatial density of these radio sources will be such that we will obtain a RM grid with several hundreds of sources per squared degree. In order to be prepared to use this RM grid, we need to understand if and how we will be able to invert the information encoded in the grid to reconstruct the strength and the structure of intracluster magnetic fields. To this purpose, we first develop a numerical approach that is able to produce a realistic image in full-Stokes of the radio sky. As a second step, we use these realistic images of the radio sky, in combination with numerical model of the intracluster medium, to produce synthetic radio observations similar to the images of galaxy clusters that will be obtained with the SKA. Finally, these mock spectral-polarimetric cubes are used to determine the precision of the RM Synthesis technique in reconstructing the properties of the intracluster magnetic fields.

In this Chapter we describe the procedure and the models developed to produce simulated full-Stokes images of the radio sky. The predictions of our modelling will be compared with the radio source counts both in total intensity and polarization available from the literature. Finally, we present the estimates of the confusion limits of I, U, and Q Stokes parameters versus different values of beam resolutions obtained from our simulations.

3.1 Modelling the radio sky

The physical characteristics of intracluster magnetic fields are encoded in the polarization properties of the radio sources located within and in the background of galaxy clusters.

As explained in Chapter 1, a linearly polarized signal suffers the Faraday rotation effect as it crosses a magneto-ionic medium. When we observe a polarized radio source located inside or in the background of a galaxy cluster, the rotation of the polarization plane (see Eq. 1.28) is equal to its wavelength squared times the Rotation Measure (RM). The RM is defined as the path integral of the intracluster magnetic field component parallel to the line-of-sight times the thermal density where the integral is performed throughout the portion of plasma crossed by the signal (see Eq. 1.29). Thus, it should be clear that the RM is crucial in determining the intracluster magnetic field properties provided that we have enough radio sources to cover the galaxy cluster area (see e.g. Sect. 1.4). Note that so far the majority of RM studies have been based on discrete radio sources, but thanks to its unprecedented sensitivity the SKA will permit to investigate also the Faraday rotation effect using diffuse sources, like radio haloes (Govoni et al. 2015, 2017).

In this thesis, we use the FARADAY software package (Murgia et al. 2004) which has been specifically designed for the study of the intracluster magnetic fields. This tool was already able to predict the polarization properties of the large scale diffuse emission associated to radio haloes (see Sect. 3.1.1 below). We further developed the FARADAY package to include the possibility to simulate a synthetic population of cluster-embedded discrete sources and also a synthetic population of background and foreground discrete sources distributed over cosmological distances (see Sect. 3.1.2). FARADAY is now able to produce full-Stokes spectral cubes that can be further analysed as if they were real observations of discrete radio sources. We use these new features to predict the distribution of the radio sources cosmological population with respect to redshift which is very important to understand the effectiveness of the RM grid for a galaxy cluster at a given distance. Finally, we present simulated I, U and Q images of the cosmological population of discrete radio sources in order to evaluate the confusion limit at different angular resolutions.

3.1.1 Radio haloes' simulations

In order to produce the signal of a radio halo we need a model for the ICM properties, namely the intracluster magnetic field, the thermal plasma density and the relativistic electron density. By using the FARADAY software package we can model a 3-dimensional distribution of the magnetic field and the thermal plasma density in a physical cube. FARADAY is able to reproduce specific physical properties like e.g. a particular power-spectrum for the magnetic field fluctuations or a given $\beta-$model for the thermal gas density. The software package is also able to accept physical cubes produced by external numerical magneto-hydro-dynamical (MHD) simulations. In both cases, once a given intracluster magnetic field is included in the physical cube we can illuminate it with a relativistic electron population. For the simulations presented in this thesis the energy of the relativistic electrons is set according to the equipartition condition (see Appendix B). FARADAY is able to compute full-Stokes spectro-polarimetric cubes. The total intensity emissivity resulting from the interaction between the relativistic electron population and the intracluster magnetic field is computed from the synchrotron formulas presented in Sect. 1.2. The total intensity will be the integral of the emissivity throughout the line-of-sight:

$$I(\nu) = \frac{1}{4\pi}\int_0^L j_\nu dl \tag{3.1}$$

where L is the dimension of the physical cubes of the ICM properties. It is worth to mention that FARADAY includes the k-correction factor $(1+\mathrm{z})^{-3-\alpha}$ to take into account the Doppler effect and the cosmological dimming of the brightness.

To compute the intrinsic polarized intensity P and angle Ψ we take into account both the internal depolarization effect and the variation of the magnetic field direction along the line-of-sight. We first evaluate the rotation which affects the intrinsic linearly polarized signal

$P_{\mathrm{int}}(\nu, \mathrm{l})$ emitted in a cell located at depth l:

$$\Delta\Psi(\nu, l) = RM(l) \times \left(\frac{c}{\nu}\right)^2 \tag{3.2}$$

where the RM(l) (in rad/m^2) is defined in Eq. 1.29. Hence, we compute the contributions to the Stokes parameters U and Q from the polarized signal emitted inside the cell by inverting the relations:

$$P(\nu, l) = \sqrt{U(\nu, l)^2 + Q(\nu, l)^2}$$
$$\Psi(\nu, l) = 0.5 \times \tan^{-1}\left(\frac{U(\nu, l)}{Q(\nu), l}\right)$$

The final images of U and Q are obtained by summing up all the contributions along a given line-of-sight incoming from every point inside the radio halo.

3.1.2 Discrete radio sources simulations

For this PhD project, the capabilities of FARADAY have been upgraded to reproduce the emission of a population of discrete radio sources.

The simulation begins with a catalogue of radio sources which is generated by integrating the selected luminosities functions over a large "conical" volume of space: the catalogue contains all the discrete radio sources inside the slice of Universe whose angular aperture is set by the field-of-view of the target cluster and that extends in depth from a redshift z=0 up to z=$\mathrm{z_{max}}$. This list is used to store the basic radio source properties i.e.: *type, size, position* (with respect to the cluster), *redshift, coordinates, luminosity*. In addition, to each source of the list we attach a *model* which is extracted from a *dictionary* and consists of four images: total intensity, spectral index distribution, fractional degree polarization, and intrinsic polarization angle. These images are derived from real observations of radio sources. Some examples are shown in Fig. 3.1 where the colour represents the total intensity and the vectors the electric field polarization direction and strength. Furthermore, with FARADAY it is possible to divide the population into different *types* of radio sources (i.e. radio-loud, radio-quiet, star forming galaxy, quasar etc.). For simplicity, we decided to opt for two main families depending on the mechanism that triggers the radio emission: star forming galaxies (SFG) and active galactic nuclei (AGN). To the AGN class we associate powerful and polarized radio sources with different morphologies (FRI, FRII, Head-Tails..), while for the SFG class we use maps of spiral galaxies. The radio source models are all derived using high-quality high-resolution images. Indeed, the images of fractional polarization and angle of the radio sources included in our dictionary are derived from VLA images at C and X bands at arcsecond resolution so that they can be considered very closed to the intrinsic values. The SFG and AGN *sizes* are assigned, according to their luminosity and redshift, consistently with the prescriptions of Wilman et al. (2008).

For each source, the total intensity of the model $\mathrm{I}_\nu(\mathrm{x}, \mathrm{y})$ randomly extracted from the dictionary is rescaled such that the total luminosity:

$$L_\nu = \int_\Sigma I_\nu(x, y) dx dy \tag{3.3}$$

matches to that required by the catalogue, where the integral is performed over the radio source area Σ.

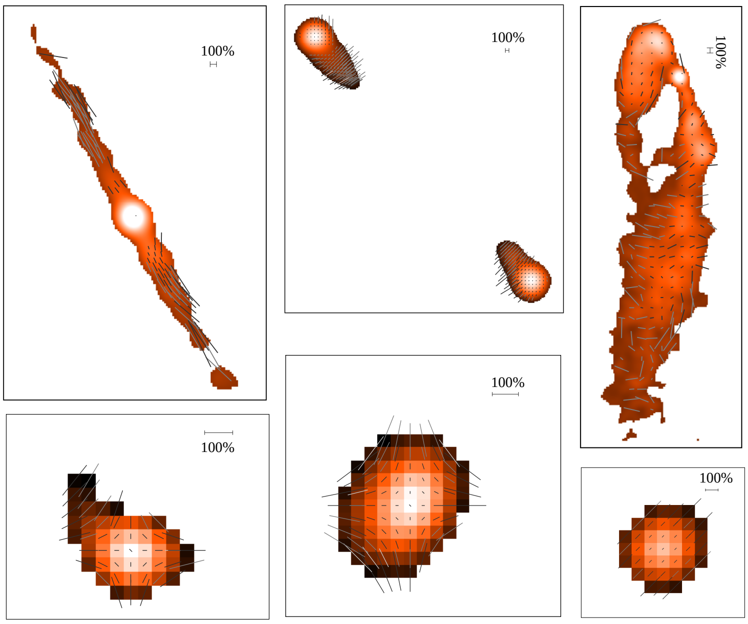

Figure 3.1 Models of radio galaxies where the colour represent the total intensity (normalized to one) and the vectors the intrinsic polarization strength.

From an operative point of view, the generation of the catalogue is generally based on a Monte Carlo extraction. However, there are some differences between the cluster-embedded and the cosmological population.
For what concerns the cluster-embedded radio sources, we follow these steps:

1) we choose a value for r_{200}, defined as the distance within which the cluster density is 200 times the critical density of the Universe;

2) for numerical purposes, we define the cluster volume as a cubical box of few Mpc^3;

3) we assume that the spatial distribution of the radio sources follows a Navarro-Frank-White profile (Lin & Mohr 2007);

4) we assume as radio luminosity function (RLF) that proposed by Lin & Mohr (2007);

5) we normalize the Navarro-Frank-White distribution such that it yields the same number of sources per Mpc^3 provided by the RLF;

6) the total number of cluster sources N is computed from the integration of the spatial distribution over the cubical box;

7) we select the relative fraction of AGNs and SFGs depending on the ratio between the RLF of one specific type (AGN or SFG) with respect to the total RLF;

8) by using a Monte Carlo approach we randomly extract the position (x,y,z), the luminosity, and the size of each source;

9) a model for the radio source is extracted from the dictionary according to the luminosity and type.

The distribution of the non-cluster radio sources is computed starting from a "cosmological" RLF. First, we set the field-of-view and the maximum redshift up to which we populate the simulated portion of the Universe. We split the slice into sub-volumes of $\Delta z = 0.01$ in width. We choose the local RLF of Condon (1984) evolved at higher redshifts with a the pure luminosity evolution represented by a power law: $L(z) = L(0) \cdot (1+z)^{\gamma_L}$. Following Condon (1989), we set $\gamma_{\mathrm{L}} = 4.7$ for both the AGN and the SFG RLFs letting the RLFs evolve from the local Universe until z=3. We perform the integral of the AGN and SFG RLF throughout the solid angle of the simulated observation sub-volume by sub-volumes: the result is the total number of "cosmological" AGN and SFGs respectively. The radio source *redshift* of each specific type is assigned through a Monte Carlo extraction depending on the corresponding RLF evolution. We populate each sub-volume, by randomly extracting the (x,y) coordinates, the size, the luminosity, and the model by following the same procedure adopted for the cluster-embedded radio galaxies.

At this point we have a list that contains cluster, foreground and background radio sources and all their properties. Starting from this information, FARADAY is able to create a spectral-polarimetric cube with the given pixel size over a given bandwidth at the specified spectral resolution for each of the Stokes parameters I, U, and Q. In this process, the algorithm considers the right spectral index for each pixel according to the dictionary.

By multiplying the intrinsic total intensity for the fractional degree polarization maps we obtain the intrinsic polarized intensity of the selected radio galaxy. We neglect the effect of the Galactic RM and we assume that no other magnetized plasma are inside the simulated slice of Universe, except those associated to the simulated galaxy clusters. Therefore, the polarized intensity of foreground radio sources corresponds to the intrinsic one, while the polarized intensity of a background or a cluster radio source depends on the amount of the magneto-ionized plasma crossed by the polarized signal. In the case of a background radio source, the intrinsic polarized signal is rotated as shown in Eq. 1.28 where the RM integral is performed over the full path length of the cluster magneto-ionic plasma. For cluster-embedded radio sources the depth of the magneto-ionic plasma crossed has to be calculated case by case depending on the source position with respect to the cluster centre.

3.2 Comparison with data

To double-check the reliability of our simulations we make some comparisons with total intensity and polarization source counts available from the literature.
In Fig. 3.2, we plot the differential source counts of our simulated radio source population together with those estimated from data. The counts are euclidean normalized[1] and the data refers to counts taken at 1.4 GHz (White et al. 1997; Prandoni et al. 2001; Bondi et al. 2003, 2008; Kellermann et al. 2008; Hales et al. 2014; Vernstrom et al. 2014). The flux density is evaluated taking into account the k-correction:

$$S_\nu = \frac{L_\nu}{4\pi D_L^2} \cdot (1+z)^{1-\alpha}$$

where $\mathrm{D_L}$ is the luminosity distance, z the redshift and α the spectral index of the radio source. As showed in the plot, the simulated differential counts (black points) are in quite

---

[1] the source counts are normalized with respect to an Euclidean Universe, i.e. the number N of source depends on their flux densities S as $\log \mathrm{N} = \mathrm{S}^{2/5} \log \mathrm{S}$

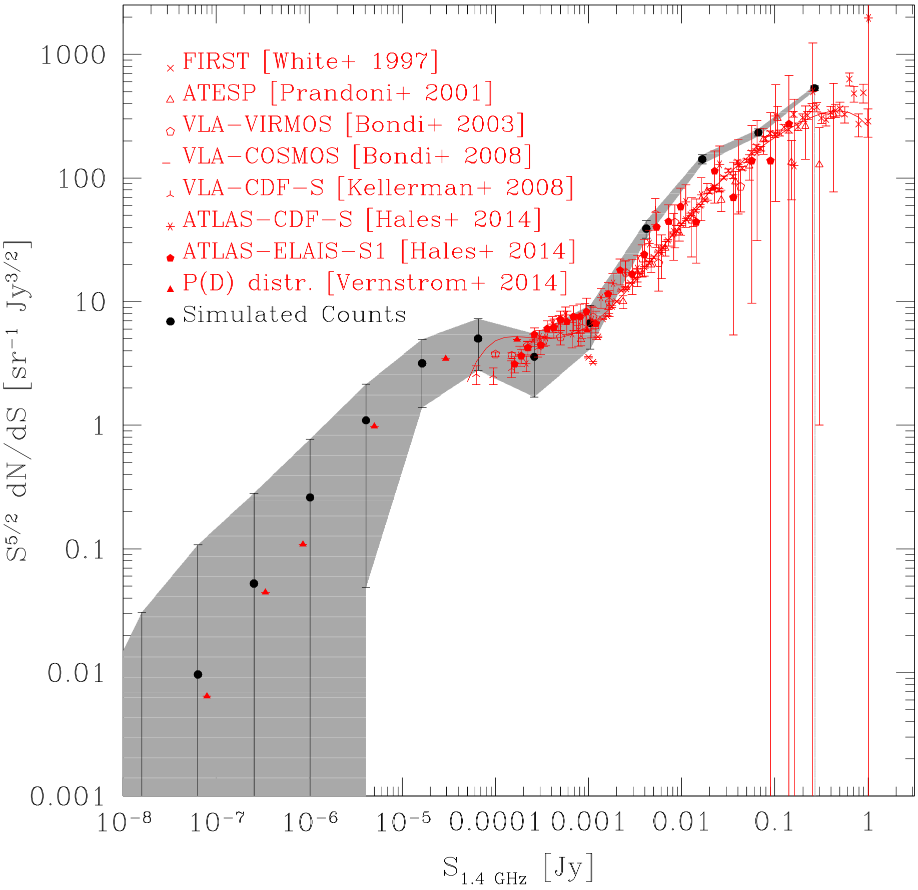

Figure 3.2 Euclidean-normalized source counts at 1.4 GHz: the red points represent the data (White et al. 1997; Prandoni et al. 2001; Bondi et al. 2003, 2008; Kellermann et al. 2008; Hales et al. 2014; Vernstrom et al. 2014) while the black ones show the values obtained from a simulation with the FARADAY software package.

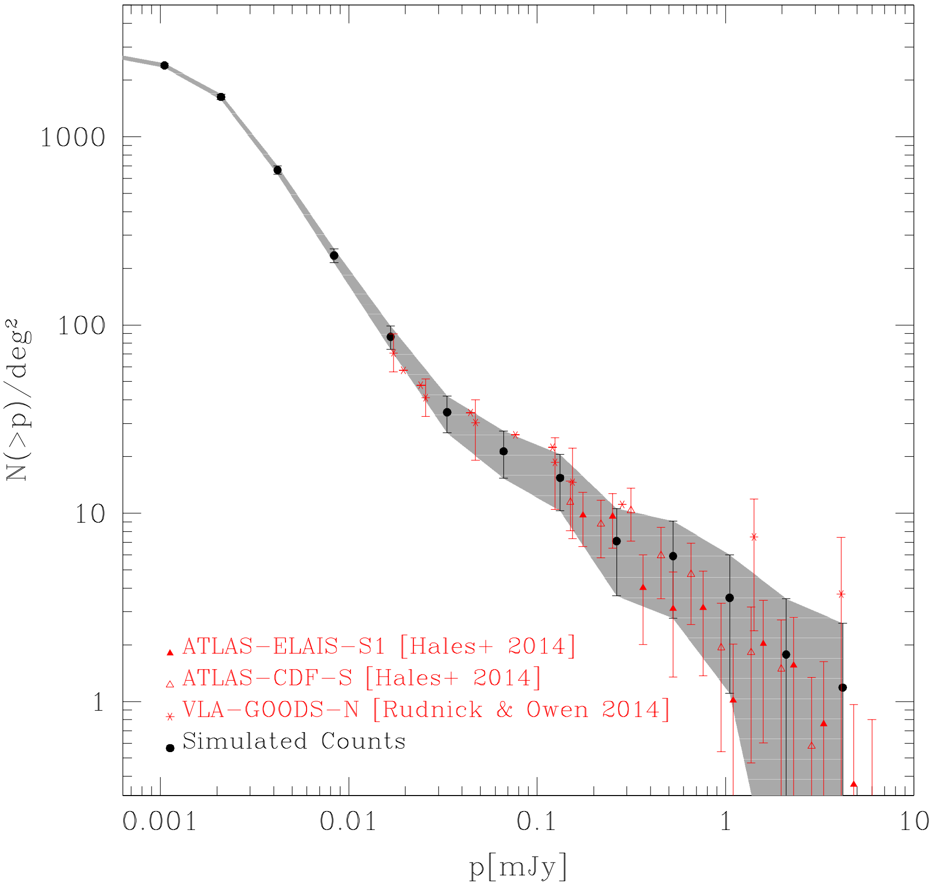

Figure 3.3 Cumulative counts of polarized sources with respect to the polarization. The red points refers to the data of the GOODS-N field (Rudnick & Owen 2014) while the black points represent the results of a simulation obtained with the FARADAY software package.

good agreement with data, although we can appreciate differences especially at . Moreover these kind of simulation gives us the chance of explore the sub-mJy region, that will be accessible with the next generation radio telescope like the SKA over larger field-of-views. In Fig. 3.3, we show the cumulative counts of polarized sources with respect to the polarization. The red points are the results of the GOODS-N field presented by Rudnick & Owen (2014) while the black points are the cumulative counts obtained from a simulation obtained with the FARADAY software package. We appreciate a good match between the data and the simulation.

3.3 Predicted source number density and filling factors as a function of cluster redshift

In Figure 3.4, (top panel) we plot the predicted number density (per deg^2) of foreground and background sources as a function of the cluster redshift. We take into account only sources with flux densities $S_{1.4\mathrm{GHz}} > 20\,\mu$Jy. The red and the blue colours are used to represent the background and foreground sources respectively, the dotted lines and the triangles refers to

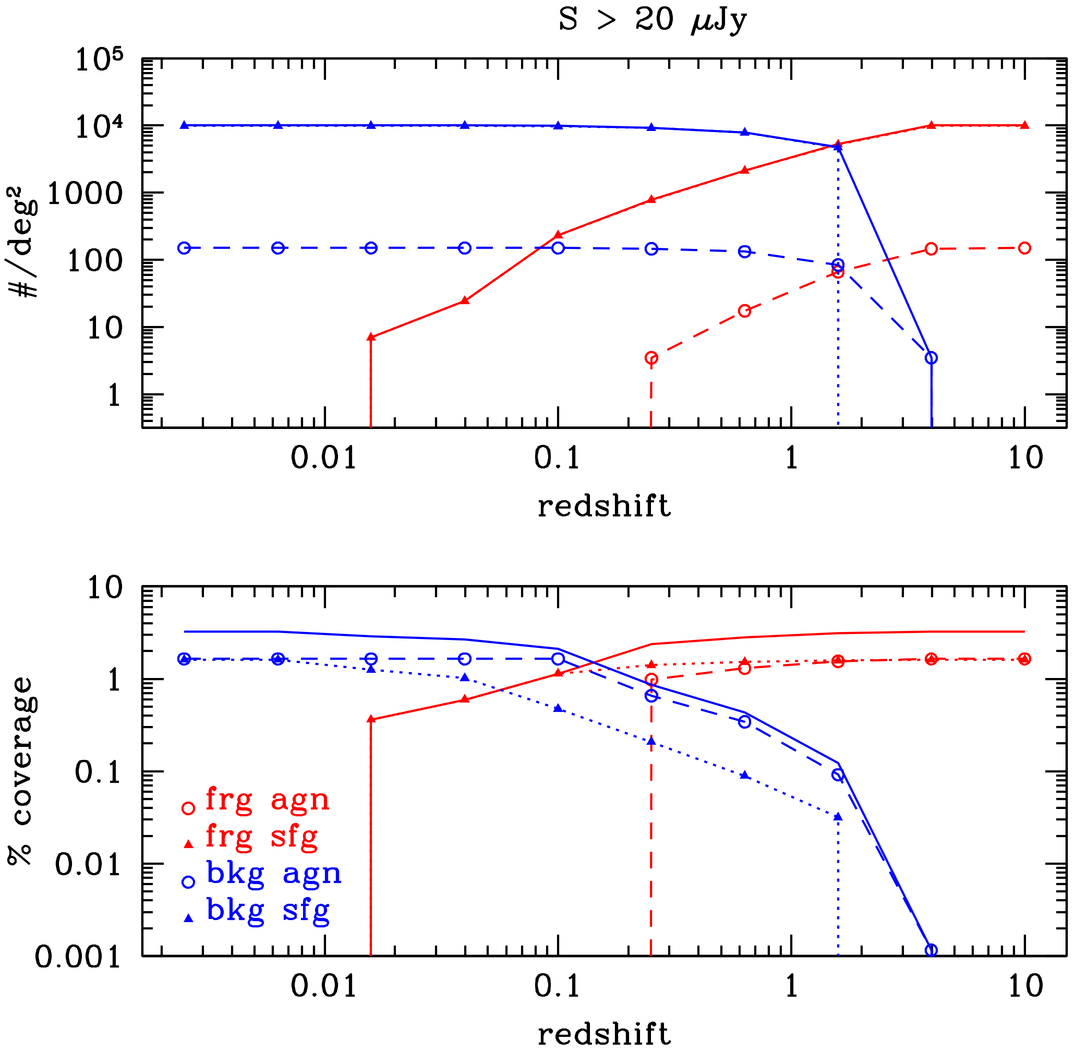

Figure 3.4 *Top panel:* the simulated number per deg^2 of radio sources with density flux $S_{1.4\mathrm{GHz}} > 20\,\mu$Jy for cluster at different redshifts. *Bottom panel:* percentage of the field-of-view covered by the radio source area with density flux $S_{1.4\mathrm{GHz}} > 20\,\mu$Jy for cluster at different redshift values. Both panels use the same code colours and symbols: the red and the blue colours are used to represent the foreground and background sources respectively, the dotted lines and the triangles refers to SFGs while the dashed line and the empty points are used for the AGNs, the solid lines indicate the total contributions of the two radio source populations.

SFGs while the dashed line and the empty points are used for the AGNs. The solid lines are the total contributions of the two radio source populations.
As we expect, foreground sources are negligible for low redshift clusters and become relevant for cluster at higher redshift. Vice versa, the background population dominates for clusters at low redshift and it is less important for high redshift clusters.

This expectations can be used to draw some statistical considerations about intracluster magnetic fields investigations. For instance, we infer from the top panel that an observed image will be dominated by the contribution of foreground galaxies for clusters placed at redshift $z \gtrsim 1.5$. Indeed, at z=1.5 the foreground component is equal to the background one and at larger redshift values it prevails. If we want to study the magnetic field with the RM we need a high number of background sources and few foreground sources. Thus, from a statistical point of view it appears that we can best recognize the cluster contribution to the observed RM, if its redshift is $z \lesssim 0.015$.

However, also the field-of-view source filling factor depends on redshift and this also has an impact on RM studies. As we show in the bottom panel of Fig. 3.4, the intersection between the percentage of field-of-view coverage of foreground and background sources takes place at $z \sim 0.15$ for the overall population, at $z \sim 0.25$ for AGNs and, at $z \sim 0.06$ for SFGs.

From the above considerations we can state that the RM grid of an all-sky survey should statistically give reliable cluster RM contributions for clusters with redshift lower than $z \sim 0.06$ or at least lower than $z \sim 0.15$. This holds assuming a detection threshold of $S_{1.4\mathrm{GHz}} = 20\,\mu$Jy while for different sensitivity levels the redshift values can significantly change.

3.4 Simulations of confusion limits in total and polarized intensity

The possibility to simulate all the radio sources that are present in a given field-of-view let us explore an important observational limit known as confusion limit.
When we observe a “cold” part of the sky we still detect a residual noise even if we observe for a long time which can significantly reduce the thermal noise of our observations. The residual noise is due to the faint unresolved radio sources whose signal enters inside the beam of the telescope and we refer to this as confusion. While we can reduce thermal noise by extending the exposure time, the confusion is a physical limit that we cannot overcome and it is important to have a precise estimate of its statistical properties. The distribution of the confusion source densities as a function of flux densities is obviously not Gaussian-like but it presents a long tail at high flux densities due to bright sources. It is important to stress that in total intensity the spatial distribution of confusion sources over a large region of the sky would form a plateau characterized by a mean different from zero. However, this base level cannot be observed in the interferometric images due to the missing short space baselines in the u-v plane. Also in single−dish images the plateau is hardly observed since it is removed by the baseline subtraction. Thus, what we observe in general is the fluctuating component of the confusion. In any case, the distribution of these fluctuations is highly non-Gaussian because of the presence of the high luminosity tail.

In total intensity the properties of the confusion noise have been extensively studied in literature, and we refer to the seminal works by Condon (1974, 2002), and Condon et al. (2012). However, the polarization confusion noise is less studied probably because it requires a numerical approach to evaluate the net polarized flux density within a Gaussian beam. The simulation framework developed in this thesis allows us to explore this issue.

Here, we simulate the Stokes parameters of a radio source population in a computational grid of 3074×3074 pixels with a cell size of 1″. The data are produced in a bandwidth of 810 MHz divided in 512 channels and centred at 1.355 GHz, i.e. the SKA1-MID band 2. The radio source population is composed only by external radio sources, no galaxy clusters are simulated and thus we are not reproducing the signal of cluster-embedded radio sources or radio haloes. Moreover, we do not reproduce the effect of a magnetic field. The resulting images have been convolved with different beam sizes. In particular we consider FWHM=1″, 2″, 6″, 10″, 20″, 45″, 60″, 120″, 900″.
Fig. 3.5 shows from left to right the I, U, and Q images convolved, from top to bottom, with a FWHM=1″, 45″, and 60″. To estimate the confusion we measure the average and the rms with an iterative procedure: considering a box centred in the images centre and with a width of 2800 pixels we evaluate the rms by clipping iteratively all the pixels having an intensity larger than 5×rms, until the statistic reaches a convergence. In practice, we consider that the "confusion noise" is related only to the sources fainter than a signal-to-noise ratio q=S/N<5, where N is evaluated numerically by clipping the tail of the distribution as described above. The bottom panel of Fig. 3.5 reports from left to right the rms measured in the I, U, and Q images with respect to the FWHM. The blue solid line are the fit of the data whose equations are indicated in the right bottom corner. As reference we trace with a red line the confusion noise in total intensity expected on the basis of the simplified formula provided by Condon (2002):

$$\frac{\sigma_c}{mJy/beam} = 0.2\left(\frac{\nu}{GHz}\right)^{\alpha}\left(\frac{FWHM_{min}\times FWHM_{max}}{arcmin}\right)^2 \tag{3.4}$$

assuming $\alpha = 0.8$ and $\nu = 1.355\,\mathrm{GHz}$. We note that for what concerns the total intensity there is a remarkable agreement (to within 40%) between the predictions of our simulations and the formula by Condon (2002) widely used in literature. Indeed, we are confident of the reliability of our calculations and we can go further and try to infer the confusion limit in Stokes U and Q. We report in the following the best fit equations showed in the plots:

$$\sigma^I_{mJy/beam} = 0.096\cdot(FWHM_{arcmin})^{2.02} \tag{3.5}$$

$$\sigma^Q_{mJy/beam} = 0.003\cdot(FWHM_{arcmin})^{2} \tag{3.6}$$

$$\sigma^U_{mJy/beam} = 0.004\cdot(FWHM_{arcmin})^{2.17} \tag{3.7}$$

$$\tag{3.8}$$

As expected the confusion limits of the U and Q Stokes parameters are 30 times lower than in total intensity. This result is of paramount importance since it implies that we can perform much deeper observations in polarization than in total intensity provided that we have a high sensitivity instrument like the SKA.

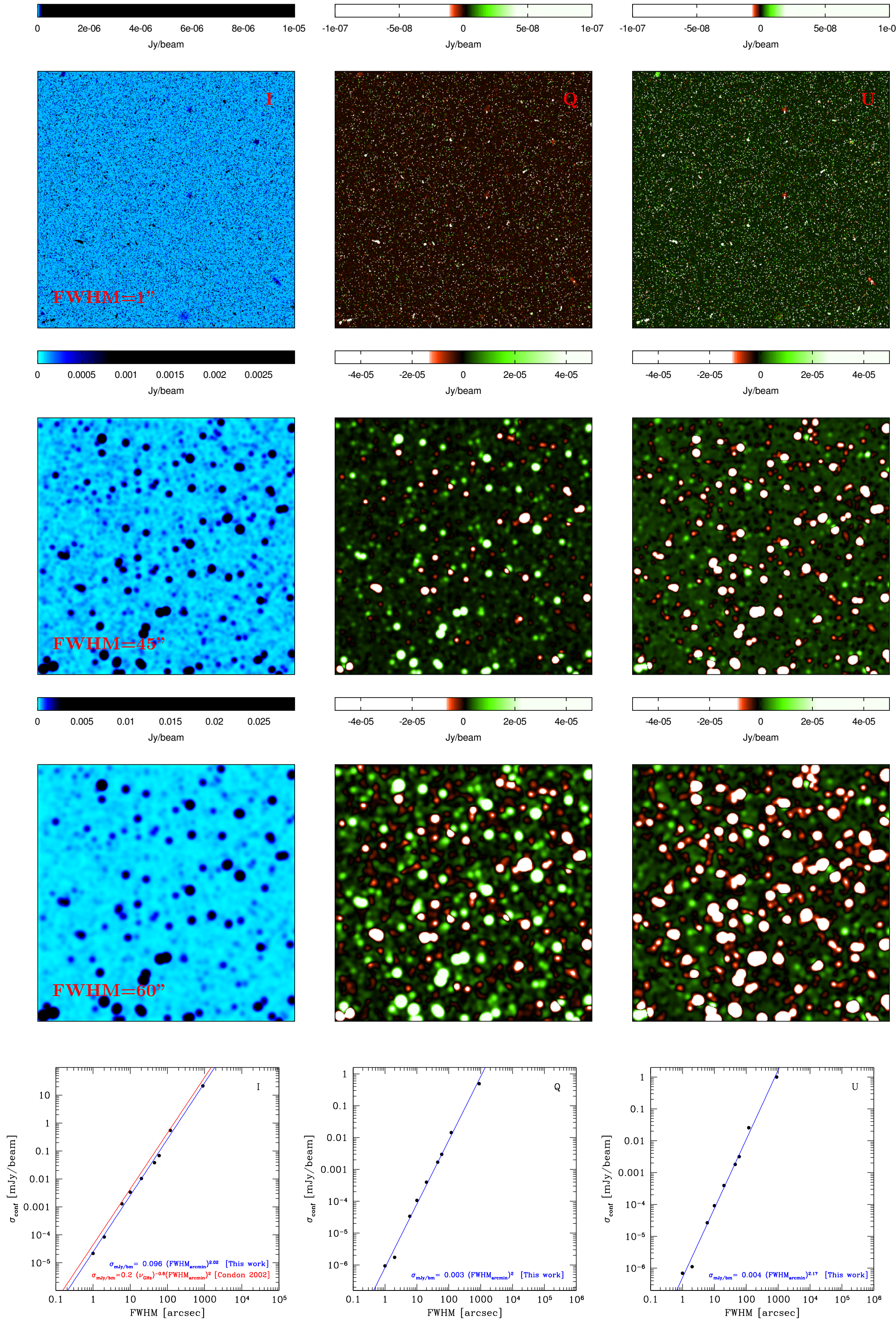

Figure 3.5 From left to right, simulated images of the I, U and Q Stokes parameters of radio galaxies in a field-of-view of $\sim 0.7\,\mathrm{deg}^2$. The images from top to bottom have been convolved with a FWHM=1″, 45″ and 60″ respectively. The bottom plots show the confusion noise of the I, U and Q Stokes parameters calculated from the convolved images with respect to the FWHM and the fit of the measured points in blue. The fitted relations are reported in the bottom left corner. For the confusion in total intensity we also show the formula proposed by Condon (2002).

4

Constraining magnetic fields in a simulated pair of merging galaxy clusters

Cosmic magnetism is one of the main science drivers of the SKA. So far, the determination of magnetic fields in galaxy clusters has been performed from the analysis a few radio sources per cluster. With the SKA, it will be possible to increase the number of radio sources up to hundreds of objects, covering the entire cluster volume. In addition, the SKA will be able to detect the polarization of radio haloes which has been proven to be extremely difficult with the current instruments. However, how accurate the SKA will be in reconstructing the RM images associated to the magneto-ionic medium of galaxy clusters? Answering to this question is not trivial since it requires the simulation and then the analysis of a huge amount of synthetic data, as it will be for the case of the real SKA observations. By using the numerical simulations described in the previous Chapter and state-of-the art cosmological magneto-hydro-dynamical simulations of the ICM properties we tried to address this challenging question.

In this Chapter, we show the simulated observations of a pair of two merging galaxy clusters as it would be observed by the SKA1-MID at $\sim 1.4\,\mathrm{GHz}$ with a resolution of $2.5''$. In addition to the discrete radio sources we also simulate two radio haloes. We apply the RM synthesis technique on the simulated data at $2.5''$ and also on the data convolved at a resolution of $10''$ to show the impact of beam depolarization.

4.1 Features of the simulation

A realistic simulation must include the following fundamental features:

i) a cosmological population of radio sources;

ii) a population of cluster-embedded radio sources;

iii) a cluster wide radio halo.

The polarization properties of all these sources are modified by the Faraday rotation effect as the radio waves cross the magneto-ionic intracluster medium. Indeed, it is fundamental to determine if and how we are able to reconstruct the input (the theoretical RM from mock data).
We decided to consider a pair of merging galaxy clusters whose ICM properties have been taken from a cosmological magneto-hydro-dynamical simulation. We use FARADAY to illuminate the magnetic fields of the clusters with relativistic particles and to include the discrete radio sources. The details of the simulations are explained in the following Sections. Here, we assume a ΛCDM cosmology with $\mathrm{H_0} = 73\,\mathrm{km \cdot s^{-1} Mpc^{-1}}$, $\Omega_\mathrm{m} = 0.27$, and $\Omega_\Lambda = 0.73$. At z=0.205, $1''$ corresponds to 3.24 kpc.

4.1.1 The cosmological magneto-hydro-dynamical simulation

Cosmological magneto-hydro-dynamical (MHD) simulations are powerful tools to investigate large scale magnetic fields and we can found many examples of such studies in literature (Bonafede et al. 2011; Brüggen et al. 2005; Dolag et al. 2002; Dubois & Teyssier 2008; Dubois et al. 2009; Donnert et al. 2009; Xu et al. 2009, 2010, 2011, 2012).
The cosmological MHD simulation presented here has been obtained with the ENZO code (Collins et al. 2010) with adaptive mesh refinement (AMR) by the group of Hui Li at the Los Alamos National Laboratories, USA. It is a small part of a bigger cosmological simulation realized in a volume of $(256 \cdot \mathrm{h^{-1}\,Mpc^{-3}})$ which encloses several forming structures. Indeed, the evolution of the dark matter, of the baryonic matter and of magnetic fields are produced during the simulation. An adiabatic equation of state with the ratio of specific heat $\Gamma = 5/3$ has been used, while heating and cooling physics or chemical reactions were not included. The simulation runs from redshift z=30 to z=0. We focus on a pair of galaxy clusters with similar masses that undergoes to a merging process that will result in a single system at z=0.073 with a total mass of $\mathrm{M} = 1.9 \times 10^{15} \mathrm{M_\odot}$. The collision lasts for about 2 Gyrs. The magnetic fields are injected by AGNs at z=2-3 and then are amplified and spread over Mpc-scales during the late stages of the merger.

For the purposes of this thesis work, we used a single snap-shot of the MHD simulation at z=0.205. At this particular instant the clusters are still separated by about 4.5 Mpc. The simulation consists in a set of 3-dimensional cubes of $\sim (6.4\,\mathrm{Mpc})^3$ with a cell size of $\sim 10.7\,\mathrm{kpc}$ containing the ICM physical parameters: the temperature, the thermic plasma density, and the intracluster magnetic fields. The physical configuration is very similar to that observed for the pair of galaxy clusters A399-A401 where both the systems host a diffuse radio halo (Murgia et al. 2010).

From the MHD simulation, we reproduced with the FARADAY tool the X-ray surface brightness between $0.1-2.4\,\mathrm{keV}$, which is shown in Fig. 4.1 (top left). The two clusters are found to be very bright in the X-ray band with surface brightness values of the order of $\sim 25 \times 10^{44}\,\mathrm{erg/s/Mpc^2}$ at their centres. In the same Figure (bottom left) we plot the density profiles of the two clusters which have been fitted with a $\beta-$model (blue dotted and red dashed lines for the galaxy cluster C1 and C2 respectively). The parameters of the $\beta-$model are reported in the bottom left corner.
We also performed the integral which defines the RM (see Eq. 1.29) obtaining the "theoretical" RM image shown in the top right of Fig. 4.1 together with the intracluster magnetic field profiles of the two galaxy clusters (bottom right). The RM image is indicative of the

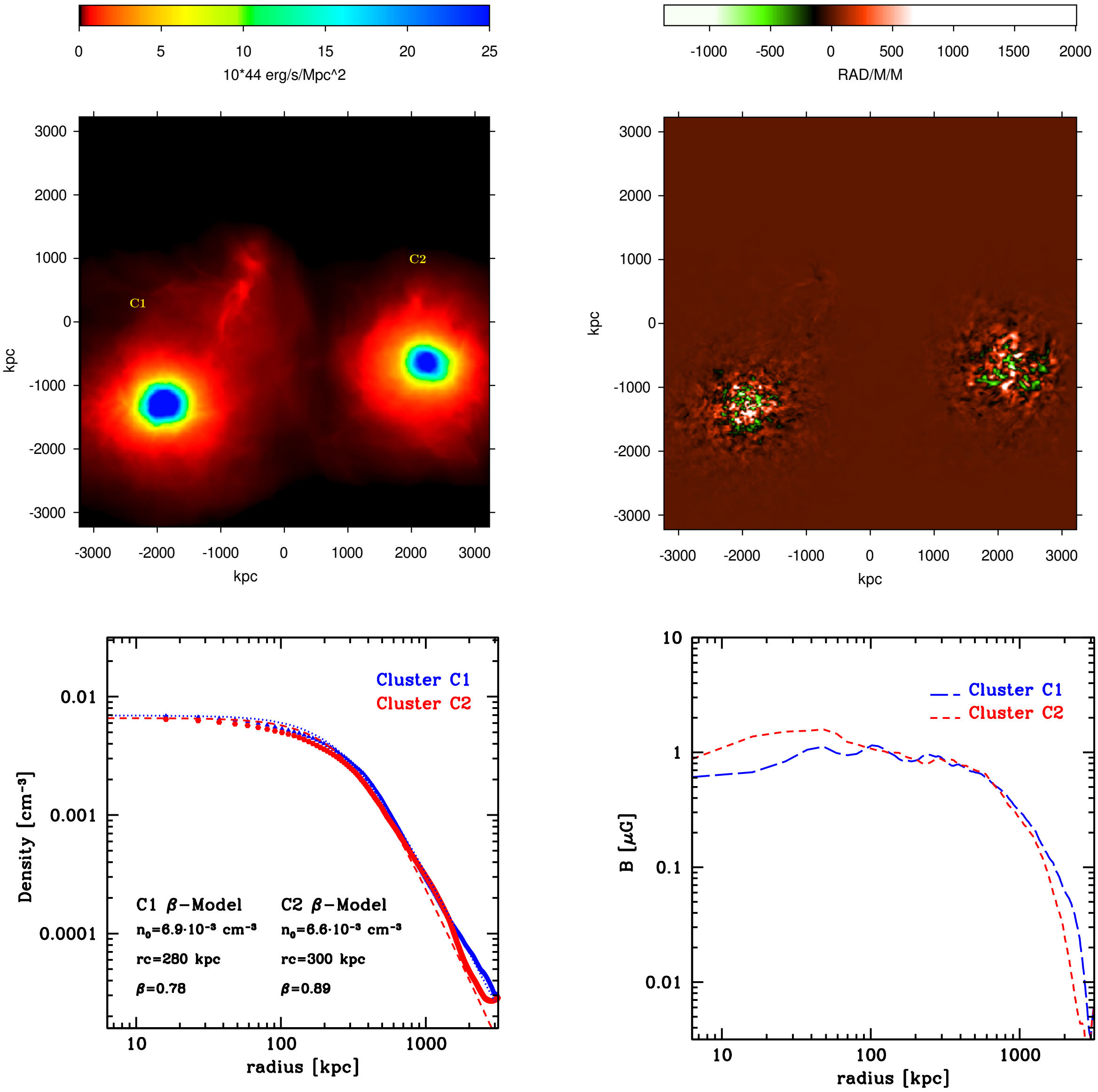

Figure 4.1 *Top left:* X-ray surface brightness of the two galaxy clusters between 0.1−2.4 keV. The field-of-view is ∼(6.4 Mpc)^2 and the resolution is ∼10.68 kpc. *Bottom left:* the density profiles of the two galaxy clusters fitted with a β model whose parameters are reported in the bottom left corner. *Top right:* the Rotation Measure image of the system. *Bottom right:* the intracluster magnetic field profiles of the two galaxy clusters. The ICM properties have been simulated with the ENZO software package while the X-ray surface brightness, the Rotation Measure images and the profiles have been reproduced with the FARADAY tool.

turbulent structure of the intracluster magnetic fields and it decreases going from the centre to the outskirts of the clusters, a behaviour which reflects the intracluster magnetic field profiles shown in the bottom plot.

4.1.2 The FARADAY simulation

Following Govoni et al. (2013), we adopt the intracluster magnetic field of the MHD simulation to create with FARADAY the radio haloes in equipartition condition (see Appendix B). In particular, we illuminate the magnetic fields with two relativistic particle populations with a power-law energy distribution with index p=3.6 and minimum and maximum Lorentz factors of $\gamma_{\rm min} = 300$ and $\gamma_{\rm max} = 1.5 \times 10^4$ while the normalization factor is defined so that the radio halo is in the minimum energy condition.

According to the MHD simulation, the redshift of the clusters' pair is z=0.205 while we set r_{200}=2.23 Mpc for both systems (r_{200} is the distance within which the cluster density is 200 times the critical density of the Universe). The cluster-embedded radio sources are simulated inside a volume of $\sim$(6.4 Mpc)^3. The external discrete radio sources are produced all over the slice of Universe identified by the field-of-view of the synthetic observation 6.4×6.4 Mpc^2. This corresponds in the adopted cosmology to $\sim 0.3\,\rm deg^2$. The simulated cosmological radio source population consists of 293841 radio sources. In output, we simulate the I, U, and Q Stokes parameters within cubes of 1024×1024×512 pixels where the first two axis correspond to the right ascension and declination while the third dimension is the frequency. The synthetic data are reproduced considering the band 2 of the SKA1-MID, having a starting frequency of 950 MHz and a bandwidth of 810 MHz. The frequency channels have a spectral resolution of ∼1.46 MHz. We assume SKA1-MID observations long enough that the I, U, and Q Stokes images are dominated by confusion noise ($\sigma_{\rm c}^{\rm I} = 0.15\,\mu$Jy/beam, $\sigma_{\rm c}^{\rm U} = 4\,$nJy/beam, and $\sigma_{\rm c}^{\rm Q} = 5\,$nJy/beam from our estimates presented in Sect. 3.4). Clearly, this is an ideal case since while in total intensity the SKA1-MID will reach this noise level after ∼25 hours of observations, in U and Q Stokes parameters it will need years of integration time (calculations based on the SKA1 System Baseline Design v2, see Dewdney et al. 2015). However, we decide to do not add the thermal noise in the images in order to understand if the RM Synthesis applied on the simulated data can give us precise estimates of the cluster RM.

We take into account only radio sources with a flux density greater than 1 nJy. With this cut 220524 sources are left and among them 2042 are foreground SFGs, 218426 background SFGs, none foreground AGNs and 56 background AGNs. Mapped on sky the images have a pixel resolution of 2.5″ and a field-of-view of $\sim 0.3\,\rm deg^2$. We produced separately the simulations related to the radio haloes, the background sources, the foreground sources, the cluster-embedded radio sources and then we put all of them together. Simulations have been performed using the Cybersar computer cluster hosted at the Cagliari Astronomical Observatory. They required a computational time of several months on 16 nodes having 8 cores each.

4.2 The simulation results

The resulting total intensity images are shown in Fig. 4.2: in the top images, from left to right, we can see the emission of the "cosmological" radio sources (background plus fore-

ground sources), of the radio haloes, and of the cluster-embedded radio sources, while in the bottom image we show the total intensity of the all components. The field-of-view is of $\sim 0.3\,\mathrm{deg}^2$ while the beam FWHM=2.5″.
The radio haloes present a notable filamentary structure with a decreasing surface brightness going from the centre to the outskirts. We can observe an enhancement of the surface brightness in a region north from the centre of cluster C1 which we can identify with a possible roundish relic. The image associated to the background plus the foreground sources appears bright and the sources cover uniformly the entire field-of-view. We can appreciate the wealth of details of these simulated images: from the fine structure of the discrete radio sources to the large scale filaments of the radio haloes.

Fig. 4.3 shows the linearly polarized emission (same order as in Fig. 4.2). The polarized sky appears bright and rich of discrete radio sources but also the radio haloes shine in polarization.

We note that at the sensitivity limit of these simulated images it would be hard in some cases to distinguish between fragments of the radio halo emission and nearby discrete radio sources.
The simulated radio haloes have characteristics similar to the radio haloes known in literature as shown by the radio halo power at 1.4 GHz versus the cluster X-ray luminosity in the 0.1-2.4 keV band (left) and versus the largest linear size of the radio halo measured at 1.4 GHz (right) in Fig. 4.4. Here, blue dots are the radio haloes taken from the compilation of Feretti et al. (2012) plus other measurements (Govoni et al. 2012; van Weeren et al. 2012; Giovannini et al. 2013; Martinez Aviles et al. 2016; Shakouri et al. 2016; Parekh et al. 2017; Loi et al. 2017b) while the two red triangles indicates the values associated to our simulated radio haloes.

4.3 RM Synthesis at 2.5″

As explained in Chapter 1, the RM synthesis technique (Burn 1966; Brentjens et al. 2005) aims to reconstruct, for each line-of-sight, the polarization with respect to the Faraday depth $\phi(l)$: starting from the spectra of U and Q Stokes parameters we assume different values for the Faraday depth inside a given interval and we rotate consequently the Stokes parameters. From the de-rotated U and Q we compute the corresponding polarization P to obtain the variation of the polarization inside the Faraday depth interval.
A background radio source or a cluster-embedded discrete radio source will appear as a single component in Faraday space and assuming as RM value the Faraday depth of the maximum polarized signal this technique is equivalent to the λ^2-fit of Eq. 1.28. For the radio halo emission the situation is different since the synchrotron and the thermal plasma are mixed. In this case, we expect multiple components in Faraday space along the same line-of-sight (see Fig. 1.9). In general, it is not obvious to associate directly one of these components to a specific physical depth. Thus, in the following, we assume for the RM the Faraday depth of the maximum peak.

We decided to apply the RM Synthesis technique to each component of the simulation and for simplicity we focus on a zoom centred on the galaxy clusters centres. The interval in Faraday depth explored in our analysis goes from -5000 $\mathrm{rad/m^2}$ to 5000 $\mathrm{rad/m^2}$ with a spacing of 10 $\mathrm{rad/m^2}$. The resulting transfer function has a full-width-at-half-maximum

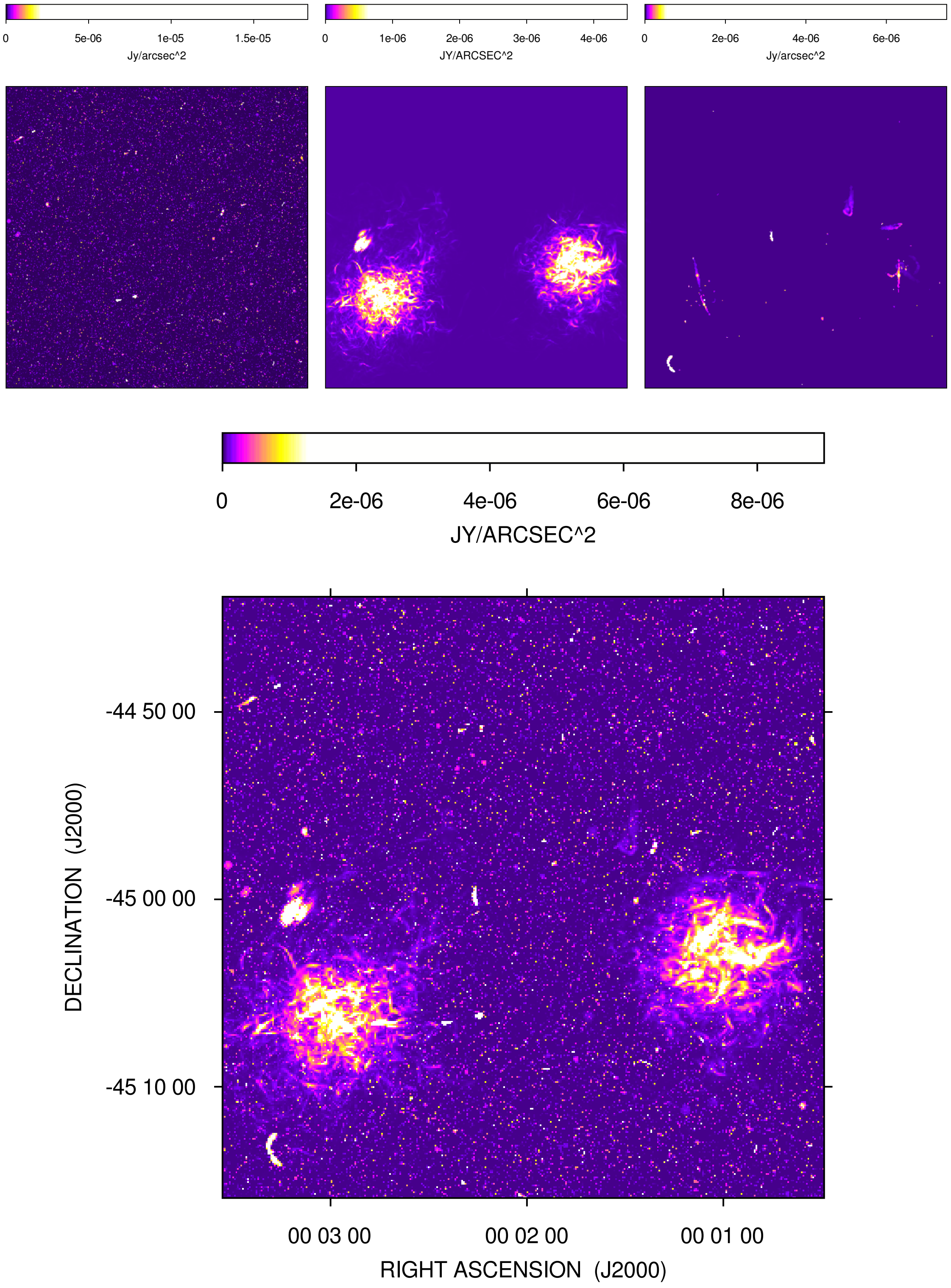

Figure 4.2 Total intensity simulated 1.4 GHz observation of a pair of galaxy cluster at z=0.205. The top images show, from left to right, the total intensity of the "cosmological" radio galaxies, of the radio halo, and the emission of the cluster-embedded radio galaxies, while in the bottom image we can see the total intensity of the all components. The field-of-view is equal to $\sim 0.3\,\mathrm{deg}^2$ with a pixel resolution of 2.5″. Images have been obtained by averaging all the spectral channels.

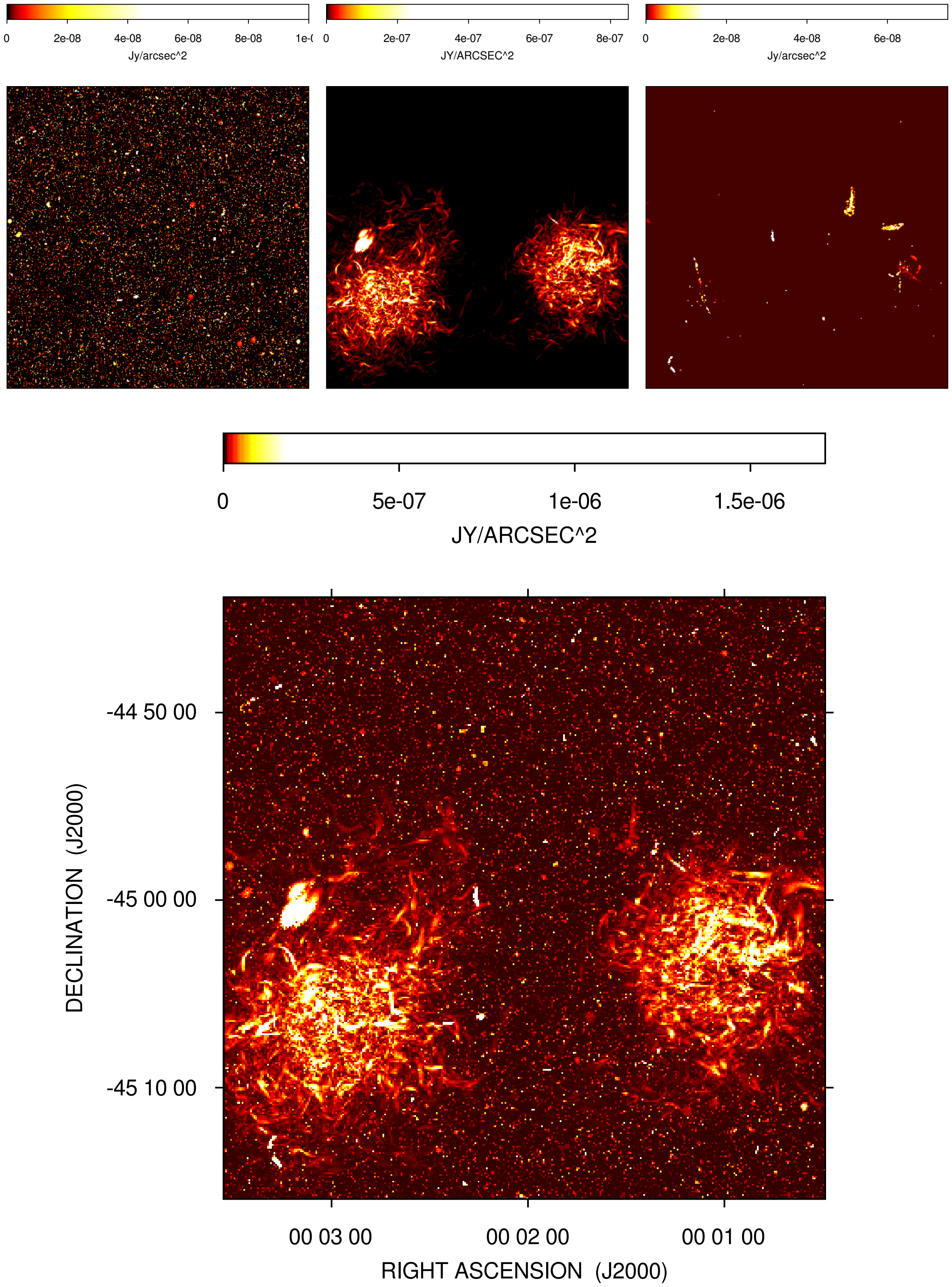

Figure 4.3 Polarized intensity simulated 1.4 GHz observation of a pair of galaxy clusters at z=0.205. The top images show, from left to right, the linearly-polarized intensity of the "cosmological" radio galaxies, of the radio halo, and the emission of the cluster-embedded radio galaxies, while in the bottom image we can see the linearly-polarized intensity of the all components. The field-of-view is equal to $\sim 0.3\,\mathrm{deg}^2$ with a pixel resolution of $2.5''$. Images have been obtained by averaging all the spectral channels (i.e. assuming RM=0).

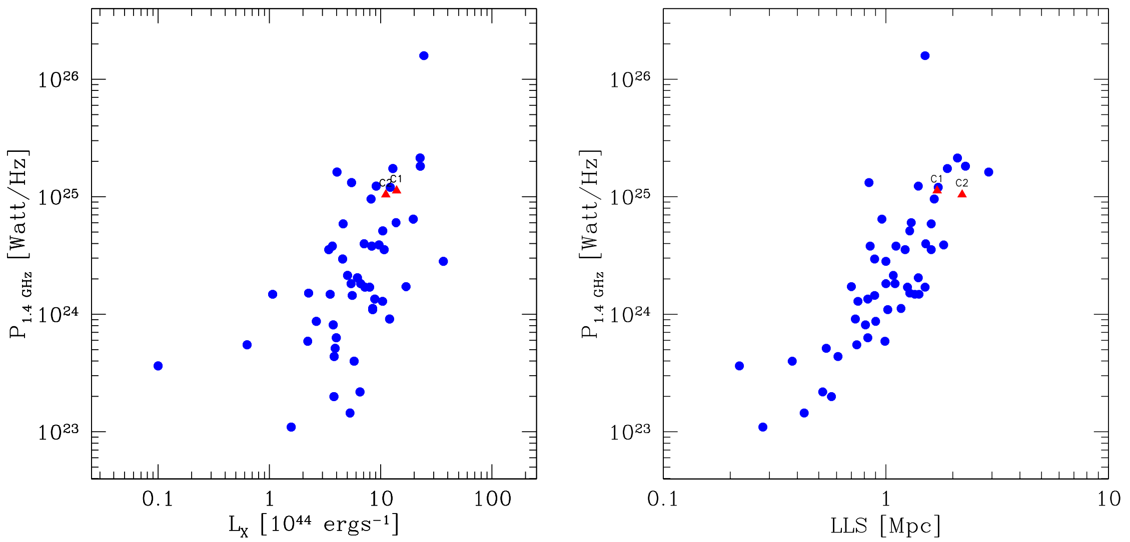

Figure 4.4 Radio halo power at 1.4 GHz versus the cluster X-ray luminosity in the 0.1-2.4 keV band (left) and versus the largest linear size of the radio halo measured at 1.4 GHz (right) of known radio haloes (blue dots) and of our simulated radio haloes (red triangles). See text for references.

(FWHM) of 40 rad/m^2. To perform the RM Synthesis we used a work station with 40 cores. The production of the RM Synthesis cubes of U and Q lasts for 12 hours for each data set.

The results are presented from Fig. 4.5 to Fig. 4.12: the top right images indicate the RM values corresponding to the polarization peak in the Faraday synthesis space, we blanked all the pixels where the polarized signal is zero due to the lack of sources; the top left images show the theoretical RM computed from the MHD simulated data following Eq. 1.29 and blanked as the corresponding RM Synthesis images. We also plot the radial profile (middle left) of the σ_{RM} of the theoretical RM images computed in annuli of ~ 40 kpc of width from the cluster centres (black line) in order to compare it with those computed from the RM Synthesis images (coloured dots). The radial profile of σ_{RM} is one of the most fundamental diagnostic to estimate the strength and the radial decline of the intracluster magnetic field (see Appendix C). The middle right panels compare point-to-point the values of RM Synthesis obtained for several lines-of-sight versus the corresponding theoretical values of RM and show the relative histograms. The values of this last plots have been calculated for all pixels in an annulus centred at 225 kpc from the cluster centres and having a width of 50 kpc. Finally, in the bottom panel we plot the RM structure function defined as:

$$S(dr) = \langle [RM(r) - RM(r + dr)]^2 \rangle, \tag{4.1}$$

where r is the distance in kpc and S(dr) is in rad^2/m^4. We calculate the function for the theoretical RM image (solid line), for the theoretical image blanked as the RM Synthesis image (dotted line) and for the RM synthesis image (coloured dots). The structure function is the other fundamental diagnostic to estimate the structure of the intracluster magnetic fields. This important observable allows us to estimate the magnetic field auto-correlation length Λ_{c}. This parameter is essential to measure the strength of the field since it enters directly in the Felten formula (see Appendix C).

Fig.s 4.5, 4.6, 4.7 and 4.8 shows the results for the cluster-embedded discrete radio sources, the background radio sources, the radio halo, and the radio halo plus the cluster-embedded, background and foreground radio sources respectively for the galaxy cluster C1.

In the same order, Fig. 4.9, 4.10, 4.11 and 4.12 show the results concerning the galaxy cluster C2.

From the above images and plots several consideration can be drawn:

(i) the cluster-embedded discrete radio sources do not accurately reproduce for each line-of-sight the theoretical values of RM as they are placed at different depths and thus they cross different portion of the magneto-ionic plasma of the clusters. For instance, according to the Felten formula (see Appendix C), if the cluster-embedded radio sources are located at half-way the cluster their $\sigma_{\rm RM}$ would be reduced by $\sqrt{2}$; we also notice that the structure function which can be inferred from the blanked theoretical RM presents higher values with respect to the full theoretical RM image. This may be due to the fact that in the case of the blanked RM image the structure function is calculated in regions with high values of RMs which give us high values of S(dr). However, the $\sqrt{2}$-suppression due to the Felten formula with respect to the S(dr) computed from the theoretical RM blanked image can be noticed from the comparison between the dotted lines and the coloured points;

(ii) the density of background radio sources is enough to cover the entire cluster area for both the clusters; indeed, the image, the $\sigma_{\rm RM}$ profile and the S(dr) computed from the RM synthesis well reproduce the theoretical values;

(iii) the RM synthesis images of radio haloes present micro-structures with respect to the theoretical images; this may be due to the fact that the RM synthesis gives us the RM of the polarized peak of the radio halo filaments and their position along the line-of-sight could be different for close lines of sight which share the same theoretical RM value. The $\sigma_{\rm RM}$ profiles as well as the structure function present slightly higher values at less than 500 kpc from the cluster centres. Moreover, the RM Synthesis versus the RM theoretical plots let us appreciate a peculiar behaviour. The trend of the correlation becomes super-linear with respect to the 1:1 correlation (black line). This could be related to the fact that the polarized peak of radio haloes is generated where the component of the intracluster magnetic field perpendicular to the line-of-sight presents high values in strength. It is possible that this signal will then cross a cell where also the parallel component of the magnetic field is strong and so it gives rise to a high RM values along that line-of-sight. Therefore, the RM values inferred from the RM Synthesis applied to radio haloes would give us higher values of RM. This picture may explain why, instead of observing the $\sqrt{2}$-suppression as for the case of cluster-embedded discrete radio sources, the RM and the $\sigma_{\rm RM}$ present higher values with respect to the theoretical ones. Whatever is the origin of the super-linear relation, the histograms show similar values of $\sigma_{\rm RM}$ even if their distribution is evidently different: for the theoretical RM histogram we observe a Gaussian distribution while the histogram of the RM Synthesis seems the sum of two different Gaussians;

(iv) for what concerns the case of radio haloes plus the discrete radio sources we observe a similar behaviour as for the case of radio haloes; this is due to the fact that the radio halo emission dominates the number of line-of-sights over the fainter discrete radio sources.

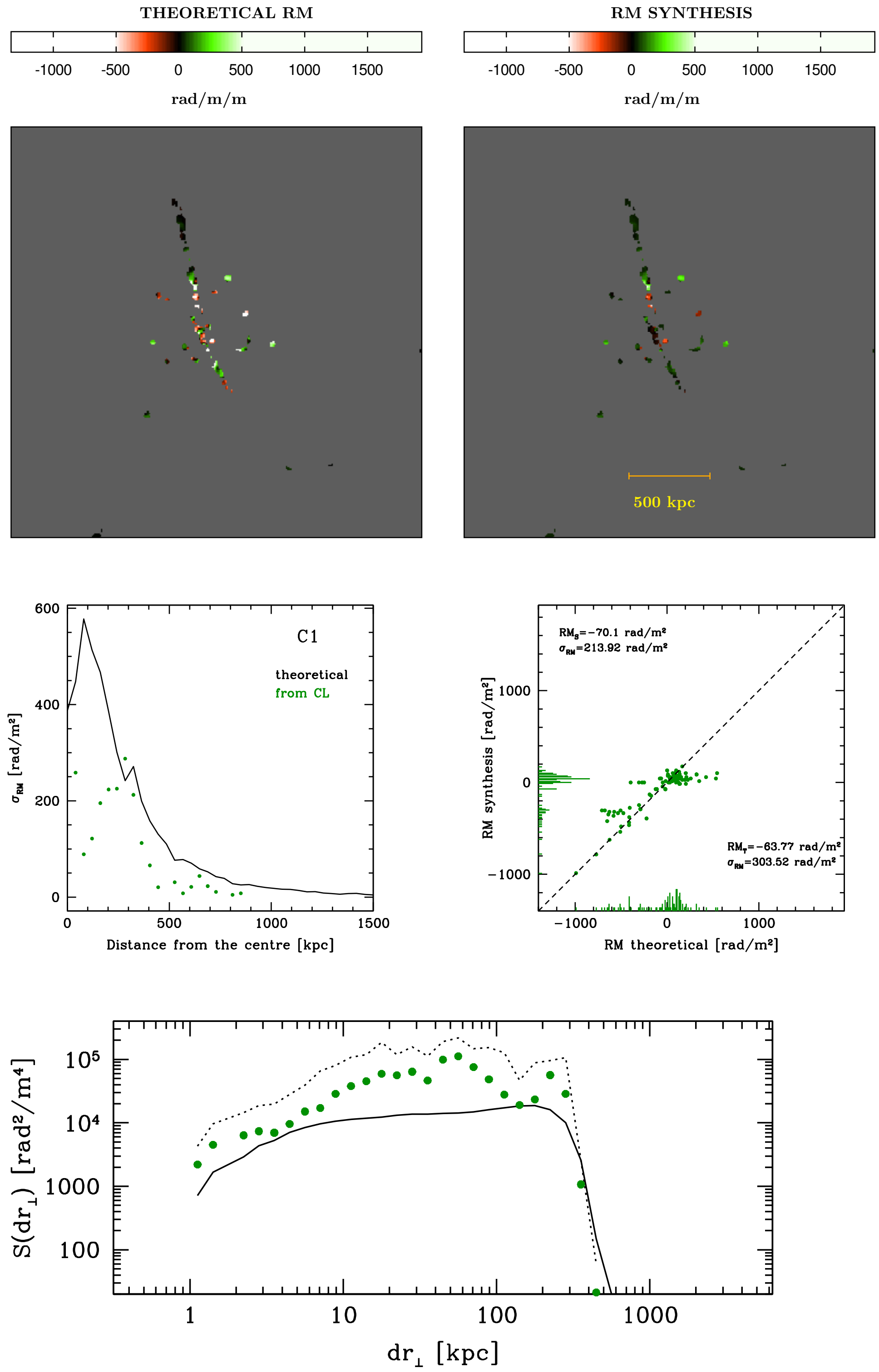

Figure 4.5 Results of the RM Synthesis technique on the *C1 cluster-embedded radio sources* (right) compared to the theoretical RM image (left) blanked as the right image. The middle left panel shows the radial profile of $\sigma_{\rm RM}$ computed from the theoretical RM image (black line) and from the RM synthesis image (green dots). The middle right panel compares the values of RM Synthesis obtained for each line of sigh versus the corresponding theoretical values of RM and the relative histograms calculated for all the pixels in an annulus centred at 225 kpc from the cluster centres and having a width of 50 kpc. The bottom panel shows the structure function computed for the full theoretical RM image (solid line), from the blanked theoretical RM image (dotted line), and from the RM Synthesis image (green dots).

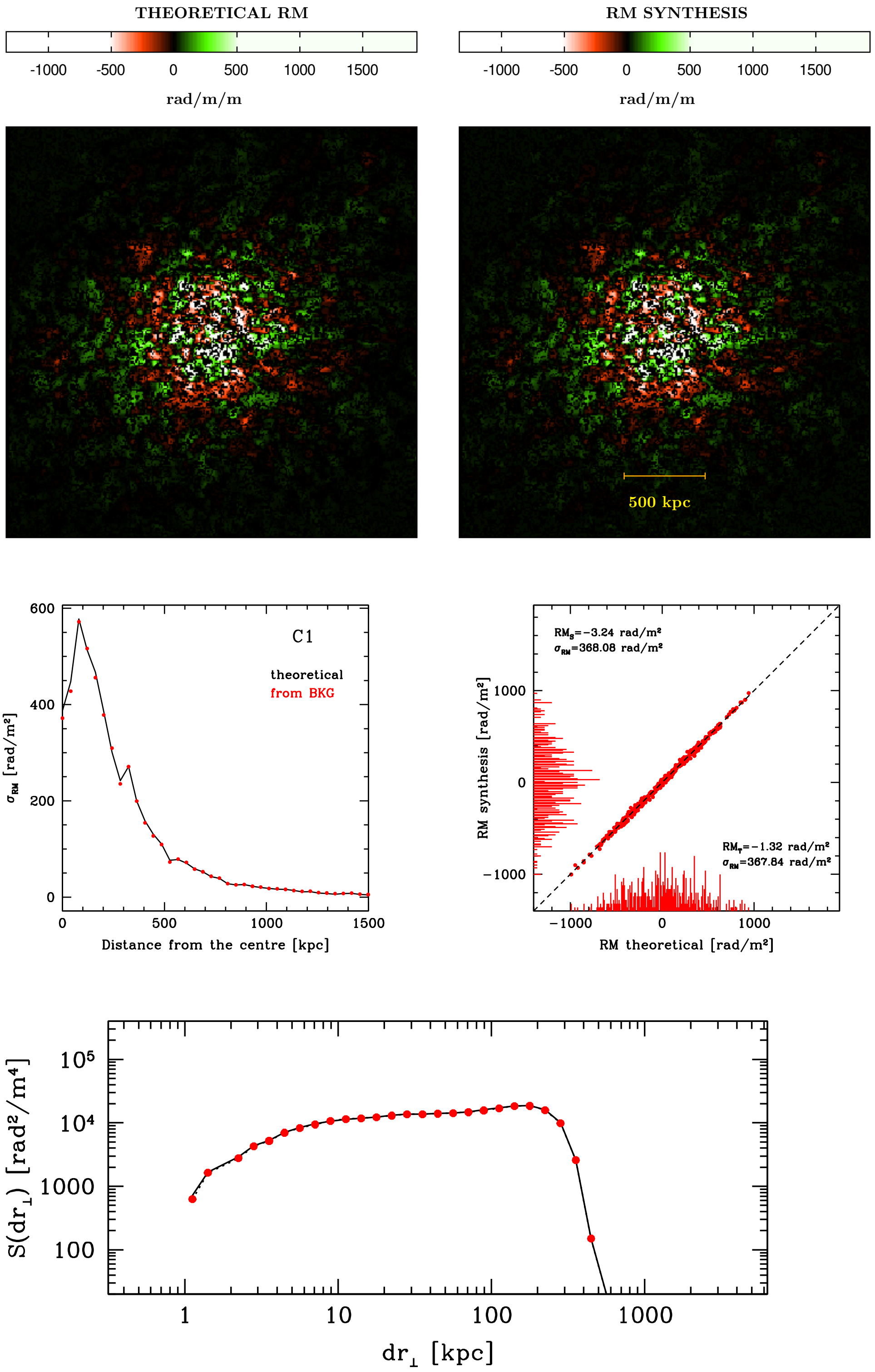

Figure 4.6 Results of the RM Synthesis technique on the *background radio sources of cluster C1* (right) compared to the theoretical RM image (left) blanked as the right image. The middle left panel shows to the radial profile of $\sigma_{\rm RM}$ computed from the theoretical RM image (black line) and from the RM synthesis image (red dots). The middle right panel compares the values of RM Synthesis obtained for each line of sigh versus the corresponding theoretical values of RM and the relative histograms calculated for all the pixels in an annulus centred at 225 kpc from the cluster centres and having a width of 50 kpc. The bottom panel shows the structure function computed for the full theoretical RM image (solid line), from the blanked theoretical RM image (dotted line), and from the RM Synthesis image (red dots).

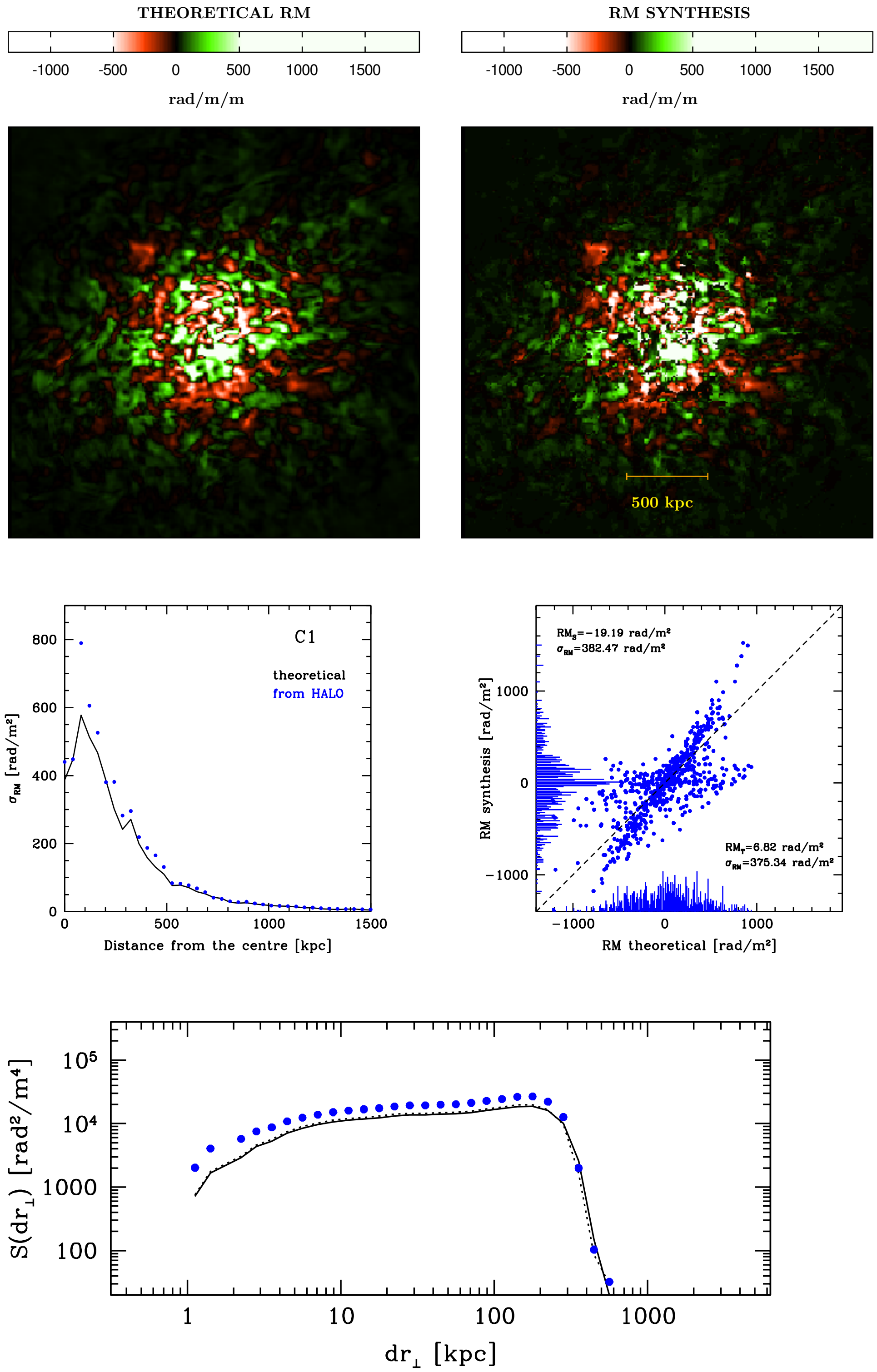

Figure 4.7 Results of the RM Synthesis technique on the radio halo of cluster C1 (right) compared to the theoretical RM image (left) blanked as the right image. The middle left panel shows the radial profile of $\sigma_{\rm RM}$ computed from the theoretical RM image (black line) and from the RM synthesis image (blue dots). The middle right panel compares the values of RM Synthesis obtained for each line of sigh versus the corresponding theoretical values of RM and the relative histograms calculated for all the pixels in an annulus centred at 225 kpc from the cluster centres and having a width of 50 kpc. The bottom panel shows the structure function computed for the full theoretical RM image (solid line), from the blanked theoretical RM image (dotted line), and from the RM Synthesis image (blue dots).

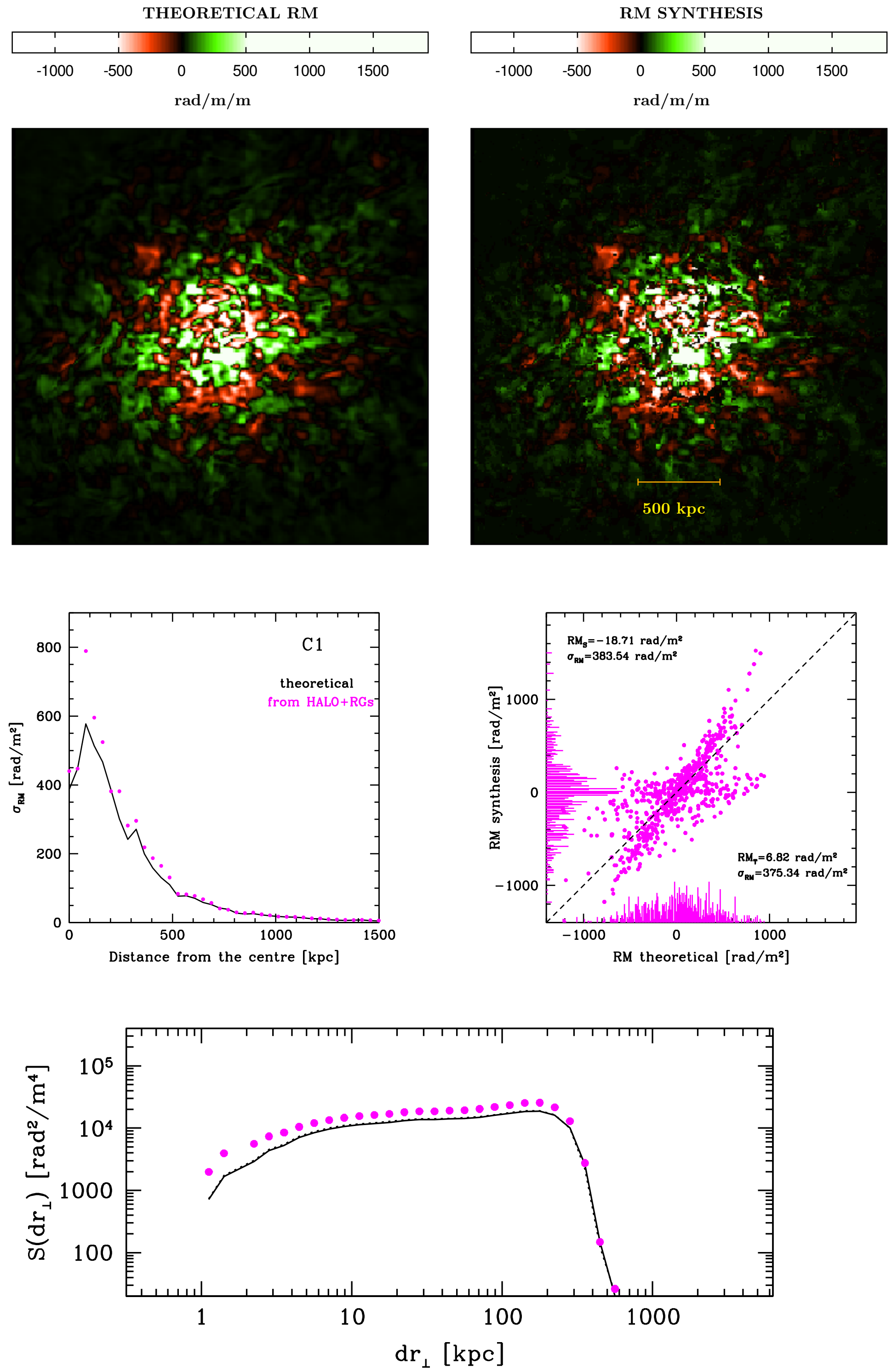

Figure 4.8 Results of the RM Synthesis technique on the *radio halo plus the cluster, background and foreground radio sources of cluster C1* (right) compared to the theoretical RM image (left) blanked as the right image. The middle left panel shows the radial profile of $\sigma_{\rm RM}$ computed from the theoretical RM image (black line) and from the RM synthesis image (magenta dots). The middle right panel compares the values of RM Synthesis obtained for each line of sigh versus the corresponding theoretical values of RM and the relative histograms calculated for all the pixels in an annulus centred at 225 kpc from the cluster centres and having a width of 50 kpc. The bottom panel shows the structure function computed for the full theoretical RM image (solid line), from the blanked theoretical RM image (dotted line), and from the RM Synthesis image (magenta dots).

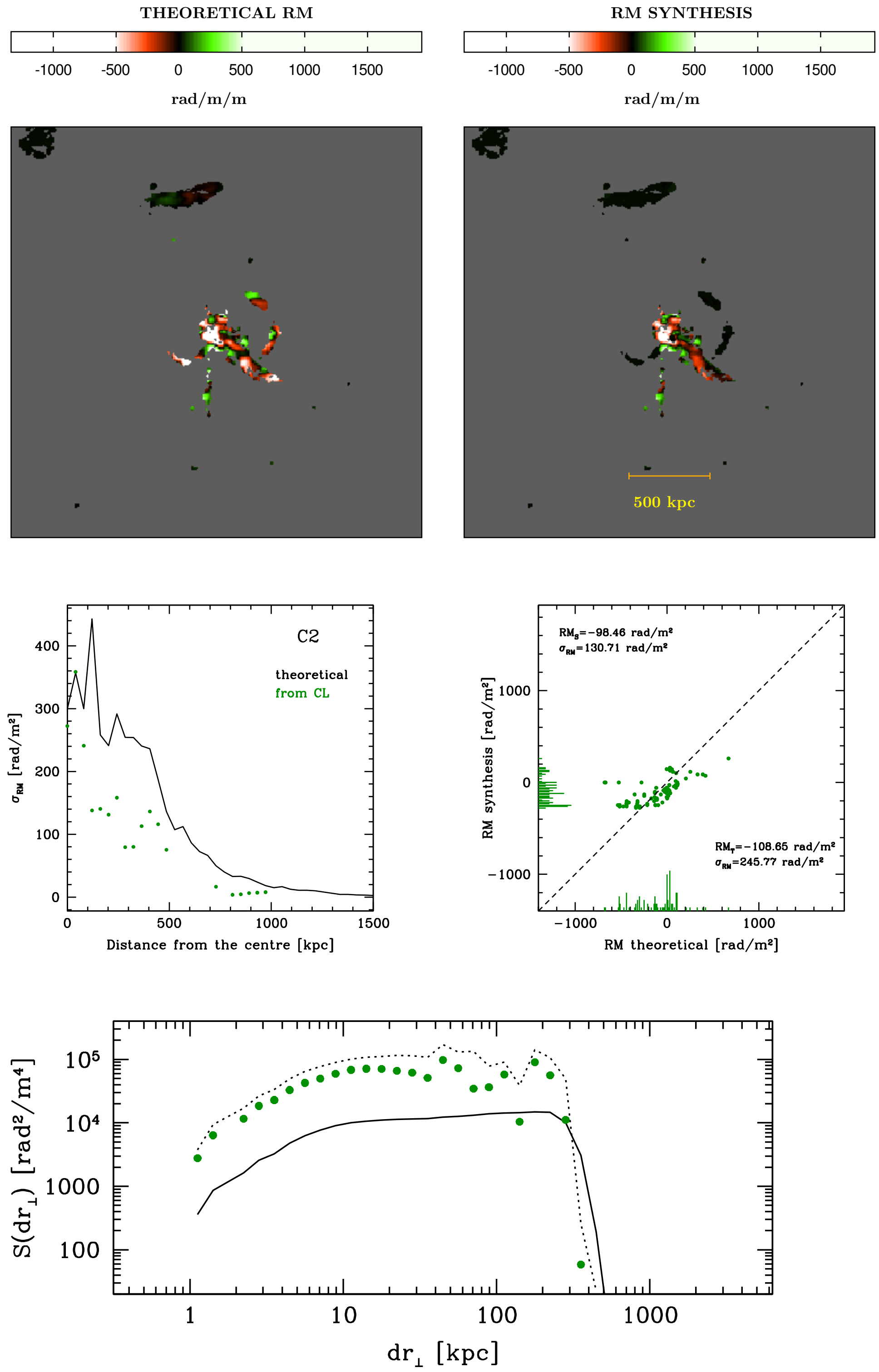

Figure 4.9 Results of the RM Synthesis technique on the *C2 cluster-embedded radio sources* (right) compared to the theoretical RM image (left) blanked as the right image. The middle left panel shows to the radial profile of $\sigma_{\rm RM}$ computed from the theoretical RM image (black line) and from the RM synthesis image (green dots). The middle right panel compares the values of RM Synthesis obtained for each line of sigh versus the corresponding theoretical values of RM and the relative histograms calculated for all the pixels in an annulus centred at 225 kpc from the cluster centres and having a width of 50 kpc. The bottom panel shows the structure function computed for the full theoretical RM image (solid line), from the blanked theoretical RM image (dotted line), and from the RM Synthesis image (green dots).

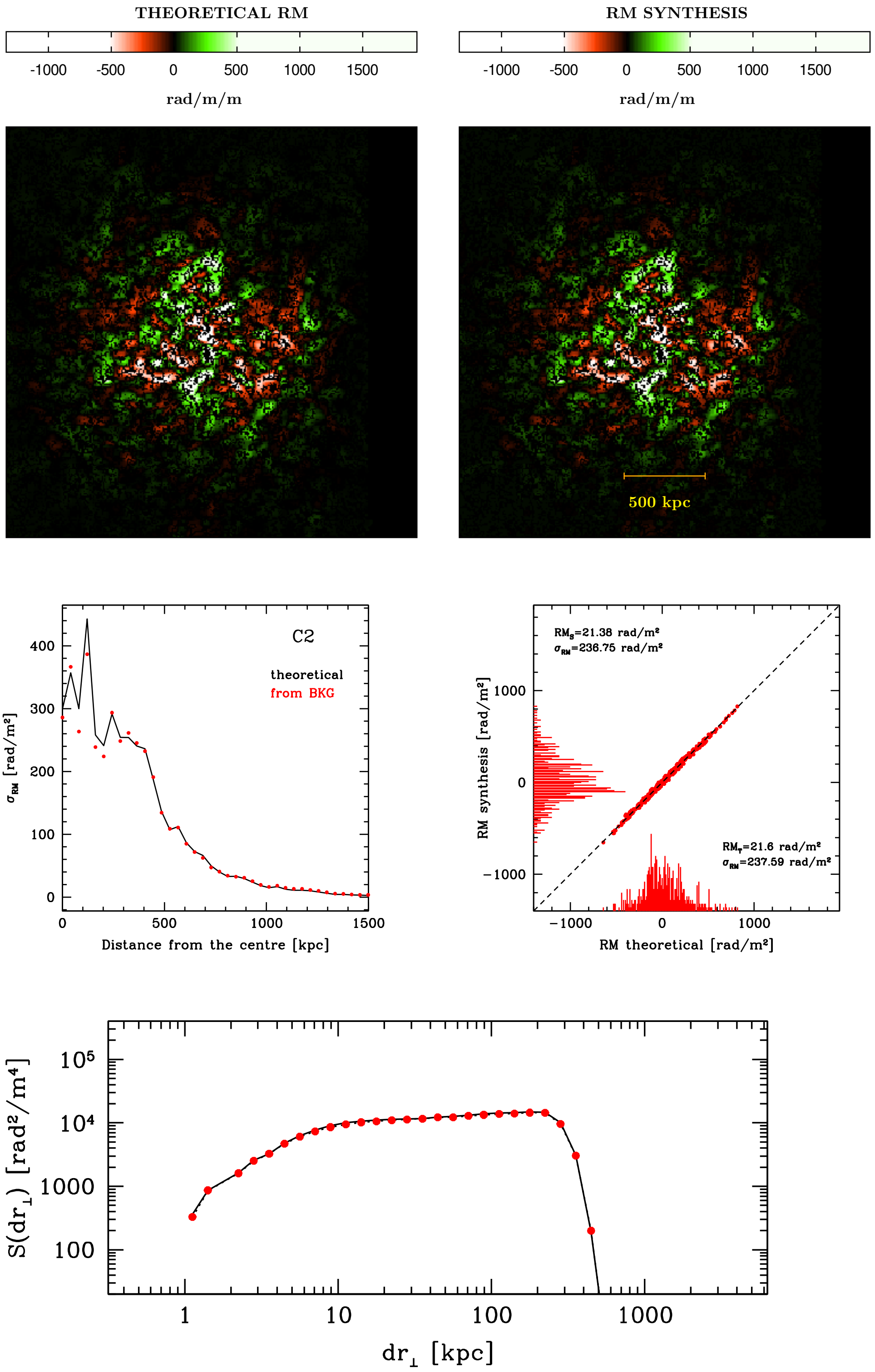

Figure 4.10 Results of the RM Synthesis technique on the *background radio sources of cluster C2* (right) compared to the theoretical RM image (left) blanked as the right image. The middle left panel shows the radial profile of $\sigma_{\rm RM}$ computed from the theoretical RM image (black line) and from the RM synthesis image (red dots). The middle right panel compares the values of RM Synthesis obtained for each line of sigh versus the corresponding theoretical values of RM and the relative histograms calculated for all the pixels in an annulus centred at 225 kpc from the cluster centres and having a width of 50 kpc. The bottom panel shows the structure function computed for the full theoretical RM image (solid line), from the blanked theoretical RM image (dotted line), and from the RM Synthesis image (red dots).

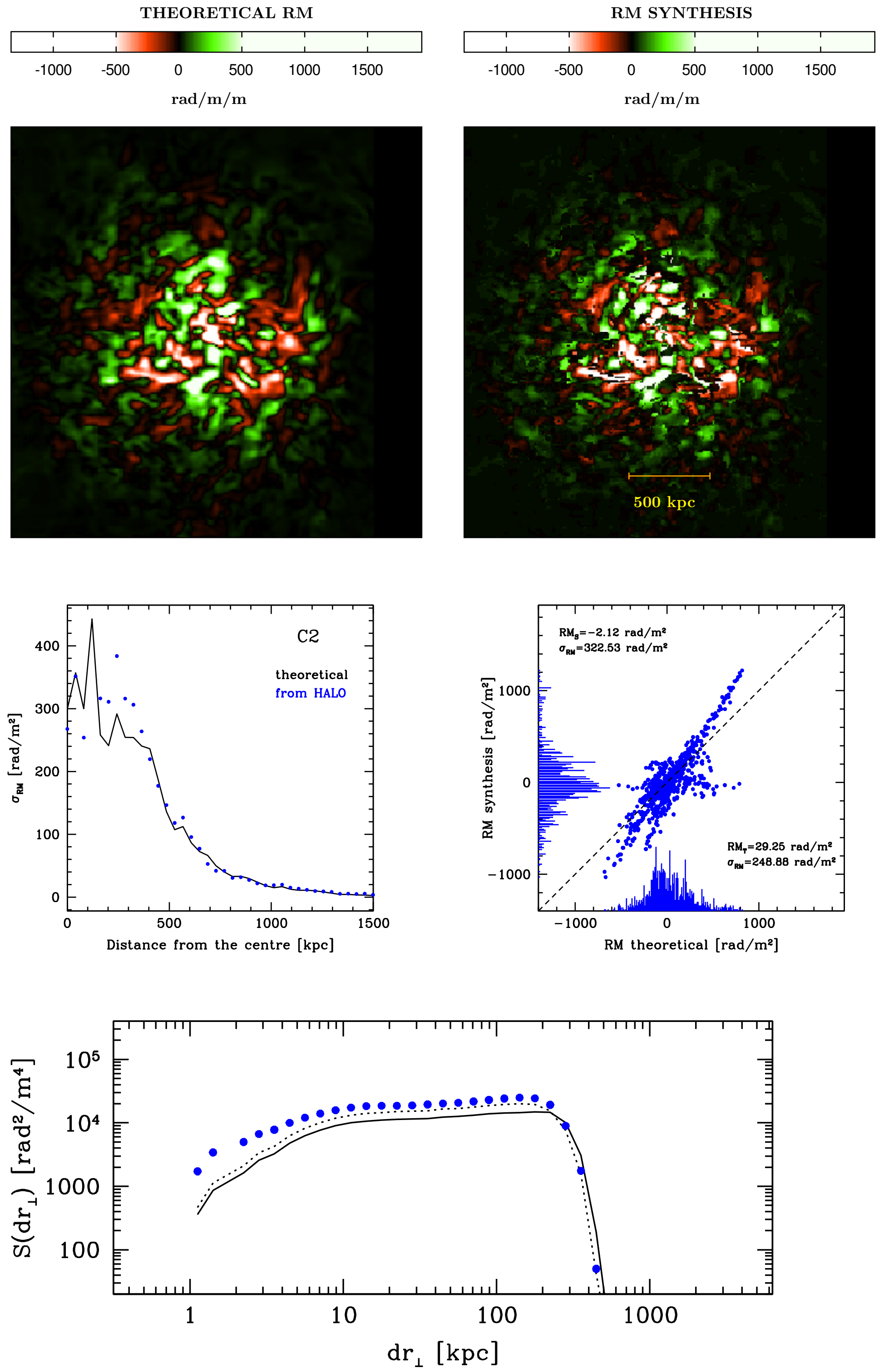

Figure 4.11 Results of the RM Synthesis technique on the *radio halo of cluster C2* (right) compared to the theoretical RM image (left) blanked as the right image. The middle left panel shows the radial profile of $\sigma_{\rm RM}$ computed from the theoretical RM image (black line) and from the RM synthesis image (blue dots). The middle right panel compares the values of RM Synthesis obtained for each line of sigh versus the corresponding theoretical values of RM and the relative histograms calculated for all the pixels in an annulus centred at 225 kpc from the cluster centres and having a width of 50 kpc. The bottom panel shows the structure function computed for the full theoretical RM image (solid line), from the blanked theoretical RM image (dotted line), and from the RM Synthesis image (blue dots).

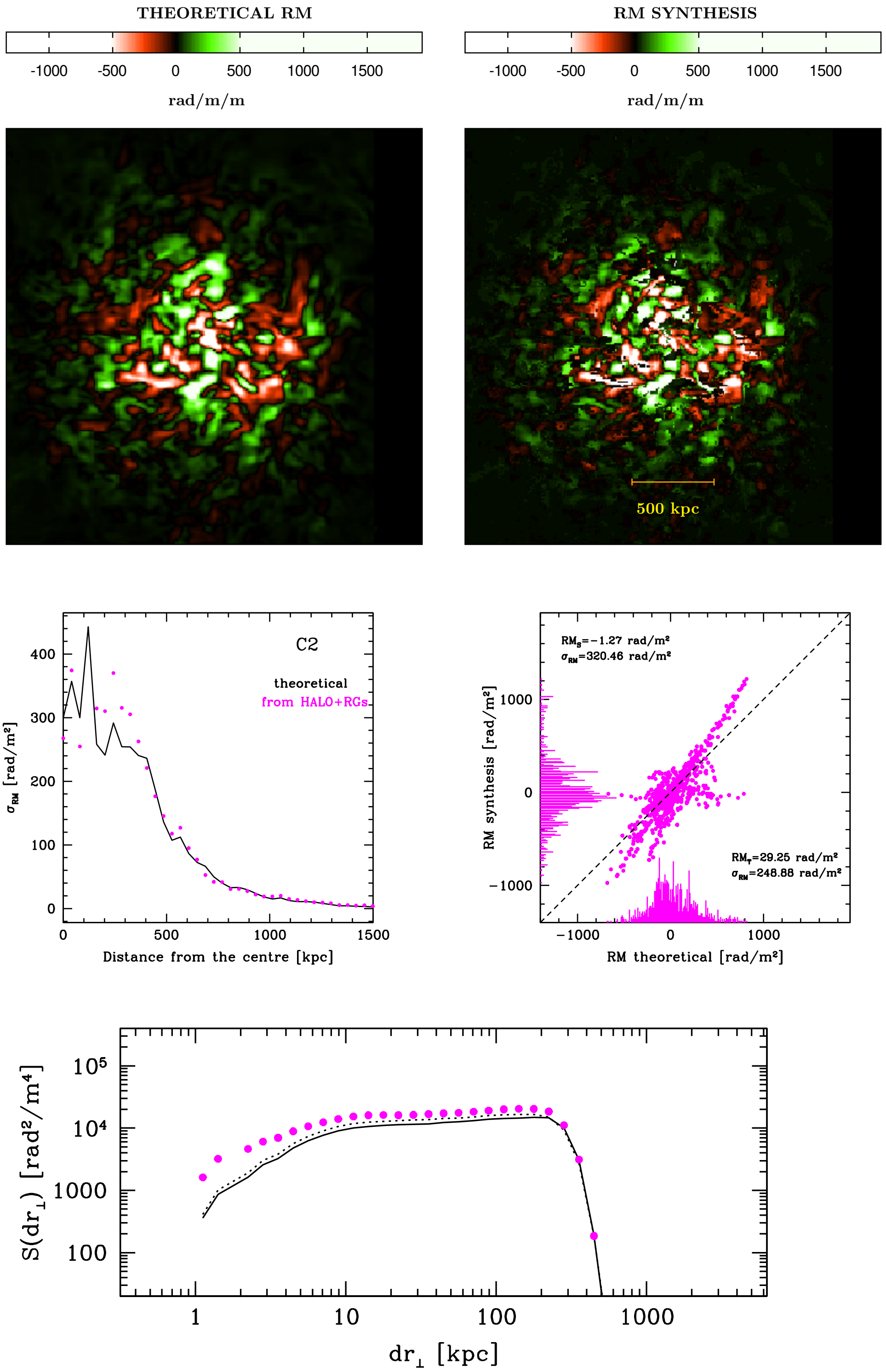

Figure 4.12 Results of the RM Synthesis technique on the *radio halo plus the cluster, background and foreground radio sources of cluster C2* (right) compared to the theoretical RM image (left) blanked as the right image. The middle left panel shows the radial profile of σ_{RM} computed from the theoretical RM image (black line) and from the RM synthesis image (magenta dots). The middle right panel compares the values of RM Synthesis obtained for each line of sigh versus the corresponding theoretical values of RM and the relative histograms calculated for all the pixels in an annulus centred at 225 kpc from the cluster centres and having a width of 50 kpc. The bottom panel shows the structure function computed for the full theoretical RM image (solid line), from the blanked theoretical RM image (dotted line), and from the RM Synthesis image (magenta dots).

As a general result, we can confirm that the Band 2 foreseen for the SKA1-MID is potentially very well suited for this kind of studies. For clusters without a radio halo, the population of background radio sources composing the RM grid will permit a very precise reconstruction of the cluster magnetic fields. Moreover, we notice that radio haloes are conceivably useful in the determination of the RM of galaxy clusters through the RM Synthesis technique. Nevertheless, this represent an ideal case since the observed time necessary to reach the confusion levels in U and Q predicted by our model (see Sect. 3.4) is too long (of the order of years).

4.4 RM Synthesis at 10″

In the previous Section we show that the application of the RM Synthesis on the U, Q data acquired over the Band 2 of SKA1-MID is potentially able to reconstruct the theoretical RM values and thus to constrain the intracluster magnetic fields.
Here, we consider the same images of the previous Section but convolved with a beam FWHM of 10″. This is a resolution provided by future surveys performed with SKA precursors and pathfinders like e.g. ASKAP (Norris et al. 2011). We applied the RM Synthesis technique on the convolved data obtaining the results shown from Fig. 4.13 to 4.20.

For what concerns the results on cluster-embedded sources we can observe the same behaviour as before.
On the other hand, background sources seem to suffer from beam depolarization as we can see from the comparison between the theoretical and the RM synthesis images point-to-point values, although the $\sigma_{\rm RM}$ profiles and the structure functions are more stable indicators.
Radio haloes show a different behaviour with respect to the results regarding the higher resolution images. Indeed, here we can observe the lack of micro-structure in the RM images and lower values in the $\sigma_{\rm RM}$ profiles and in the structure functions. We can suppose that beam depolarization suppresses the enhancement we observed at higher resolution.
Same consideration can be made for the case of radio haloes plus radio galaxies.

To summarize, we can state that even at 10″ of resolution with the band 2 of the SKA1-MID we can obtain reliable estimates of the RM of galaxy clusters if the exposure time is such that we reach the confusion level on data. Based on Dewdney et al. (2015), in order to reach the confusion levels of $\sigma_{\rm c}^{\rm I} = 2.6\,\mu{\rm Jy}$, $\sigma_{\rm c}^{\rm Q} = 83\,{\rm nJy}$, and $\sigma_{\rm c}^{\rm I} = 81\,{\rm nJy}$ at 10″ of resolution the integration time should be ~6 minutes and ~90 hours in U and Q Stokes parameters. The number of background radio sources forming the RM grid is enough to permit us a precise reconstruction of the RM properties in the majority of galaxy clusters. The presence of radio haloes could significantly help in determine the RM values although the interpretation of the RM Synthesis results is not trivial, as discussed before.

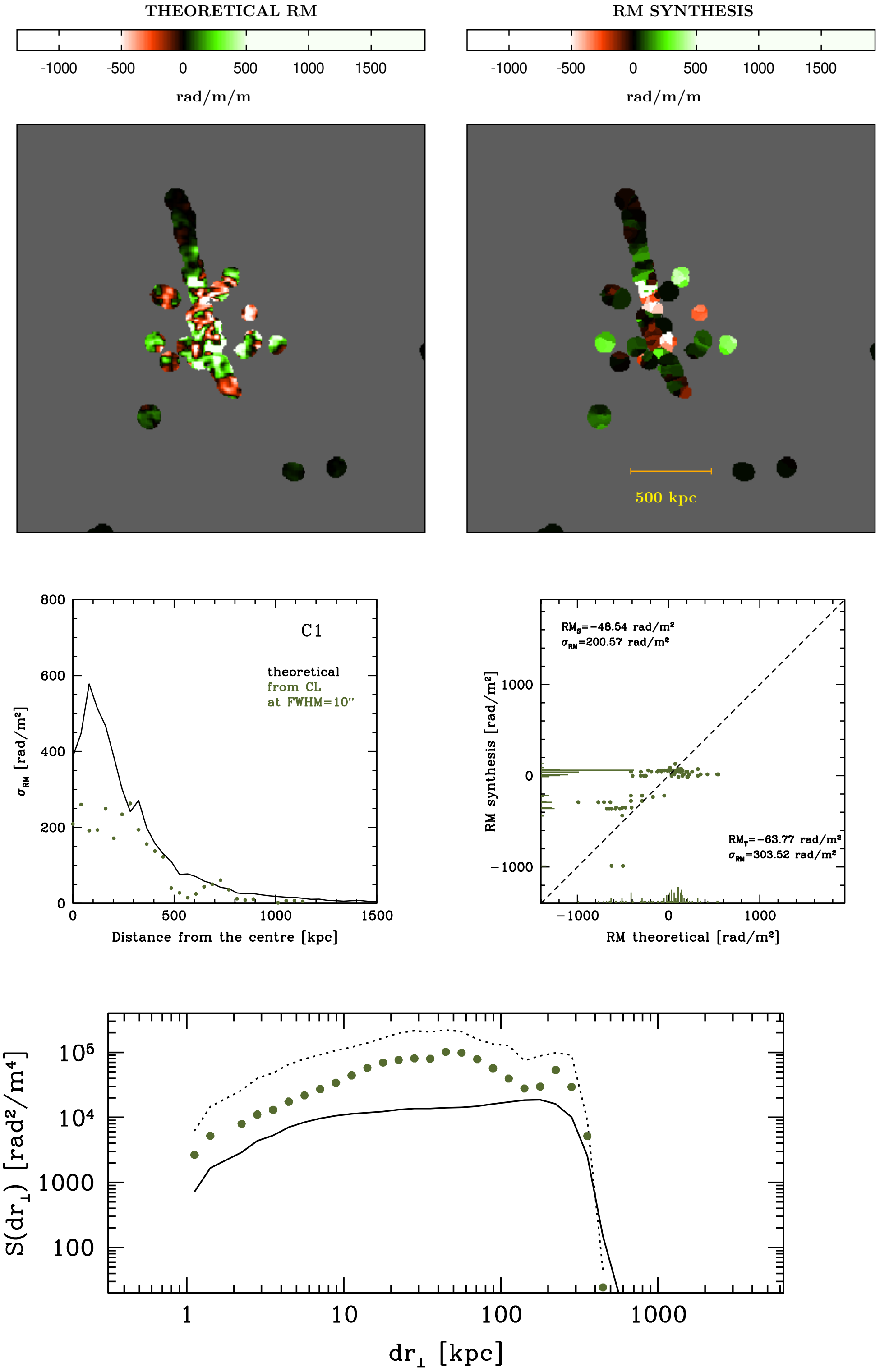

Figure 4.13 Results of the RM Synthesis technique on the *C1 cluster-embedded radio sources at FWHM=10″*. See Fig. 4.5 for the details.

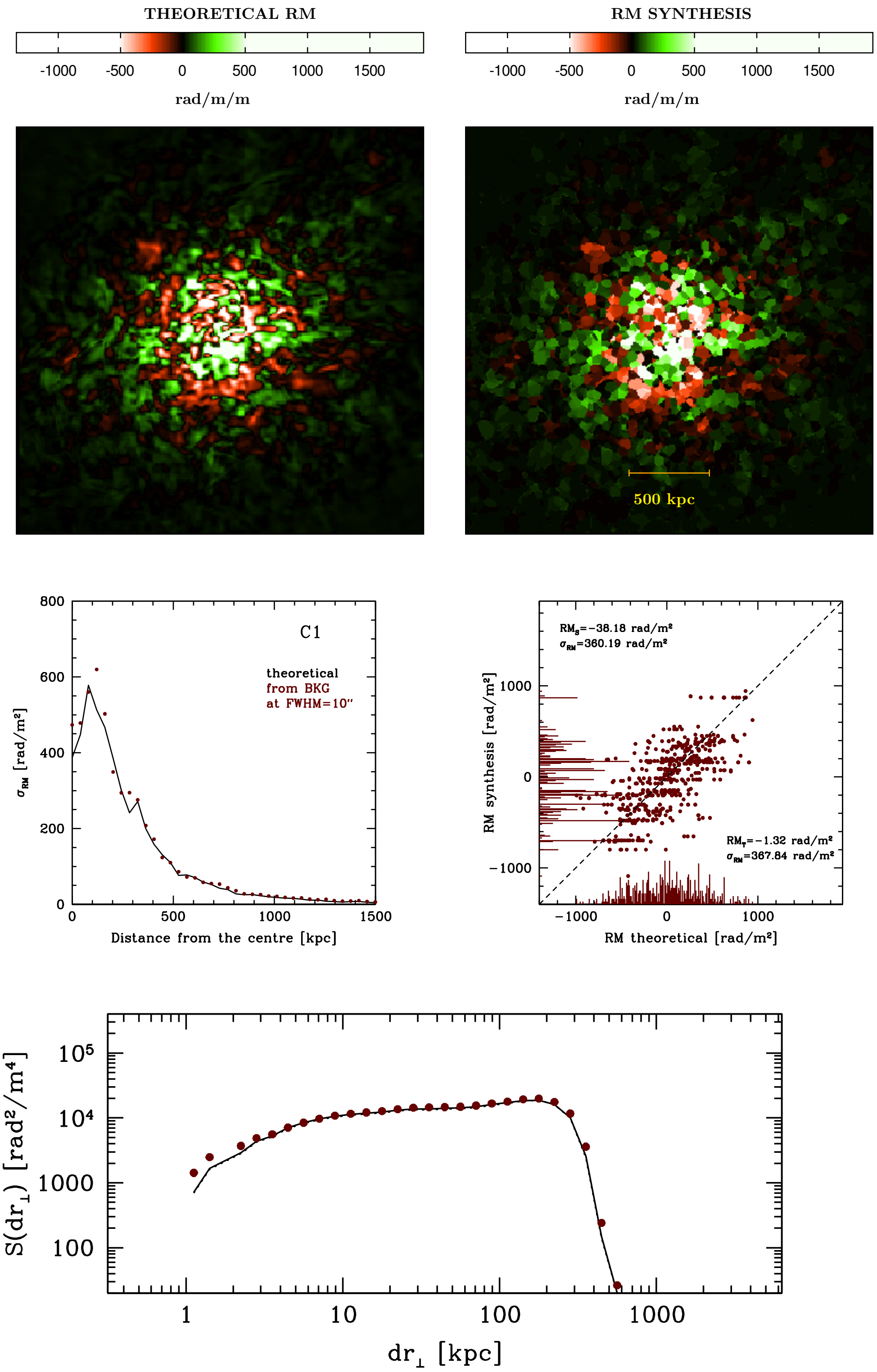

Figure 4.14 Results of the RM Synthesis technique on the *C1 background radio sources at FWHM=10″*. See Fig. 4.6 for the details.

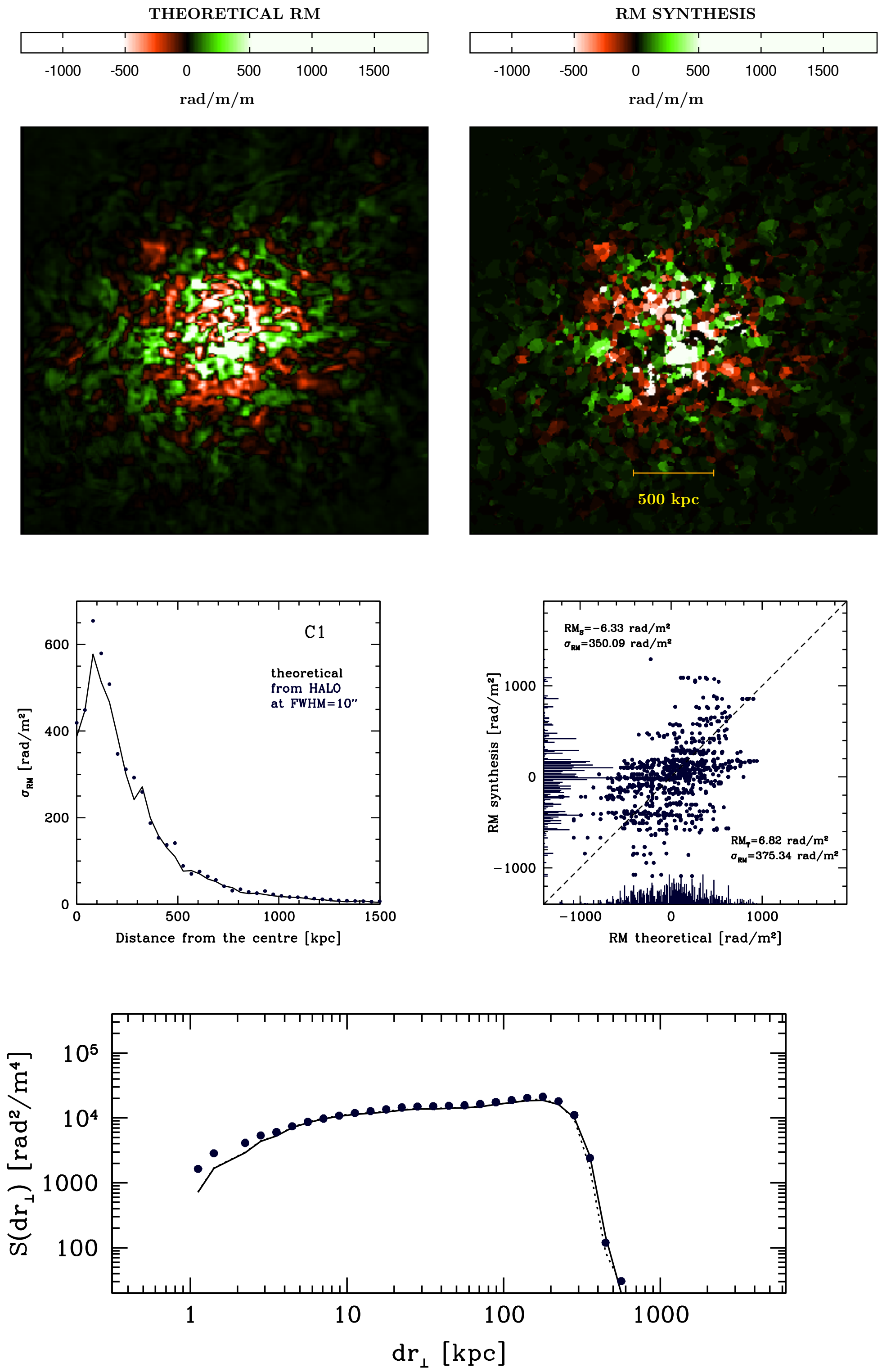

Figure 4.15 Results of the RM Synthesis technique on the *C1 radio halo at FWHM=10″*. See Fig. 4.7 for the details.

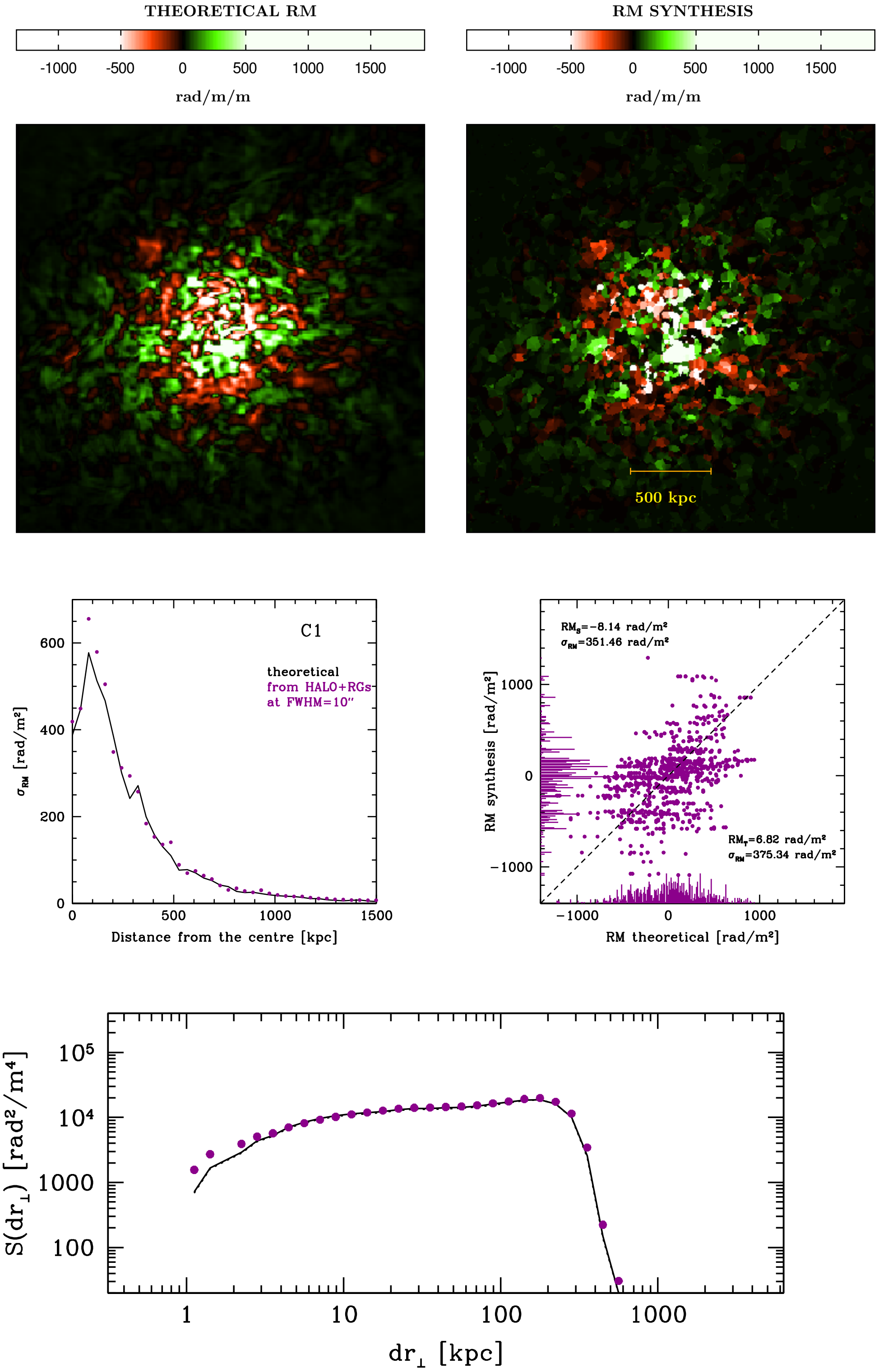

Figure 4.16 Results of the RM Synthesis technique on the *C1 radio halo plus the cluster, background and foreground radio sources at FWHM=10″*. See Fig. 4.8 for the details.

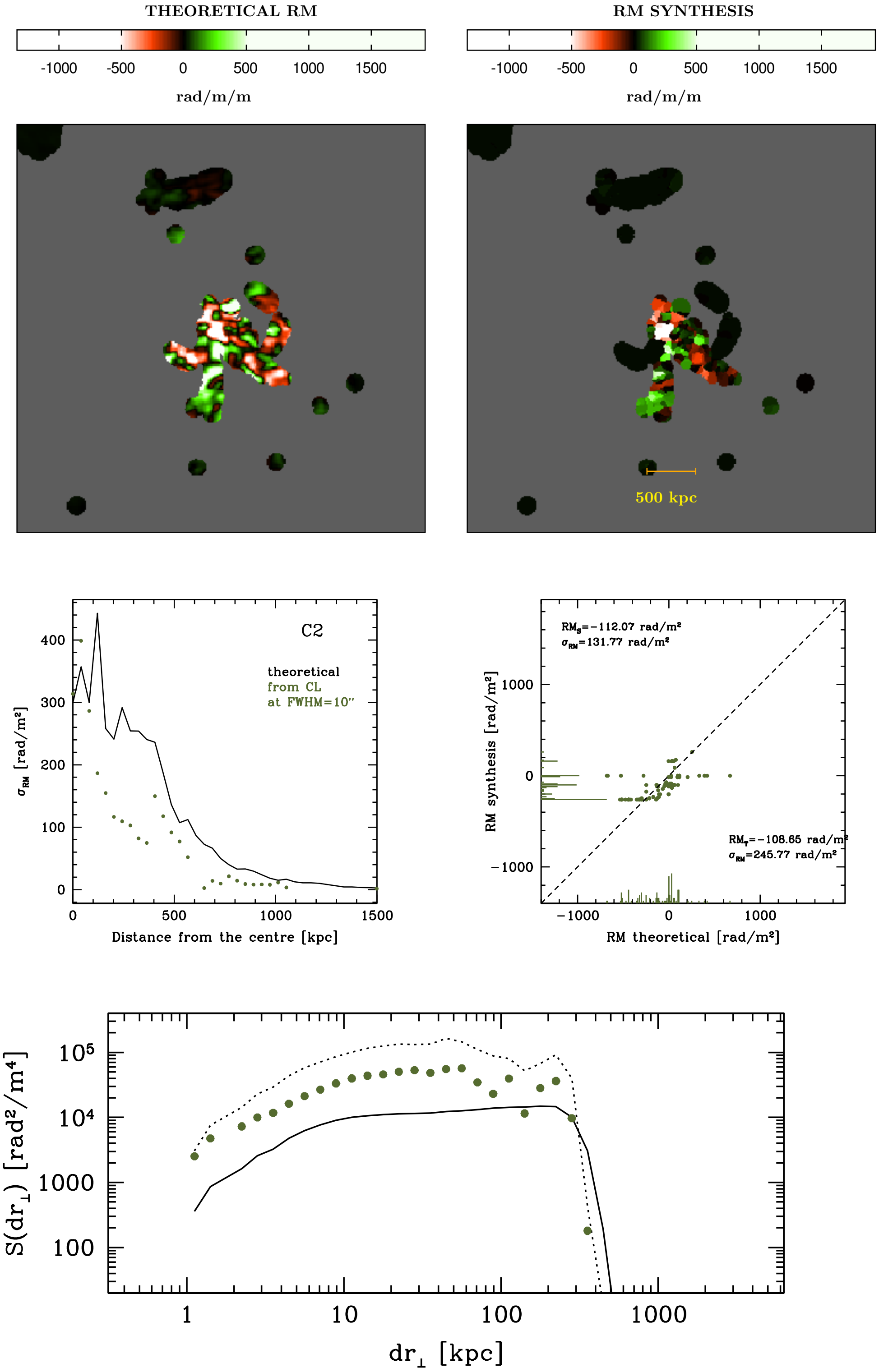

Figure 4.17 Results of the RM Synthesis technique on the *C2 cluster-embedded radio sources at FWHM=10″*. See Fig. 4.9 for the details.

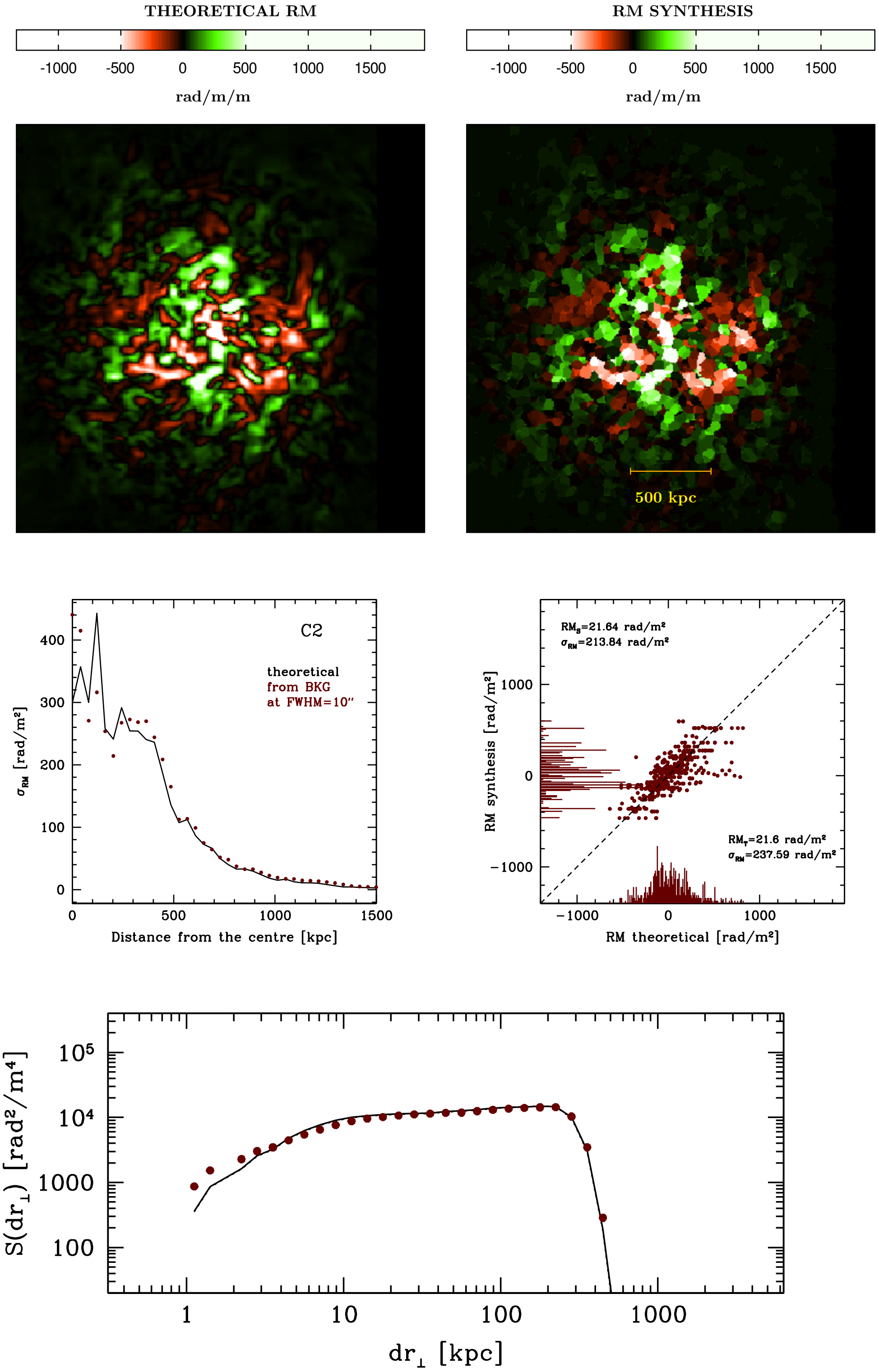

Figure 4.18 Results of the RM Synthesis technique on the *C2 background radio sources at FWHM=10″*. See Fig. 4.10 for the details.

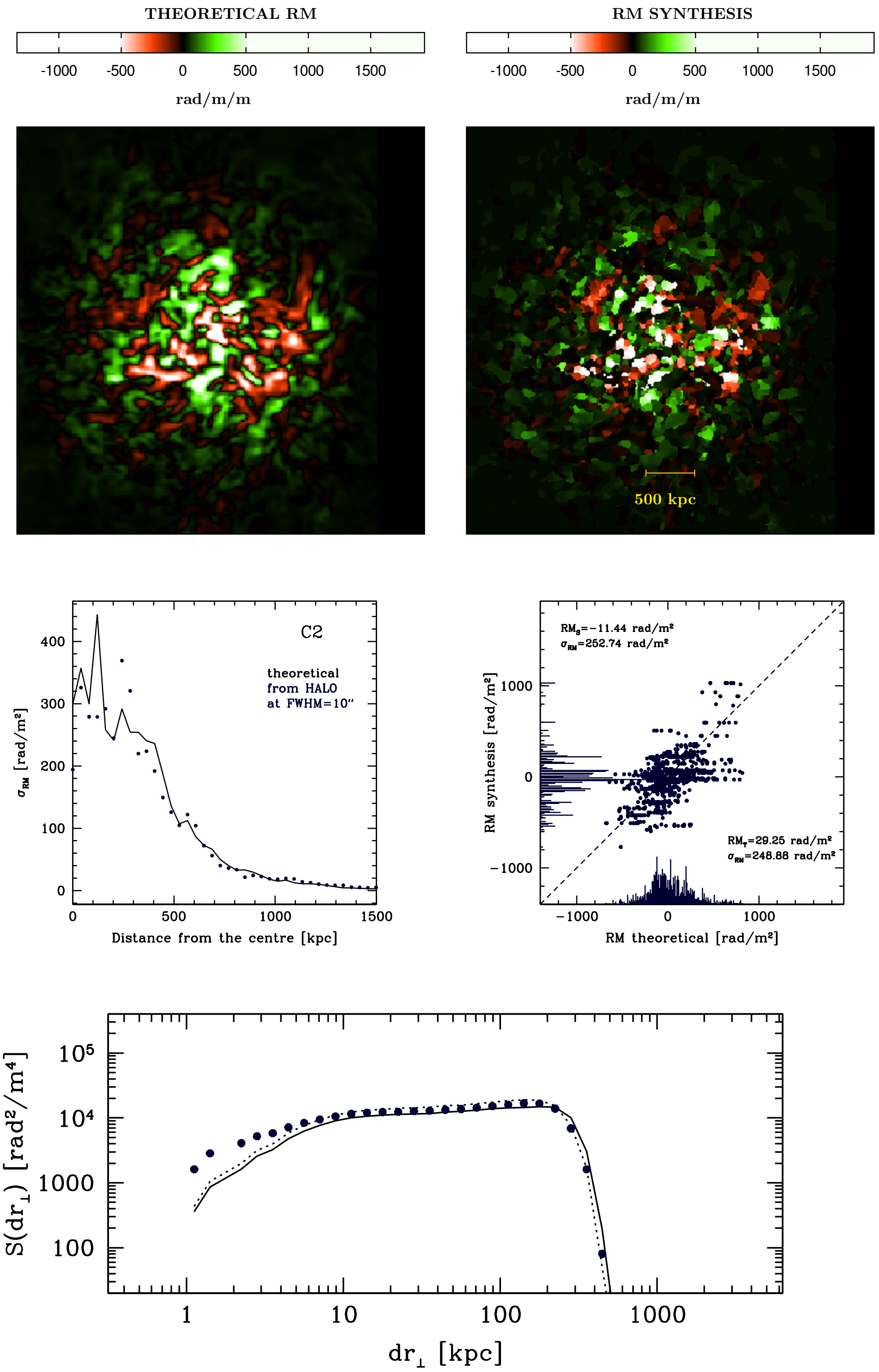

Figure 4.19 Results of the RM Synthesis technique on the *C2 radio halo at FWHM=10″*. See Fig. 4.11 for the details.

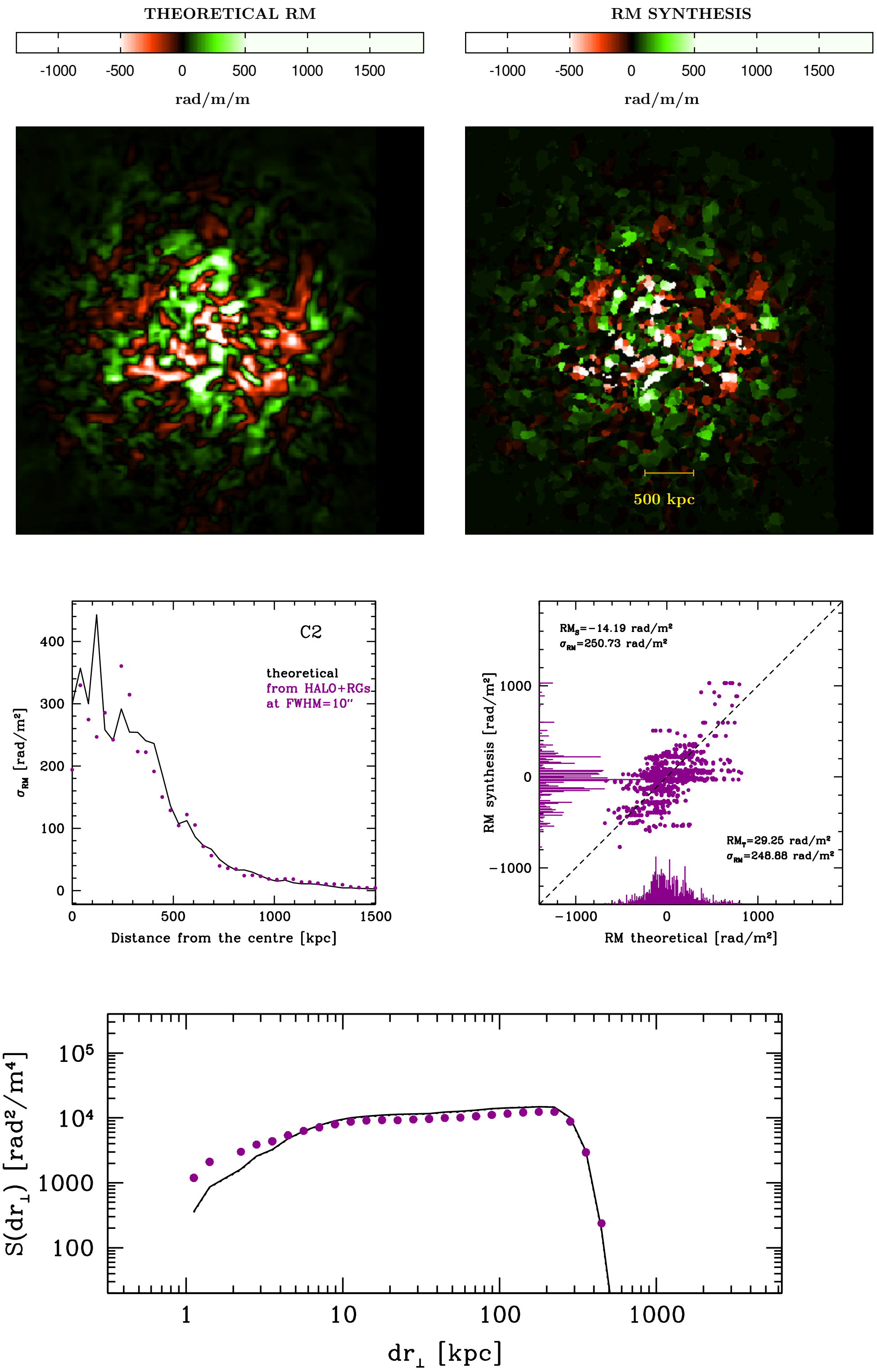

Figure 4.20 Results of the RM Synthesis technique on the *C2 radio halo plus the cluster, background and foreground radio sources at FWHM=10″*. See Fig. 4.12 for the details.

5

Summary and conclusions

The main motivation of this thesis was to address the origin of cosmic magnetism with particular focus on magnetic fields in galaxy clusters. These systems form at the intersections of cosmic web filaments and they represent unique laboratories to investigate the processes by means of which the primordial magnetic fields are spread and amplified to the levels observed in the local Universe.

There is a general consensus that magnetic fields are present in every galaxy cluster: they are a naturally occurring component in the intracluster medium unavoidably linked to the hot thermal plasma which shines in the X-rays (see Chapter 1). Although these fields are too weak to dramatically influence the dynamical state and evolution of galaxy clusters, they trace turbulent motions in the ICM, they alter the thermal conduction, and, perhaps more importantly, they reveal the presence of a still enigmatic non-thermal component composed by relativistic electrons with GeV energies distributed over Mpc-scales. This non-thermal component, whose origin is still debated, interacting with the intracluster magnetic field manifests itself through huge diffuse synchrotron sources known as radio haloes and peripheral arc-like sources known as relics. Radio haloes and relics are a direct evidence of the presence of a magnetic field in the intracluster medium, however these low-surface brightness sources are elusive and they have been observed only in a fraction of galaxy clusters. It has been proposed that these radio sources are powered by the energy released by merging phenomena through which galaxy clusters form and grow.

In Chapter 2, we presented the study of one of the most spectacular example of these systems: **CIZA J2242+5301**. In this galaxy cluster we can observe simultaneously a double-relic system connected by a giant radio halo of 2.7 Mpc in size. We collected new radio data with the Sardinia Radio Telescope in three frequency bands centred at 1.4 GHz, 6.6 GHz, and 19 GHz. These single-dish data were compared with interferometric observations taken with the WSRT, the GMRT, the VLA, as long as X-rays images obtained with the ROSAT satellite. Our observations permitted to study the radio spectrum of the relics up to 6.6 GHz, and to compare the measurements with models proposed to explain the acceleration mechanism of the relativistic electrons and the distribution of magnetic fields in these sources. Assuming simple diffusive shock acceleration, we interpret measurements of the northern relic with a continuous injection model. This yields an injection spectral index $\alpha_{\rm inj} = 0.7 \pm 0.1$ and a Mach number $\rm M = 3.3 \pm 0.9$, consistent with recent X-ray estimates. **Unlike other studies of the same object, no significant steepening of the relic radio emission is seen in data up to 8.35 GHz.** By fitting the southern relic spectrum with a simple power-law ($\rm S_\nu \propto \nu^{-\alpha}$) we obtained a spectral index $\alpha \approx 1.9$ corresponding to a Mach number $\rm M \approx 1.8$ in agreement with X-ray estimates. Finally, we evaluated the rotation measure of the northern relic at 6.6 GHz. These results provide new insights on the magnetic structure of the relic, but further observations are needed to clarify the nature of the observed Faraday rotation.

Radio haloes and relics are dramatic manifestations of intracluster magnetic fields. However, these elusive sources are rare, while magnetic fields are likely to be ubiquitous. Indeed, magnetic fields themselves are not directly observable but we can infer their presence by the indirect effect that they cause on the polarized radio waves that cross the hot plasma in which they are contained. The position angle of the polarization plane rotates by an amount proportional to the Rotation Measure (RM), the path integral of the parallel magnetic field times the thermal plasma density through the intracluster medium. This is the so-called Faraday rotation effect. If the distribution of the thermal electron is known, from X-rays or SZ observations, we can invert the RM equation to reconstruct the strength and structure of the underlying magnetic field. This is however not a trivial task even for very simple magnetic fields and gas density distributions and in general it requires a numerical approach. In addition, in order to successfully apply this technique we need a large number of radio sources embedded or in the background of a galaxy cluster.

The advent of the Square Kilometre Array will have an unprecedented impact in the study of Faraday rotation. An all-sky survey at 1.4 GHz will be proposed for the SKA with the aim to acquire an accurate map of the RM based on a enormous number of radio sources spread over cosmological distances. The spatial density of these radio sources will be such that we will obtain a RM grid with several hundreds of sources per squared degree. **In this thesis, we developed an original numerical approach that is able to produce realistic images in full-Stokes of the radio sky very close to the images of galaxy clusters that will be obtained with the SKA.** Moreover, these synthetic spectral-polarimetric cubes can be used as a tool to determine the precision of the RM Synthesis technique in reconstructing the properties of the intracluster magnetic fields. In Chapter 3, we described the procedure and the models we developed to produce simulated full-Stokes images of the radio sky. The predictions of our modelling have been compared with the radio source counts both in total intensity and polarization available in literature. **In addition, we presented the estimates of the confusion limits of I, U, and Q Stokes parameters versus different values of beam resolutions obtained from our simulations.**

As already pointed out, with the SKA it will be possible to accurately study the intracluster magnetic fields with the observation of hundreds of radio sources per squared degree, which will cover the entire cluster volume. In addition, the SKA will be able to detect the polarization of radio haloes which has been proven to be extremely difficult with the current instruments. In Chapter 4, we explored the potentialities of the SKA in reconstructing the RM images associated to the magneto-ionic medium of galaxy clusters. This required the simulation and then the analysis of a huge amount of synthetic data, as it will be for the case of the real SKA observations. By using the original numerical approach developed in this

thesis and state-of-the art cosmological magneto-hydro-dynamical simulations of the ICM properties we tried to address this challenging question.
We presented the simulated observations of a pair of two merging galaxy clusters as it would be observed by the SKA1-MID at 1.4 GHz with a beam resolution of 2.5″. These simulations include the discrete radio sources and two radio haloes. We apply the RM synthesis technique on the simulated data at 2.5″ and also on the data convolved at a beam resolution of 10″ to show the impact of beam depolarization. **According to our results, we can state that at both the resolutions we can obtain reliable estimates of the RM of galaxy clusters if the exposure time is such that we reach the confusion level on data.** The number of background radio sources forming the RM grid is enough to permit a precise reconstruction of the RM properties in the majority of galaxy clusters. The presence of radio haloes could significantly help in determine the RM values although the interpretation of the RM Synthesis results is not trivial.

The research work conducted as part of this thesis led to the following **publications** sorted in order of relevance:

- **Loi, F.**, Murgia, M., Govoni, F., et al. 2017, *"Observations of the galaxy cluster CIZA J2242.8+5301 with the Sardinia Radio Telescope"*, published in *MNRAS*, 472, 3605
- Govoni, F., Murgia, M., Vacca, V., **Loi, F.**, et al. 2017, *"Sardinia Radio Telescope observations of Abell 194 - the intra-cluster magnetic field power spectrum"*, published in *A&A*, 603, A122
- Murgia, M., Govoni, F., Carretti, E., Melis, A., Concu, R., Trois, A., **Loi, F.**, et al. 2016, *"Sardinia Radio Telescope wide-band spectral-polarimetric observations of the galaxy cluster 3C 129"*, published in *MNRAS*, 461, 3516
- **Loi, F.**, Murgia, M., Govoni, F., et al. 2017,*"Magnetic fields in galaxy clusters in the SKA era"*, proceedings of *7^{th} Young Researcher Meeting*, published in Journal of Physics: Conference Series, 841 012005
- Govoni, F., Murgia, M., Vacca, V., **Loi, F.**, et al. 2015,*"Magnetism and continuum surveys working together"*, Proceedings of *The Many Facets of Extragalactic Radio Surveys: Towards New Scientific Challenges*, 36

In addition the Candidate had the chance to collaborate in the following publications:

- Prandoni, I., Murgia, M., Tarchi, A., Burgay, M., Castangia, P., Egron, E., Govoni, F., Pellizzoni, A., Ricci, R., Righini, S., Bartolini, M., Casu, S., Corongiu, A., Iacolina, M. N., Melis, A., Nasir, F. T., Orlati, A., Perrodin, D., Poppi, S., Trois, A., Vacca, V., Zanichelli, A., Bachetti, M., Buttu, M., Comoretto, G., Concu, R., Fara, A., Gaudiomonte, F., **Loi, F.**, et al. 2017, *"The Sardinia Radio Telescope: From a Technological Project to a Radio Observatory"*, published in *A&A*, 608, A40
- Egron, E., Pellizzoni, A., Iacolina, M. N., Loru, S., Marongiu, M., Righini, S., Cardillo, M., Giuliani, A., Mulas, S., Murtas, G., Simeone, D., Concu, R., Melis, A., Trois, A., Pilia, M., Navarrini, A., Vacca, V., Ricci, R., Serra, G., Bachetti, M., Buttu, M., Perrodin, D., Buffa, F., Deiana, G. L., Gaudiomonte, F., Fara, A., Ladu, A., **Loi, F.**, et al. 2017, *"Imaging of SNR IC443 and W44 with the Sardinia Radio Telescope at 1.5 GHz and 7 GHz"*, published in MNRAS, 470, 1329

A

The Stokes parameters

The Stokes parameters described the polarized emission coming from a radio source. In particular:

- I is the total intensity of the signal;
- Q and U are related to the elliptical polarization;
- V represents the circular polarization.

Actually, just three of them are independent parameters, because it results:

$$I \geqslant Q^2 + U^2 + V^2. \tag{A.1}$$

The polarized emission of the source is given by

$$P = \sqrt{Q^2 + U^2 + V^2} \tag{A.2}$$

therefore, the degree of polarization of the source is:

$$\Pi = \frac{P}{I} = \frac{\sqrt{Q^2 + U^2 + V^2}}{I} \tag{A.3}$$

while the polarization angle is defined as:

$$\Psi = \frac{1}{2} \text{arctg} \left(\frac{U}{Q} \right). \tag{A.4}$$

For the sources considered in this thesis the circular polarization is null, that is V=0.

B

The equipartition condition

The intensity of a synchrotron source is related to the magnetic field energy density and to the relativistic electron energy density. The same intensity can be obtained from a different combinations of these two physical quantities. However, there is a particular combination that minimized the total energy content of the source. This condition is achieved for a particular value of the magnetic field strength that we indicate with $\mathrm{B}_{\mathrm{min}}$. Incidentally, it is found that for this particular value of B, the energy density of the magnetic field and also of the particles are very similar and thus, we often refer to this particular magnetic field strength as to the equipartition magnetic field.

To the total energy U_{tot} of the radio source two elements contribute, i.e. the magnetic field energy U_{B} and the relativistic particles one $(1+\kappa)\cdot U_{\mathrm{el}}$:

$$U_{\mathrm{tot}} = (1+\kappa)\cdot U_{\mathrm{el}} + U_{\mathrm{B}} \tag{B.1}$$

where κ is the ratio of the heavy particle to electron energy densities. The magnetic field energy is:

$$U_{\mathrm{B}} = \phi \cdot V \cdot \frac{B^2}{8\pi} \tag{B.2}$$

where V is the volume of the radio source and ϕ is the filling factor that is the fraction of the volume of the source occupied by the magnetic field. The total energy of relativistic electrons is:

$$U_{\mathrm{el}} = V \int_{-\pi/2}^{\pi/2} \int_{\epsilon_{\mathrm{min}}}^{\epsilon_{\mathrm{max}}} N(\epsilon,\theta)\cdot\epsilon\cdot d\epsilon \cdot \frac{\sin\theta}{2}\cdot d\theta = V\cdot N_0 \cdot \left[\frac{\epsilon_{\mathrm{max}}^{1-2\alpha} - \epsilon_{\mathrm{min}}^{1-2\alpha}}{1-2\alpha}\right]. \tag{B.3}$$

The source luminosity $\mathrm{L}_{\mathrm{syn}}$ is related to the emissivity j_{ν} as:

$$L_{\mathrm{syn}} = V\cdot\langle j_{\nu}(\theta)\rangle_{LOS} = V\cdot\langle C(\alpha_{inj})\rangle_{LOS}\cdot N_0 \cdot B^{1+\alpha_{inj}}\cdot\nu^{-\alpha_{inj}},$$

where $\langle\cdots\rangle_{\mathrm{LOS}}$ indicates the average along the line-of-sight while $\langle \mathrm{C}(\alpha_{\mathrm{inj}})\rangle_{\mathrm{LOS}}$ is a constant related to the spectral index of the source. By substituting in the relativistic electron energy

$V \cdot N_0$ with respect to the luminosity:

$$U_{\rm el} = \frac{\epsilon_{\rm max}^{1-2\alpha} - \epsilon_{\rm min}^{1-2\alpha}}{1-2\alpha} \cdot \frac{1}{C_\alpha \nu^{-\alpha}} \cdot \frac{L_{\rm syn}}{B^{1+\alpha}}, \tag{B.4}$$

the total energy becomes:

$$U_{\rm tot} = (1+\kappa) \cdot \frac{\epsilon_{\rm max}^{1-2\alpha} - \epsilon_{\rm min}^{1-2\alpha}}{1-2\alpha} \cdot \frac{1}{C_\alpha \nu^{-\alpha}} \cdot \frac{L_{\rm syn}}{B^{1+\alpha}} + \phi \cdot V \cdot \frac{B^2}{8\pi}. \tag{B.5}$$

This function has a minimum for a magnetic field given by (Brunetti et al. 1997; Beck & Krause 2005):

$$B_{\rm min} = \left(\frac{4\pi}{C^\alpha} \cdot \frac{\epsilon_{\rm max}^{1-2\alpha} - \epsilon_{\rm min}^{1-2\alpha}}{1-2\alpha} \cdot (1+\alpha) \cdot (1+\kappa) \cdot \nu^\alpha \cdot \frac{L_{\rm syn}}{\phi \cdot V} \right)^{\frac{1}{3+\alpha}}. \tag{B.6}$$

When α=1, this value of the magnetic field guarantees a perfect equipartition of the energy between the magnetic field and the relativistic particles. The magnetic field in this condition is the equipartition magnetic field.
Under the previous assumptions we can to derive a value for the intracluster magnetic field strength and this is a quite common way to derive it in literature. Obviously, the resulting values are affected by the assumption made and they have to take with care.

C

Single scale magnetic field model

A magnetic field tangled on a single scale $\Lambda_{\rm C}$ randomly oriented from cell to cell results in a Gaussian-like RM distribution with zero mean $\langle RM \rangle$ and dispersion $\sigma_{\rm RM}$ given by:

$$\sigma^2_{\rm RM} = \langle RM^2 \rangle = 812^2 \Lambda_{\rm C} \int (n_{\rm e} B_{||})^2 dl, \tag{C.1}$$

if $\Lambda_{\rm c} << {\rm L}$ where L is the thermic plasma length along the line-of-sight. The observed RM is indeed the result of a random walk over N cells along the line-of-sight where ${\rm N} = \frac{\rm L}{\Lambda_{\rm c}}$ and ${\rm RM_{cell}}$ is:

$$RM_{cell} = 812 \frac{B_0}{\sqrt{3}} n_e \Lambda_c \tag{C.2}$$

where ${\rm B_0} = \sqrt{B_x^2 + B_y^2 + B_z^2}$ e assuming an isotropic magnetic field (${\rm B_0} = \sqrt{3}{\rm B_z}$).

If the thermal gas density is supposed to decrease with the distance from the cluster centre according to a β-model (Cavaliere & Fusco-Femiano 1976):

$$n_e = n_0 \left(1 + \frac{r^2}{r_c^2}\right)^{-3\beta/2}, \tag{C.3}$$

and the magnetic field strength radial profile to be a function of the thermal gas density:

$$B = B_0 \left(\frac{n_e}{n_0}\right)^{\eta} \tag{C.4}$$

with η in the range 0.5−1, the integral in Eq. C.1 becomes:

$$\begin{aligned}
\sigma^2_{\rm RM} = \frac{812^2}{3} \Lambda_C \int_0^{\infty} B^2 n_{\rm e}^2 dl = \frac{812^2}{3} B_0^2 \Lambda_{\rm C} n_0^2 \int_0^{\infty} \left(1 + \frac{r^2}{r_{\rm c}^2}\right)^{-3\beta(1+\eta)} dl \\
= \frac{812^2}{3} B_0^2 \Lambda_C n_0^2 \int_0^{\infty} \frac{1}{\left(1 + \frac{r^2}{r_{\rm c}^2}\right)^{3\beta(1+\eta)}} dl \\
= 2 \frac{812^2}{3} B_0^2 \Lambda_C n_0^2 \int_0^{\infty} \frac{1}{\left(1 + \frac{r_{\perp}^2}{r_{\rm c}^2} + \frac{l^2}{r_{\rm c}^2}\right)^{3\beta(1+\eta)}} dl
\end{aligned}$$

where $r^2 = r_\perp^2 + l^2$. By using the Beta function:

$$\int_0^\infty \frac{l^{\mathrm{a}} dl}{(m + l^{\mathrm{b}})^{\mathrm{c}}} = \frac{m^{\frac{\mathrm{a}+1-\mathrm{bc}}{\mathrm{b}}}}{b} \left[\frac{\Gamma(\frac{a+1}{b})\Gamma(c - \frac{a+1}{b})}{\Gamma(c)} \right]; \qquad \Big(a > -1, b > 0, m > 0, c > \frac{a+1}{b}\Big)$$

we obtain:

$$\sigma_{\mathrm{RM}}^2 = 2\frac{812^2}{3} B_0^2 \Lambda_{\mathrm{C}} n_0^2 \int_0^\infty \frac{dl}{\left(1 + \frac{r_\perp^2}{r_{\mathrm{c}}^2} + \frac{l^2}{r_{\mathrm{c}}^2}\right)^{3\beta(1+\eta)}} =$$

$$= 2\frac{812^2}{3} B_0^2 \Lambda_{\mathrm{C}} n_0^2 r_{\mathrm{c}} \frac{1}{2} \left(1 + \frac{r_\perp^2}{r_{\mathrm{c}}^2}\right)^{\frac{1-6\beta(1+\eta)}{2}} \Gamma(\frac{1}{2}) \frac{\Gamma[3\beta(1+\eta) - \frac{1}{2}]}{\Gamma[3\beta(1+\eta)]} =$$

$$= \frac{812^2}{3} B_0^2 \Lambda_{\mathrm{C}} n_0^2 r_{\mathrm{c}} \left(1 + \frac{r_\perp^2}{r_{\mathrm{c}}^2}\right)^{\frac{1-6\beta(1+\eta)}{2}} \Gamma(\frac{1}{2}) \frac{\Gamma[3\beta(1+\eta) - \frac{1}{2}]}{\Gamma[3\beta(1+\eta)]} =$$

$$= \frac{812^2}{3} B_0^2 \Lambda_{\mathrm{C}} n_0^2 r_{\mathrm{c}} \sqrt{\pi} \left(1 + \frac{r_\perp^2}{r_{\mathrm{c}}^2}\right)^{\frac{1-6\beta(1+\eta)}{2}} \frac{\Gamma[3\beta(1+\eta) - \frac{1}{2}]}{\Gamma[3\beta(1+\eta)]}.$$

So, the dispersion is:

$$\sigma_{\mathrm{RM}}(r_\perp) = K B_0 \Lambda_{\mathrm{C}}^{\frac{1}{2}} n_0 r_c^{\frac{1}{2}} \frac{1}{(1 + r_\perp^2/r_{\mathrm{c}}^2)^{\frac{6\beta(1+\eta)-1}{4}}} \sqrt{\frac{\Gamma[3\beta(1+\eta) - \frac{1}{2}]}{\Gamma[3\beta(1+\eta)]}}, \qquad \text{(C.5)}$$

where K is a constant which depends on the integral path of the density distribution (K=624 for background sources, K=441 for sources lying in the middle of the cluster).

The single-scale model is a good way to determine the magnetic field strength provided that we have reliable values of all the other parameters which define the σ_{RM} in Eq. C.5 and an accurate measure of the σ_{RM}. Nevertheless, a more realistic model requires a magnetic field tangled on a range of scales. In this case the appropriate scale to use for Λ_{C} is the magnetic field auto-correlation length Λ_{B}.

Bibliography

Aharonian, F., Akhperjanian, A.G., Anton, G., et al. 2009a, A&A 495, 27

Aharonian, F., Akhperjanian, A.G., Anton, G., et al. 2009b, A&A 502, 437

Aleksić, J., Antonelli, L.A., Antoranz, P., et al. 2010, ApJ710, 634

Akamatsu H., & Kawahara H. 2013, PASJ, 65, 16

Akamatsu H., van Weeren R. J., Ogrean G. A., et al. 2015, A&A, 582, A87

Bell, A. R. 1978, MNRAS, 182, 147

Bagchi, J., Sirothia, S. K., Werner, N., et al. 2011, ApJ, 736, L8

Basu K., Vazza F., Erler J., & Sommer M. 2016, A&A, 591, A142

Beck R., Krause M., 2005, Astronomische Nachrichten 326, 414

Biskamp, D. 2003, Magnetohydrodynamic Turbulence, by Dieter Biskamp, pp. 310. ISBN 0521810116. Cambridge, UK: Cambridge University Press, September 2003., 310

Blandford, R., & Eichler, D. 1987, Phys. Rep., 154, 1

Blasi, P., & Colafrancesco, S. 1999, Astroparticle Physics, 12, 169

Boller T., Freyberg M. J., Trümper J., et al. 2016, A&A, 588, A103

Bolli P., Orlati A., Stringhetti L., et al. 2015, Journal of Astronomical Instrumentation, 4, 1550008-880

Bonafede A., Feretti L., Giovannini G., et al. 2009, A&A, 503, 707

Bonafede, A., Feretti, L., Murgia, M., et al. 2010, A&A, 513, A30

Bonafede, A., Dolag, K., Stasyszyn, F., Murante, G., & Borgani, S. 2011, MNRAS, 418, 2234

Bonafede, A., Vazza, F., Brüggen, M., et al. 2013, MNRAS, 433, 3208

Bonafede A., Intema H. T., Brüggen M., et al. 2014a, ApJ, 785, 1

Bonafede, A., Intema, H. T., Brüggen, M., et al. 2014b, MNRAS, 444, L44

Bondi, M., Ciliegi, P., Zamorani, G., et al. 2003, A&A, 403, 857

Bondi, M., Ciliegi, P., Schinnerer, E., et al. 2008, ApJ, 681, 1129-1135

Botteon A., Gastaldello F., Brunetti G., & Kale, R. 2016, MNRAS, 463, 1534

Brentjens M. A., de Bruyn A. G., 2005, A&A, 441, 1217

Bridle, A. H., Hough, D. H., Lonsdale, C. J., Burns, J. O., & Laing, R. A. 1994, AJ, 108, 766

Brüggen, M., Ruszkowski, M., Simionescu, A., Hoeft, M., & Dalla Vecchia, C. 2005, ApJ, 631, L21

Brunetti G., Setti G., Comastri A., 1997, A&A 325, 898

Brunetti, G., & Jones, T. W. 2014, International Journal of Modern Physics D, 23, 1430007-98

Burn B. J. 1966, MNRAS, 133, 67

Burns, J. O., Sulkanen, M. E., Gisler, G. R., & Perley, R. A. 1992, ApJ, 388, L49

Cantwell, T. M., Scaife, A. M. M., Oozeer, N., Wen, Z. L., & Han, J. L. 2016, MNRAS, 458, 1803

Carilli, C. L., Perley, R. A., Dreher, J. W., & Leahy, J. P. 1991, ApJ, 383, 554

Carilli C. L., & Taylor G. B. 2002, ARA&A, 40, 319

Carretti E., Brown S., Staveley-Smith L., et al. 2013, MNRAS, 430, 1414

Cavaliere, A., & Fusco-Femiano, R. 1976, aap, 49, 137

Clarke, T. E., Kronberg, P. P., Böhringer, H. 2001, ApJ, 547, L111

Collins, D. C., Xu, H., Norman, M. L., Li, H., & Li, S. 2010, ApJS, 186, 308

Condon, J. J. 1974, ApJ, 188, 279

Condon, J. J. 1984, ApJ, 284, 44

Condon, J. J. 1989, ApJ, 338, 13

Condon, J. J. 1996, Extragalactic Radio Sources, 175, 535

Condon J. J., Cotton W. D., Greisen E. W., et al. 1998, AJ, 115, 1693

Condon, J. J. 2002, Single-Dish Radio Astronomy: Techniques and Applications, 278, 155

Condon, J. J., Cotton, W. D., Fomalont, E. B., et al. 2012, ApJ, 758, 23

Dasadia S., Sun M., Sarazin C., et al. 2016, ApJ, 820, L20

Dawson W. A., Jee M. J., Stroe A., et al. 2015, ApJ, 805, 143

Dennison, B. 1980, ApJ, 239, L93

Dewdney, P. et al., 2015, SKA1 SYSTEM BASELINE DESIGN V2

Dolag, K., & Enßlin, T. A. 2000, A&A, 362, 151

Dolag, K., Bartelmann, M., & Lesch, H. 2002, A&A, 387, 383

Dolag, K., Bykov, A. M., & Diaferio, A. 2008, Space Sci. Rev., 134, 311

Donnert, J., Dolag, K., Lesch, H., Müller, E. 2009, MNRAS, 392, 1008

Donnert J. M. F., Stroe A., Brunetti G., Hoang D., & Roettgering H. 2016, MNRAS, 462, 2014

Donnert, J. M. F., Beck, A. M., Dolag, K., & Röttgering, H. J. A. 2017, MNRAS, 471, 4587

Drury L. O. 1983, Reports on Progress in Physics, 46, 973

Dubois, Y., & Teyssier, R. 2008, A&A, 482, L13

Dubois, Y., Devriendt, J., Slyz, A., & Silk, J. 2009, MNRAS, 399, L49

Ebeling H., Mullis C. R., & Tully R. B. 2002, ApJ, 580, 774

Ebeling H., Edge A. C., Burgett W. S., et al. 2013, MNRAS, 432, 62

Eilek, J. A., & Owen, F. N. 2002, ApJ, 567, 202

Emerson D. 2002, Single-Dish Radio Astronomy: Techniques and Applications, 278, 27

Ensslin T.A., Biermann P.L., Kronberg P.P., Wu X.P., 1997, ApJ 477, 560

Ensslin T. A., Biermann P. L., Klein U., & Kohle, S. 1998, A&A, 332, 395

Enßlin, T. A., & Vogt, C. 2003, A&A, 401, 835

Fabian, A. C. 1994, ARA&A, 32, 277

Fabian, A. C., Sanders, J. S., Ettori, S., et al. 2000, MNRAS, 318, L65

Farnsworth D., Rudnick L., Brown S., & Brunetti G. 2013, ApJ, 779, 189

Feretti, L., Dallacasa, D., Giovannini, G., & Tagliani, A. 1995, A&A, 302, 680

Feretti, L., Dallacasa, D., Govoni, F., et al. 1999, A&A, 344, 472

Feretti L., Giovannini G., Govoni F., & Murgia M. 2012, A&A Rev., 20, 54

Ferrari, C., Govoni, F., Schindler, S., Bykov, A. M., & Rephaeli, Y. 2008, Space Sci. Rev., 134, 93

Ferrari, C., Intema, H. T., Orrù, E., et al. 2011, A&A, 534, L12

Furlanetto S.R., Loeb A., 2001, ApJ 556, 619

Giacintucci, S., Venturi, T., Murgia, M., et al. 2007, A&A, 476, 99

Giacintucci, S., Kale, R., Wik, D. R., Venturi, T., & Markevitch, M. 2013, ApJ, 766, 18

Giacintucci, S., Markevitch, M., Venturi, T., et al. 2014, ApJ, 781, 9

Girardi M., Boschin W., Gastaldello F., et al. 2016, MNRAS, 456, 2829

Giovannini, G., Feretti, L., & Stanghellini, C. 1991, A&A, 252, 528

Giovannini, G., Feretti, L., Venturi, T., Kim, K.-T., & Kronberg, P. P. 1993, ApJ, 406, 399

Giovannini, G., Tordi, M., & Feretti, L. 1999, New Astronomy, 4, 141

Giovannini, G., & Feretti, L. 2000, New Astronomy, 5, 335

Giovannini G., Vacca V., Girardi M., et al. 2013, MNRAS, 435, 518

Govoni, F., Taylor, G. B., Dallacasa, D., Feretti, L., & Giovannini, G. 2001, A&A, 379, 807

Govoni, F., & Feretti, L. 2004, International Journal of Modern Physics D, 13, 1549

Govoni F., Murgia M., Feretti, L. et al., 2005, A&A, 430, L5

Govoni, F., Murgia, M., Feretti, L., et al. 2006, A&A, 460, 425

Govoni F., Dolag K., Murgia M., et al. 2010, A&A, 522, A105

Govoni F., Ferrari C., Feretti L., et al. 2012, A&A, 545, A74

Govoni, F., Murgia, M., Xu, H., et al. 2013, A&A, 554, A102

Govoni, F., Murgia, M., Vacca, V., et al. 2015, The Many Facets of Extragalactic Radio Surveys: Towards New Scientific Challenges, 36

Govoni F., Murgia M., Vacca V., et al. 2017, A&A, 603, A122

Grasso, D., & Rubinstein, H. R. 2001, Phys. Rep., 348, 163

Guidetti, D., Murgia, M., Govoni, F., et al. 2008, A&A, 483, 699

Guidetti, D., Laing, R. A., Murgia, M., et al. 2010, A&A, 514, A50

Hales, C. A., Norris, R. P., Gaensler, B. M., & Middelberg, E. 2014, MNRAS, 440, 3113

Hoang D. N., Shimwell, T. W., Stroe, A., et al. 2017, arXiv:1706.09903

Inskip K. J., Best P. N., Longair M. S., & MacKay D. J. C. 2002, MNRAS, 329, 277

Intema H. T., Jagannathan P., Mooley K. P., & Frail D. A. 2017, A&A, 598, A78

Jaffe, W. J. 1977, ApJ, 212, 1

Jarrett, T. H. 2000, PASP, 112, 1008

Johnston-Hollitt, M., & Ekers, R. D. 2004, arXiv:astro-ph/0411045

Johnston-Hollitt, M., Govoni, F., Beck, R., et al. 2014, Proceedings of Advancing Astrophysics with the Square Kilometre Array (AASKA14). 9 -13 June, 2014. Giardini Naxos, Italy.

Laing, R. A., Bridle, A. H., Parma, P., & Murgia, M. 2008, MNRAS, 391, 521

Laing, R. A., & Bridle, A. H. 2008, Extragalactic Jets: Theory and Observation from Radio to Gamma Ray, 386, 104

Lin, Y.-T., & Mohr, J. J. 2007, ApJS, 170, 71

Lindner, R. R., Baker, A. J., Hughes, J. P., et al. 2014, ApJ, 786, 49

Loi, F., Murgia, M., Govoni, F., et al. 2017, Proceedings of 7^{th} Young Researcher Meeting, Journal of Physics: Conference Series 841, doi:10.1088/1742-6596/841/1/012005

Loi, F., Murgia, M., Govoni, F., et al. 2017, MNRAS, 472, 3605

Kale, R., Venturi, T., Giacintucci, S., et al. 2015, A&A, 579, A92

Kang H., & Ryu D. 2016, ApJ, 823, 13

Kardashev, N. S. 1962, Soviet Ast., 6, 317

Kellermann, K. I., Fomalont, E. B., Mainieri, V., et al. 2008, ApJS, 179, 71

Kempner, J. C., & Sarazin, C. L. 2001, ApJ, 548, 639

Kierdorf, M., Beck, R., Hoeft, M., et al. 2017, A&A, 600, A18

Killeen N. E. B., Bicknell G. V., & Ekers R. D. 1986, ApJ, 302, 306

Knowles, K., Intema, H. T., Baker, A. J., et al. 2016, MNRAS, 459, 4240

Kocevski D. D., Ebeling H., Mullis C. R., & Tully R. B. 2007, ApJ, 662, 224

Kronberg P.P., Lesch H., Hopp U., 1999, ApJ 511, 56

Kuchar, P., & Enßlin, T. A. 2011, A&A, 529, A13

Kulsrud, R. M., Cen, R., Ostriker, J. P., & Ryu, D. 1997, ApJ, 480, 481

Markevitch, M., & Vikhlinin, A. 2007, physrep, 443, 1

Martinez Aviles G., Ferrari C., Johnston-Hollitt M., et al. 2016, A&A, 595, A116

Mauch, T., & Sadler, E. M. 2007, MNRAS, 375, 931

McNamara, B. R., & Nulsen, P. E. J. 2007, ARA&A, 45, 117

Mogavero F., & Schekochihin A. A. 2014, MNRAS, 440, 3226

Murgia M., Fanti C., Fanti R., et al. 1999, A&A, 345, 769

Murgia, M., Govoni, F., Feretti, L., et al. 2004, A&A, 424, 429

Murgia, M., Govoni, F., Feretti, L., & Giovannini, G. 2010, A&A, 509, A86

Murgia M., Parma P., Mack K.-H., et al. 2011, A&A, 526, A148

Murgia M., Govoni F., Carretti E., et al. 2016, MNRAS, 461, 3516

Norris, R. P., Hopkins, A. M., Afonso, J., et al. 2011, PASA, 28, 215

O'Dea, C. P., & Owen, F. N. 1986, ApJ, 301, 841

Ogrean G. A., Brüggen M., Röttgering H., et al. 2013, MNRAS, 429, 2617

Ogrean G. A., Brüggen M., van Weeren R., et al. 2014, MNRAS, 440, 3416

Okabe N., Akamatsu H., Kakuwa J., et al. 2015, PASJ, 67, 114

Oppermann N., Junklewitz H., Greiner M., et al. 2015, A&A, 575, A118

Pacholczyk A. G. 1970, Series of Books in Astronomy and Astrophysics, (San Francisco: Freeman)

Pandey-Pommier, M., van Weeren, R. J., Ogrean, G. A., et al. 2015, SF2A-2015: Proceedings of the Annual meeting of the French Society of Astronomy and Astrophysics, 247

Parekh V., Dwarakanath K. S., Kale R., & Intema H. 2017, MNRAS,464, 2752

Perley, R. A., Willis, A. G., & Scott, J. S. 1979, Nature, 281, 437

Perley, R. A., & Taylor, G. B. 1991, AJ, 101, 1623

Perley R. A., & Butler B. J. 2013, ApJS, 204, 19

Planck Collaboration, Ade P. A. R., Aghanim N., et al. 2013, A&A, 550, A130

Planck Collaboration, Ade P. A. R., Aghanim N., et al. 2016, A&A, 594, A19

Prandoni, I., Gregorini, L., Parma, P., et al. 2001, A&A, 365, 392

Prandoni, I., Murgia, M., Tarchi, A., Burgay, M., Castangia, P., Egron, E., Govoni, F., Pellizzoni, A., Ricci, R., Righini, S., et al. (36 more) , 2017, A&A, 608, A40

Pratley, L., Johnston-Hollitt, M., Dehghan, S., & Sun, M. 2013, MNRAS, 432, 243

Reimer, O., Pohl, M., Sreekumar, P., Mattox, J.R., 2003, ApJ588, 155

Rengelink R. B., Tang Y., de Bruyn A. G., et al. 1997, A&AS, 124,

Roettiger, K., Burns, J. O., & Stone, J. M. 1999, ApJ, 518, 603

Röttgering, H., Afonso, J., Barthel, P., et al. 2011, Journal of Astrophysics and Astronomy, 32, 557

Roland, J. 1981, A&A, 93, 407

Rybicki, G. B., & Lightman, A. P., 1979, Radiative processes in astrophysics, Wiley-Interscience

Rudnick, L., & Lemmerman, J. A. 2009, ApJ, 697, 1341

Rudnick, L., & Owen, F. N. 2014, ApJ, 785, 45

Sarazin, C. L. 2002, Merging Processes in Galaxy Clusters, 272, 1

Sault, R. J., Teuben, P. J., & Wright, M. C. H. 1995, Astronomical Data Analysis Software and Systems IV, 77, 433

Schlafly, E. F., & Finkbeiner, D. P. 2011, ApJ, 737, 103

Scodeggio, M., Guzzo, L., Garilli, B., et al. 2016, arXiv:1611.07048

Shakouri, S., Johnston-Hollitt, M., & Pratt, G. W. 2016, MNRAS, 459, 2525

Sijbring, L. G. 1993, Groningen: Rijksuniversiteit, |c1993,

Stanimirovic, S., Staveley-Smith, L., Dickey, J. M., Sault, R. J., & Snowden, S. L. 1999, MNRAS, 302, 417

Stott, J. P., Edge, A. C., Smith, G. P., Swinbank, A. M., & Ebeling, H. 2008, MNRAS, 384, 1502

Stroe, A., van Weeren, R. J., Intema, H. T., et al. 2013, A&A, 555, A110

Stroe, A., Harwood, J. J., Hardcastle, M. J., & Röttgering, H. J. A. 2014, MNRAS, 445, 1213

Stroe, A., Shimwell, T., Rumsey, C., et al. 2016, MNRAS, 455, 2402

Taylor, G. B., & Perley, R. A. 1993, ApJ, 416, 554

Taylor, G. B., Govoni, F., Allen, S. W., & Fabian, A. C. 2001, MNRAS, 326, 2

Taylor, A. R., Stil, J. M., & Sunstrum, C., 2009, ApJ, 702, 1230

Trasatti, M., Akamatsu, H., Lovisari, L., et al. 2015, A&A, 575, A45

Truemper, J. 1993, Science, 260, 1769

Vacca, V., Murgia, M., Govoni, F., et al. 2012, A&A, 540, A38

Vacca, V., Oppermann, N., Enßlin, T., et al. 2016, A&A, 591, A13

van Weeren, R. J., Röttgering, H. J. A., Brüggen, M., & Hoeft, M. 2010, Science, 330, 347

van Weeren, R. J., Brüggen, M., Röttgering, H. J. A., & Hoeft, M. 2011, MNRAS, 418, 230

van Weeren, R. J., Bonafede, A., Ebeling, H., et al. 2012, MNRAS, 425, L36

van Weeren, R. J., Intema, H. T., Lal, D. V., et al. 2014, ApJ, 781, L32

van Weeren, R. J., Intema, H. T., Lal, D. V., et al. 2014, ApJ, 786, L17

van Weeren, R. J., Andrade-Santos, F., Dawson, W. A., et al. 2017, Nature Astronomy, 1, 0005

Vazza, F., Ferrari, C., Brüggen, M., et al. 2015, A&A, 580, A119

Vernstrom, T., Scott, D., Wall, J. V., et al. 2014, MNRAS, 440, 2791

Voges, W., Aschenbach, B., Boller, T., et al. 1999, A&A, 349, 389

Vogt, C., & Enßlin, T. A. 2003, A&A, 412, 373

Vogt, C., & Enßlin, T. A. 2005, A&A, 434, 67

von Hoerner, S. 1973, ApJ, 186, 741

Völk, H. J., & Atoyan, A. M. 2000, ApJ, 541, 88

White, R. L., Becker, R. H., Helfand, D. J., & Gregg, M. D. 1997, ApJ, 475, 479

Wilman, R. J., Miller, L., Jarvis, M. J., et al. 2008, MNRAS, 388, 1335

Xu, H., Li, H., Collins, D. C., Li, S., & Norman, M. L. 2009, ApJ, 698, L14

Xu, H., Li, H., Collins, D. C., Li, S., & Norman, M. L. 2010, ApJ, 725, 2152

Xu, H., Li, H., Collins, D. C., Li, S., & Norman, M. L. 2011, ApJ, 739, 77

Xu, H., Govoni, F., Murgia, M., et al. 2012, ApJ, 759, 40

Zwicky, F. 1937, ApJ, 86, 217

Acknowledgements

F. Loi gratefully acknowledges Sardinia Regional Government for the financial support of her PhD scholarship (P.O.R. Sardegna F.S.E. Operational Programme of the Autonomous Region of Sardinia, European Social Fund 2007-2013 - Axis IV Human Resources, Objective l.3, Line of Activity l.3.1.). This research was partially supported by PRIN-INAF 2014. This work is part of the "Cybersar" Project, which is managed by the COSMOLAB Regional Consortium with the financial support of the Italian Ministry of University and Research (MUR), in the context of the "Piano Operativo Nazionale Ricerca Scientifica, Sviluppo Tecnologico, Alta Formazione (PON 2000-2006)". The Sardinia Radio Telescope (Bolli et al. 2015; Prandoni et al. 2017) is funded by the Ministry of Education, University and Research (MIUR), Italian Space Agency (ASI), the Autonomous Region of Sardinia (RAS) and INAF itself and is operated as National Facility by the National Institute for Astrophysics (INAF). The development of the SARDARA back-end has been funded by the Autonomous Region of Sardinia (RAS) using resources from the Regional Law 7/2007 "Promotion of the scientific research and technological innovation in Sardinia" in the context of the research project CRP-49231 (year 2011, PI Possenti): "High resolution sampling of the Universe in the radio band: an unprecedented instrument to understand the fundamental laws of the nature". The National Radio Astronomy Observatory (NRAO) is a facility of the National Science Foundation, operated under cooperative agreement by Associated Universities, Inc. This research made use of the NASA/IPAC Extragalactic Database (NED) which is operated by the Jet Propulsion Laboratory, California Institute of Technology, under contract with the National Aeronautics and Space Administration. This publication makes use of data products from the Two Micron All Sky Survey, which is a joint project of the University of Massachusetts and the Infrared Processing and Analysis Center/California Institute of Technology, funded by the National Aeronautics and Space Administration and the National Science Foundation.